

*In vivo*  $^1\text{H}$  NMR spectroscopy of the rat brain  
at 16.4 T

Dissertation

zur Erlangung des Grades eines Doktors  
der Naturwissenschaften

der Mathematisch-Naturwissenschaftlichen Fakultät  
und  
der Medizinischen Fakultät  
der Eberhard-Karls-Universität Tübingen

vorgelegt

von

**Sung-Tak Hong**

aus Incheon, Südkorea

2011

Tag der mündlichen Prüfung:

24. 08. 2011

Dekan der Math.-Nat. Fakultät:

Prof. Dr. W. Rosenstiel

Dekan der Medizinischen Fakultät:

Prof. Dr. I. B. Autenrieth

1. Berichterstatter:

Prof. Dr. Klaus Scheffler

2. Berichterstatter:

Prof. Dr. Uwe Klose

Prüfungskommission:

Prof. Dr. Klaus Scheffler

Prof. Dr. Uwe Klose

Prof. Dr. Fritz Schick

Prof. Dr. Bernd Pichler

PD. Dr. Matthias Munk

*I hereby declare that I have produced the work entitled: "In vivo  $^1\text{H}$  NMR spectroscopy of the rat brain at 16.4 T" submitted for the award of a doctorate, on my own (without external help), have used only the sources and aids indicated and have marked passages included from other works, whether verbatim or in content, as such.*

Tübingen, 03.05.2011

(Sung-Tak Hong)

## Personal contributions to the publications

### **Chapter 2 (publication 1)**

*Enhanced neurochemical profile of the rat brain using in vivo  $^1\text{H}$  NMR spectroscopy at 16.4 T.* Sung-Tak Hong, David Balla, G. Shajan, Changho Choi, Kamil Ugurbil, Rolf Pohmann. *Magnetic Resonance in Medicine* 2011; 65: 28-34.

Contribution: Initial pulse sequence was written by Sung-Tak Hong and developed by Dr. Rolf Pohmann. The design of the study, sequence parameter optimization, *in vivo*  $^1\text{H}$  NMR spectroscopy measurements, data processing, analysis and writing the manuscript were done by Sung-Tak Hong. An acetate infusion experiment was performed together with Dr. David Balla.

### **Chapter 3 (publication 2)**

*Rat-strain dependent variations in brain metabolites detected by in vivo  $^1\text{H}$  NMR spectroscopy at 16.4 T.* Sung-Tak Hong, David Z. Balla, Changho Choi, Rolf Pohmann. *NMR in Biomedicine* (in press)

Contribution: Initial pulse sequence was written by Sung-Tak Hong and developed by Dr. Rolf Pohmann. The design of the study, *in vivo*  $^1\text{H}$  NMR spectroscopy measurements, development of reconstruction program, data processing, statistical analysis and writing the manuscript were done by Sung-Tak Hong.

### **Chapter 4 (publication 3)**

*Determination of regional variations and reproducibility in in vivo  $^1\text{H}$  NMR spectroscopy of the rat brain at 16.4 T.* Sung-Tak Hong, David Balla, Rolf Pohmann. *Magnetic Resonance in Medicine* 2011; 66: 11-17.

Contribution: The design of the study, *in vivo*  $^1\text{H}$  NMR spectroscopy measurements, data processing, statistical analysis and writing the manuscript were done by Sung-Tak Hong.

### **Chapter 5**

*Quantification issues of in vivo  $^1\text{H}$  NMR spectroscopy of the rat brain investigated at 16.4 T.* Sung-Tak Hong, Rolf Pohmann. (Submitted to *NMR in Biomedicine*)

Contribution: The design of the study, *in vivo*  $^1\text{H}$  NMR spectroscopy measurements, development of a program for Monte-Carlo simulation, data processing and analysis and writing the manuscript were done by Sung-Tak Hong.

## **DEDICATION**

For my parents, Myong-son Hong and Suk-cha Kim.

## **ACKNOWLEDGEMENTS**

First and foremost, I would like to express my deepest gratitude to my advisor, Dr. Rolf Pohmann, for his constant guidance and support throughout this dissertation work. My deepest appreciation goes to Dr. David Balla for his valuable discussion and instruction on MR instruments. In addition, my appreciation is expanded to G. Shajan for his excellent hardware, which has been used in all experiments. Thanks to my sister and her husband for being a source of support that I can always count on. Finally, I would love to express my special thanks to my father, Myong-son Hong, and my mother, Suk-cha Kim, for their unconditional and endless love, concern and support with their sacrifice. They have given me the confidence to dream big and the courage to pursue my interests.

## CONTENTS

ABSTRACT .....	1
1. Introduction to NMR spectroscopy .....	2
2. Enhanced Neurochemical Profile of the Rat Brain using <i>in vivo</i> $^1\text{H}$ NMR Spectroscopy at 16.4 T .....	19
3. Rat-strain dependent variations in brain metabolites detected by <i>in vivo</i> $^1\text{H}$ NMR spectroscopy at 16.4 T .....	32
4. Determination of regional variations and reproducibility in <i>in vivo</i> $^1\text{H}$ NMR spectroscopy of the rat brain at 16.4 T .....	43
5. Quantification issues of <i>in vivo</i> $^1\text{H}$ NMR spectroscopy of the rat brain investigated at 16.4 T .....	55
6. CONCLUSIONS and OUTLOOK .....	70
APPENDIX .....	72



## ABSTRACT

Since the discovery of nuclear magnetic resonance (NMR) in the middle of the 1940s, this phenomenon has become a crucial tool for investigating chemical compounds and protein structures. The introduction of imaging gradients for phase- and frequency-encoding made it possible to acquire spatial information giving rise to magnetic resonance imaging (MRI), which has been utilized widely in clinical and preclinical applications. Complementary to MRI, the development of sequences that use gradients to select a specific volume-of-interest (VOI) established magnetic resonance spectroscopy (MRS) for detecting the biochemical information in a specific location or a selected tissue type within a living subject. In contrast to MRI, which is based on the abundant signal from water,  $^1\text{H}$  MRS detects signals from protons attached to biologically more interesting molecules, suppressing the water signal, which leads to long measurement times due to the inherently low concentrations (millimolar) of the metabolites of interest. One of the fundamental approaches to solve this problem is to increase the static field strength.

The goal of this thesis was to develop and optimize a localization sequence for *in vivo*  $^1\text{H}$  NMR spectroscopy at 16.4 T, aiming for accurate quantification of metabolites. To increase the localization performance, outer volume suppression (OVS) modules preceded the localization part of the sequence. The use of short echo time (TE) enables to acquire the maximal neurochemical information, though with significant contributions from macromolecular components. A sophisticated algorithm, based on a linear combination of *in vivo* data with *in vitro* model spectra was used for precise quantification. A basis data set of metabolite spectra was generated by numerical simulation based on the density matrix formalism while macromolecular components were included by parameterization of measured signals.

The application of this methodology demonstrated the possibility to reliably acquire highly enhanced neurochemical profiles with the potential to quantify up to 20 metabolites in the rat brain. The sensitivity gain at ultra-high field strength was explored by analyzing the Cramér-Rao lower bounds (CRLB) as a function of the number of averages. Subsequently, interstrain differences in metabolite concentrations were examined in the thalamus and the hippocampus. The potential for extended applications of *in vivo*  $^1\text{H}$  NMR spectroscopy was demonstrated by acquiring the neurochemical profile in the posterior part of the rat brain, the cerebellum and the medulla oblongata, as well as in the hippocampus and the thalamus, demonstrating regional variations of metabolite concentrations. Intra- and inter-individual reproducibility was also investigated to ascertain the reliability and applicability of *in vivo*  $^1\text{H}$  NMR spectroscopy.

To assess the influence of the high field and the field homogeneity on the quantification, the dependence of the linewidth and signal-to-noise ratio (SNR) were examined with the use of Monte Carlo simulations. Finally, the effect of different ways to account for macromolecular signals on the results of metabolites quantification was investigated.

The experiments presented in the following chapters illustrate the high quality of spectral information that can be obtained *in vivo* at ultra-high field. Demonstrating reliable solutions to some of the main challenges of *in vivo*  $^1\text{H}$  NMR spectroscopy, like generation of basis spectra for quantification, implementing macromolecular signals into the quantification algorithm or optimization of the measurement protocol for ultra-short echo times, it is shown that highly accurate, quantitative values for the concentrations of up to 20 metabolites in the rat brain are possible, representing a detailed neurochemical profile.

The contents of chapters 2 to 5 are transcripts of papers that have been either published (chapters 2 to 4) or is in preparation to be submitted (chapter 5) to peer-reviewed journals specialized on MR imaging and spectroscopy.

## Chapter 1

### Introduction

*In vivo*  $^1\text{H}$  NMR spectroscopy of the brain is a non-invasive technique to detect some of the most abundant biochemical compounds simultaneously by suppressing the substantial water signal (1). It has been widely established as an indispensable tool providing information about diverse neurochemical processes related to energy metabolism, membrane metabolism, neurotransmission and the antioxidant system, and can give valuable insight into normal and pathological processes at the molecular and cellular level *in vivo*. Substantial methodological developments over the past decades have extended *in vivo*  $^1\text{H}$  NMR spectroscopy to acquire two- or more-dimensional data with techniques such as chemical shift imaging (CSI) (2) or localized correlated spectroscopy (L-COSY) (3). However, all experiments in this thesis were confined to one-dimensional single voxel spectroscopy (SVS) with an ultra-short echo time (TE) to maximize the neurochemical information acquired.

### 1.1 Principles of NMR Spectroscopy

#### 1.1.1 Chemical Shift

Consider the molecular structure of lactate and its corresponding  $^1\text{H}$  NMR spectrum (Fig. 1a). Two groups, methine (CH) and methyl ( $\text{CH}_3$ ), in lactate give rise to two distinct peaks, where the magnetic field experienced by a nucleus, is reduced due to the shielding of the surrounding electrons, giving rise to slightly diminished resonance frequencies. The large electronegativity of oxygen causes a reduction in the electron density of the protons of the methine group (deshielding), resulting in a slight increase of the resonance frequency visualized by a shift of the spectral line to the left in the spectrum. The protons in the methyl group, on the other hand, have a relatively high electron density, leading to a shift of their resonance peak to the right. This small variation of resonance frequencies is called chemical shift and makes it possible to differentiate individual protons based on their different chemical environment.

The chemical shielding causes a shift in the local magnetic field at the site of the nucleus that can be expressed as

$$B = B_0(1 - \sigma)$$

where  $\sigma$  is a shielding constant and  $B_0$  is the external magnetic field.

Although chemical shifts can be expressed in units of Hz, it is more convenient to use units of parts per million (ppm), which is independent of  $B_0$ . In principle, the choice of the zero-point of the chemical shift scale is arbitrary, though in  $^1\text{H}$  NMR spectroscopy it is customary to use the resonance frequency of tetramethylsilane (TMS) as reference. The chemical shift ( $\delta_{\text{ppm}}$ ) is then defined as

$$\delta_{\text{ppm}} = 10^6 \times \frac{\nu - \nu_{\text{TMS}}}{\nu_{\text{TMS}}}$$

where  $\nu_{\text{TMS}}$  and  $\nu$  are the resonance frequencies of TMS ( $\delta_{\text{ppm}} = 0$ ) and that of the compound under investigation, respectively.

While the chemical shift can cause artifacts, known as chemical shift artifacts, in MRI, it forms the basis of MRS due to its ability to identify different functional groups within molecules and providing evidence for determining the molecular structure. The increased spectral dispersion at higher field strengths as shown in Fig. 1b demonstrates the improved separation of the Glu methylene signals at 2.04 ppm and 2.11 ppm at 16.4 T compared to lower field strengths.

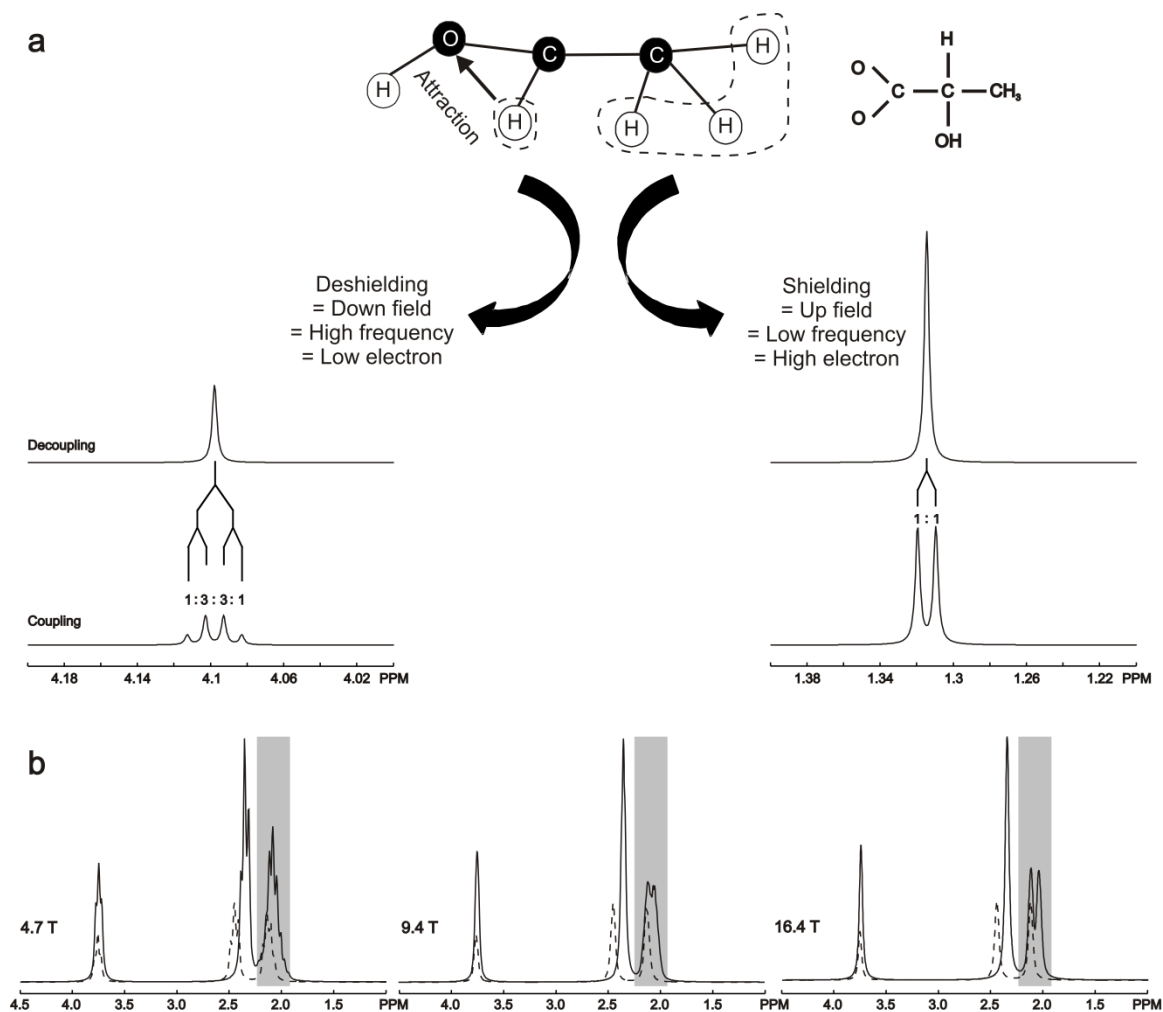


Figure 1. Principles of chemical shift and scalar coupling. (a) Molecular structure and simulated spectra of lactate without and with J-coupling. (b) Numerically calculated spectra of glutamate and glutamine (dotted line) assuming concentrations of  $8.3 \mu\text{mol/g}$  and  $2.7 \mu\text{mol/g}$ , respectively. Different linebroadening values of 5 Hz at 4.7 T, 10 Hz at 9.4 T and 20 Hz at 16.4 T were applied. The chemical shift dispersion of the Glu methylene signals at 2.04 ppm and 2.11 ppm (gray) increases with static field strength, making it possible to clearly separate the two peaks. In contrast, the split of the resonance lines due to J-coupling that is clearly visible at the lower field disappears at high field strength due to the higher absolute linewidth.

### 1.1.2 J-coupling

Nuclear spins within a molecule interact with each other indirectly through the propagation by the surrounding electrons. This effect, known as *J*-coupling, results in a split of the resonance lines into two or more components, depending on the number of non-equivalent, interacting nuclei. In contrast to the chemical shift, the modification of the resonance frequency caused by J-coupling does not scale with the magnetic field strength.

Depending on the size of the splitting compared to the chemical shift, J-coupling can be classified as weak or strong coupling. As convention, spin systems that are weakly coupled are labeled as AX systems, where the large differences in alphabetical order represent the distance in resonance frequencies compared to J-coupling. The individual nuclei in such a system are often labeled I and S, where I is the nucleus under observation and S is the interacting nucleus. Correspondingly, an AB spin system indicates strongly-coupled spins based on the small difference in alphabetical order.

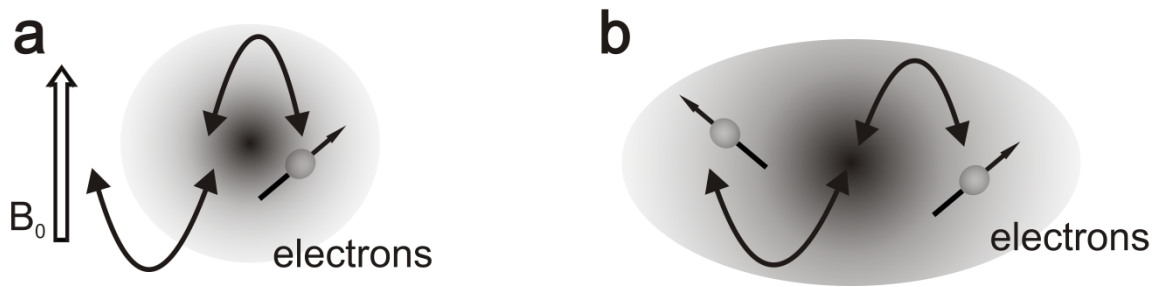


Figure 2. Schematic comparison of chemical shift and J-coupling. (a) Chemical shift as indirect interaction of the magnetic field with the nuclear spin via conduction electrons. (b) J-coupling is an indirect interaction between nuclear spins, propagated by the electrons.

### 1.1.2.1 Weak coupling

A spin system of two spin types with different chemical shift is said to be *weakly coupled* when the separation of their Larmor frequencies is much larger than their J-coupling. For a coupled two-spin system, four energy levels are observed, their individual energy given by:

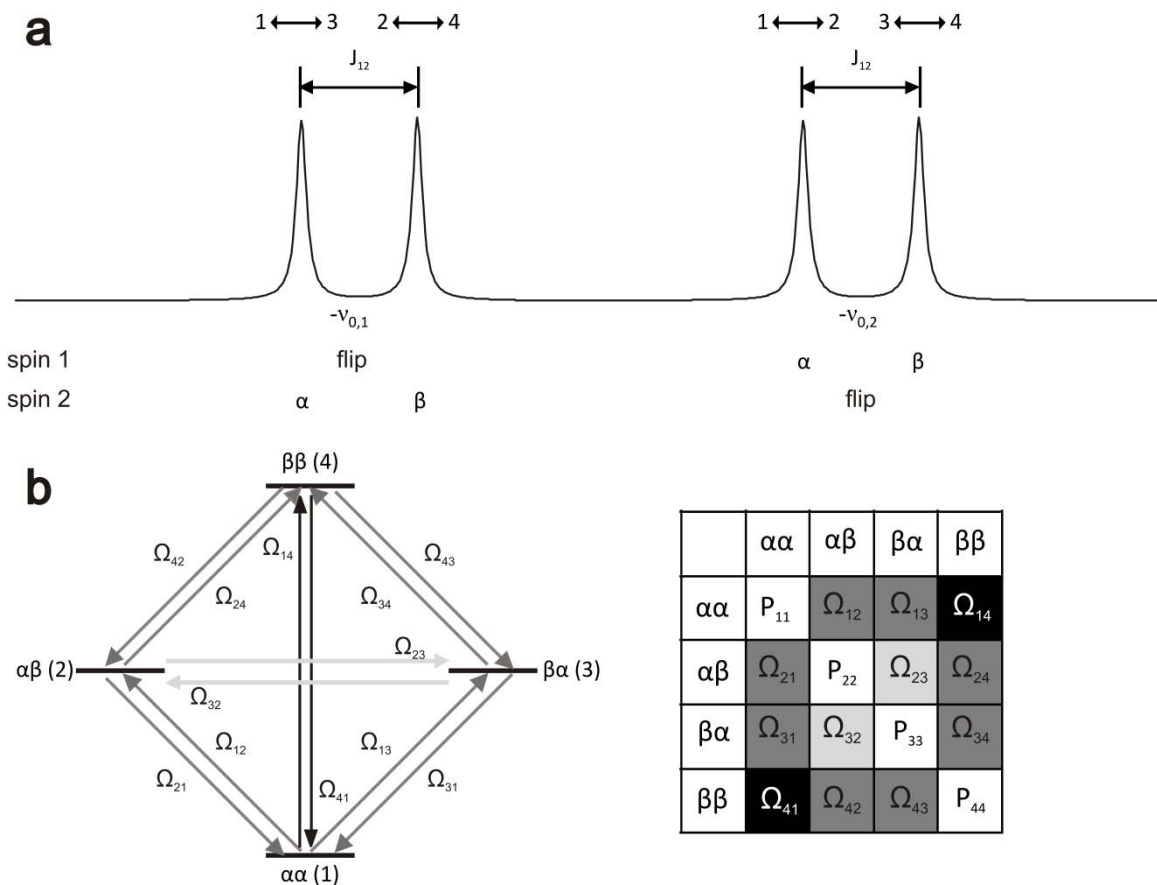


Figure 3. (a) Simulated spectrum of an AX spin system displaying four peaks with resonance frequencies of  $-v_{0,1} \pm \frac{1}{2}J_{12}$  and  $-v_{0,2} \pm \frac{1}{2}J_{12}$ . (b) Energy level diagram of a coupled two-spin system. Each transition is represented by an uni-directional arrow with different colors, black, dark gray and light gray indicating double quantum coherences, single quantum coherences and zero quantum coherences, respectively. The corresponding representation in the density matrix formalism is illustrated on the right side. The four diagonal elements indicate the populations of the states since they do not evolve with time.

$$E_{m_1 m_2} = m_1 \nu_{0,1} + m_2 \nu_{0,2} + m_1 m_2 J_{12},$$

where  $m$  is the quantum number, which for the case of a spin one-half nucleus can assume two values of  $-\frac{1}{2}$  and  $+\frac{1}{2}$ . The Larmor frequencies of spin 1 and spin 2, respectively, are given by  $\nu_{0,1} = -\frac{1}{2\pi}\gamma(1 + \delta_1)B_0$  and  $\nu_{0,2} = -\frac{1}{2\pi}\gamma(1 + \delta_2)B_0$  and  $J_{12}$  is the coupling constant expressed in Hz. Conventionally,  $m = +\frac{1}{2}$  is indicated by  $\alpha$  and referred to as “spin up”, while the “spin down” state is labeled  $\beta$ .

number	spin states	energy
1	$\alpha\alpha$	$+\frac{1}{2}\nu_{0,1} + \frac{1}{2}\nu_{0,2} + \frac{1}{4}J_{12}$
2	$\alpha\beta$	$+\frac{1}{2}\nu_{0,1} - \frac{1}{2}\nu_{0,2} - \frac{1}{4}J_{12}$
3	$\beta\alpha$	$-\frac{1}{2}\nu_{0,1} + \frac{1}{2}\nu_{0,2} - \frac{1}{4}J_{12}$
4	$\beta\beta$	$-\frac{1}{2}\nu_{0,1} - \frac{1}{2}\nu_{0,2} + \frac{1}{4}J_{12}$

The resulting frequencies are calculated as (for the example of a transition from state 1 to 2):

$$\nu_{12} = E_2 - E_1 = +\frac{1}{2}\nu_{0,1} - \frac{1}{2}\nu_{0,2} - \frac{1}{4}J_{12} - \left(\frac{1}{2}\nu_{0,1} + \frac{1}{2}\nu_{0,2} + \frac{1}{4}J_{12}\right) = -\nu_{0,2} - \frac{1}{2}J_{12}$$

For all transitions, the observed frequencies are:

transition	spin states	frequency
1 $\rightarrow$ 2	$\alpha\alpha \rightarrow \alpha\beta$	$-\nu_{0,2} - \frac{1}{2}J_{12}$
3 $\rightarrow$ 4	$\beta\alpha \rightarrow \beta\beta$	$-\nu_{0,2} + \frac{1}{2}J_{12}$
1 $\rightarrow$ 3	$\alpha\alpha \rightarrow \beta\alpha$	$-\nu_{0,1} - \frac{1}{2}J_{12}$
2 $\rightarrow$ 4	$\alpha\beta \rightarrow \beta\beta$	$-\nu_{0,1} + \frac{1}{2}J_{12}$

An exemplary spectrum is presented in Fig. 3a, showing two doublets with a total of four resonance frequencies. Below (Fig. 3b) is a representation of the density matrix, the elements of which represent the average probability of all possible states and transitions of the ensemble. The diagonal elements in the density matrix (Fig. 3b) represent the probability to find the spin system in the given eigenstates while the off-diagonal elements indicate coherent superpositions of eigenstates, which are grouped in three types of transitions:

1. Zero quantum coherences (transitions) connect the  $\alpha\beta$  and  $\beta\alpha$  states without changing the overall quantum number.
2. Single quantum coherences (transitions) correspond to the signals commonly to be observed.
3. Double quantum coherences (transitions) connect the  $\beta\beta$  to  $\alpha\alpha$  states.

### 1.1.2.2 Strong coupling

If the weak-coupling approximation is not valid, the spin system is said to be *strongly coupled*. The frequencies and intensities of a strongly coupled two-spin system are given by

transition	frequency	Intensity
1 – 2	$\frac{1}{2}D - \frac{1}{2}\Sigma - \frac{1}{2}J_{12}$	$(1 + \sin 2\theta)$
3 – 4	$\frac{1}{2}D - \frac{1}{2}\Sigma + \frac{1}{2}J_{12}$	$(1 - \sin 2\theta)$
1 – 3	$-\frac{1}{2}D - \frac{1}{2}\Sigma - \frac{1}{2}J_{12}$	$(1 - \sin 2\theta)$
2 – 4	$-\frac{1}{2}D - \frac{1}{2}\Sigma + \frac{1}{2}J_{12}$	$(1 + \sin 2\theta)$

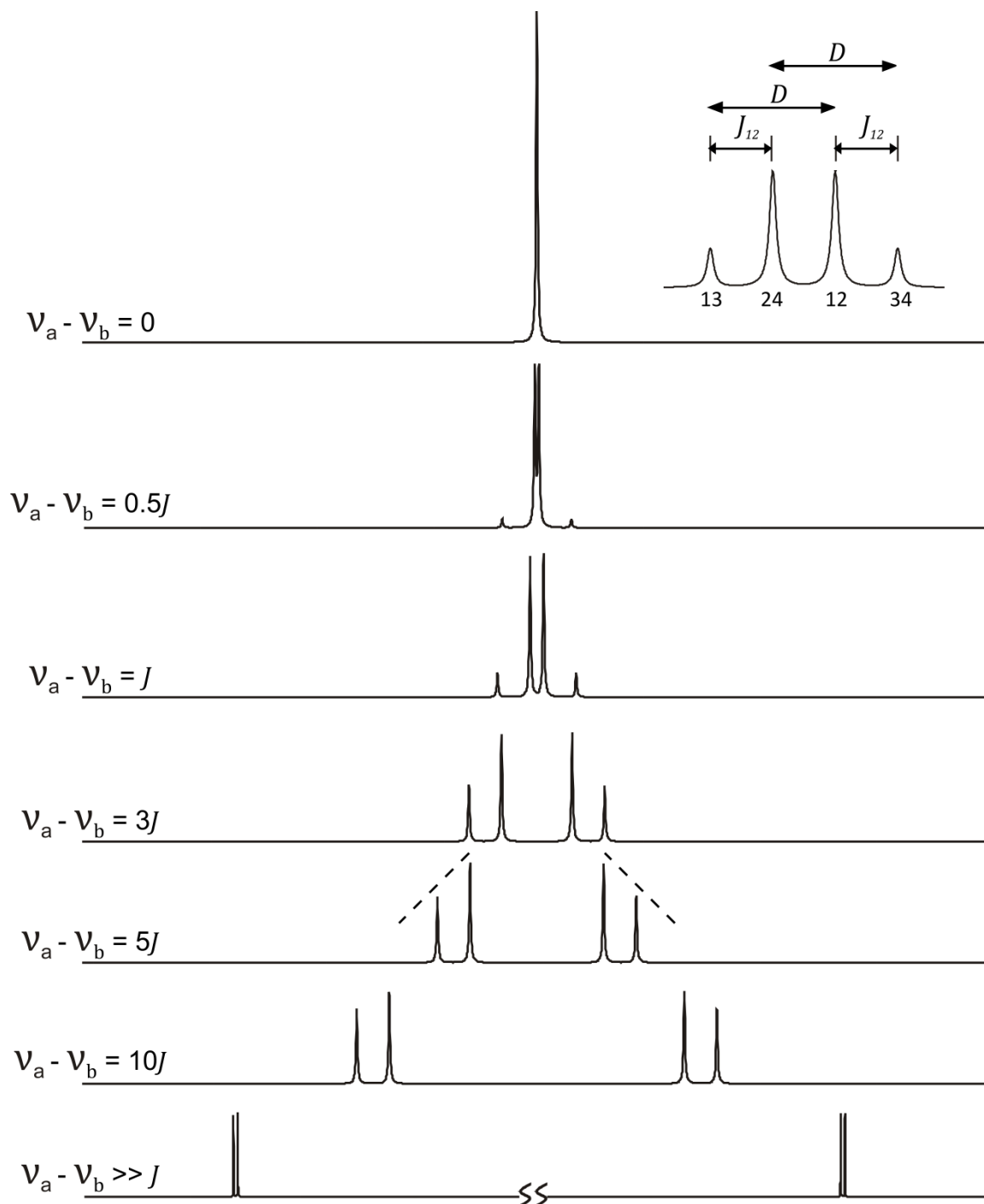


Figure 4. A series of spectra for a hypothetical spin system demonstrating the strong coupling effect with decreasing differences between resonance frequencies ( $\nu_a$  and  $\nu_b$ ). The coupling constant was fixed to 20 Hz. The dotted lines illustrate the so-called *roof effect*. The intensities of the outer lines become weaker and those of the inner lines become stronger. This effect disappears in the limit of a weakly coupled spectrum (lowest trace).

where  $\Sigma$  is the sum of the Larmor frequencies,  $\Sigma = \nu_{0,1} + \nu_{0,2}$ .  $D$  and  $\theta$  (strong coupling parameters) are defined by  $D^2 = (\nu_{0,1} - \nu_{0,2})^2 + J_{12}^2$  and  $\sin 2\theta = \frac{J_{12}}{D}$ , respectively. While in the weakly coupled spectrum the two lines of a doublet are just symmetrically distributed around the Larmor frequency, the spectrum of strongly coupled spin systems becomes more complicated: The frequency separations between  $\nu_{34}$  and  $\nu_{24}$  and between  $\nu_{12}$  and  $\nu_{13}$  are equal to  $D$  and the sum of the frequencies  $\nu_{12}$  and  $\nu_{24}$  as well as that of  $\nu_{34}$  and  $\nu_{13}$  is equal to  $-\Sigma$ :

$$\begin{aligned} \nu_{34} - \nu_{24} &= \left(\frac{1}{2}D - \frac{1}{2}\Sigma + \frac{1}{2}J_{12}\right) - \left(-\frac{1}{2}D - \frac{1}{2}\Sigma + \frac{1}{2}J_{12}\right) = D \\ \nu_{12} + \nu_{24} &= \left(\frac{1}{2}D - \frac{1}{2}\Sigma - \frac{1}{2}J_{12}\right) + \left(-\frac{1}{2}D - \frac{1}{2}\Sigma + \frac{1}{2}J_{12}\right) = -\Sigma \end{aligned}$$

Since the coupling constant can be measured directly in the spectrum (Fig. 4, inset), the value of  $(\nu_{0,1} - \nu_{0,2})$  can be calculated as

$$(\nu_{0,1} - \nu_{0,2}) = \sqrt{D^2 - J_{12}^2}$$

since,  $D^2 = (\nu_{0,1} - \nu_{0,2})^2 + J_{12}^2 \approx (\nu_{0,1} - \nu_{0,2})^2$ .

Using the knowledge of  $(\nu_{0,1} - \nu_{0,2})$  and  $\Sigma = \nu_{0,1} + \nu_{0,2}$ , the frequencies  $\nu_{0,1}$  and  $\nu_{0,2}$  can easily be calculated:

$$\nu_{0,1} = \frac{1}{2}(\Sigma + (\nu_{0,1} - \nu_{0,2})), \quad \nu_{0,2} = \frac{1}{2}(\Sigma - (\nu_{0,1} - \nu_{0,2}))$$

### 1.1.3 Localization

Localization is one of the most critical properties of *in vivo*  $^1\text{H}$  NMR spectroscopy making it possible to acquire metabolic information from a specific region inside a living sample. Among the available localization techniques, the point-resolved spectroscopy (PRESS) (4) sequence is used mostly due to its high SNR efficiency. This approach, however, has inevitable drawbacks such as increased TE and chemical shift displacement artifacts due to the two  $180^\circ$  pulses compared to a stimulated echo acquisition mode (STEAM) (5) sequence. Since both problems become more detrimental with increasing static magnetic field strength, the STEAM sequence has been used throughout this thesis. The inherent SNR loss in the STEAM sequence, which is caused by the acquisition of a stimulated echo having only half the amplitude of a corresponding spin echo, is tolerable at 16.4 T due to the high SNR.

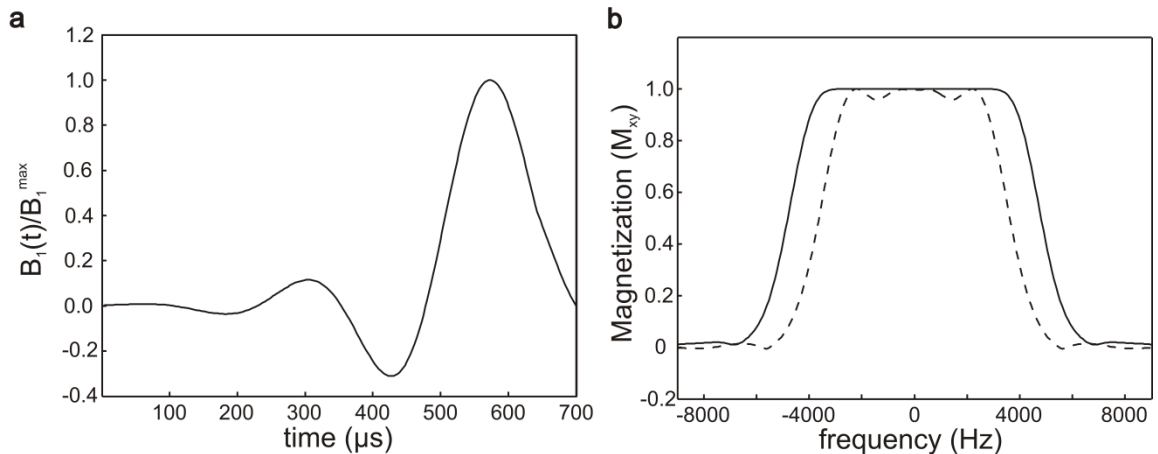


Figure 5. (a) Asymmetric  $90^\circ$  RF pulse waveform used in the STEAM sequence. (b) Transverse magnetization  $M_{xy}$  following a  $700 \mu\text{s}$  asymmetric pulse compared to that of a  $700 \mu\text{s}$  hermite pulse (dotted line). Note the wider bandwidth and flat plateau of the asymmetric pulse compared to the hermite pulse.

For reaching ultra-short echo times in STEAM, the duration of the slice-selective RF pulses and spoiler gradients has to be minimized. To this purpose, asymmetric pulses (6) were used for excitation and refocusing, providing shorter duration and improved slice profile compared to conventional pulses (Fig. 5). In addition, very short and strong spoiler gradients with a duration of 431  $\mu\text{s}$  and a strength of 820 mT/m were applied after the first and the third pulse of the STEAM sequence. An additional Gaussian pulse was inserted during the mixing time (TM) to improve the suppression of the water signal. Applying three  $90^\circ$  slice-selective pulses for localization generates three FIDs, four spin echoes and a stimulated echo (STE) at given time points, depending on TE and TM (Fig. 6). To observe the STE without contamination from other unwanted signals, phase cycling and spoiler gradients are combined in *in vivo*  $^1\text{H}$  NMR spectroscopy. Representative *in vivo*  $^1\text{H}$  NMR spectra with increasing TE are shown in Fig. 7.

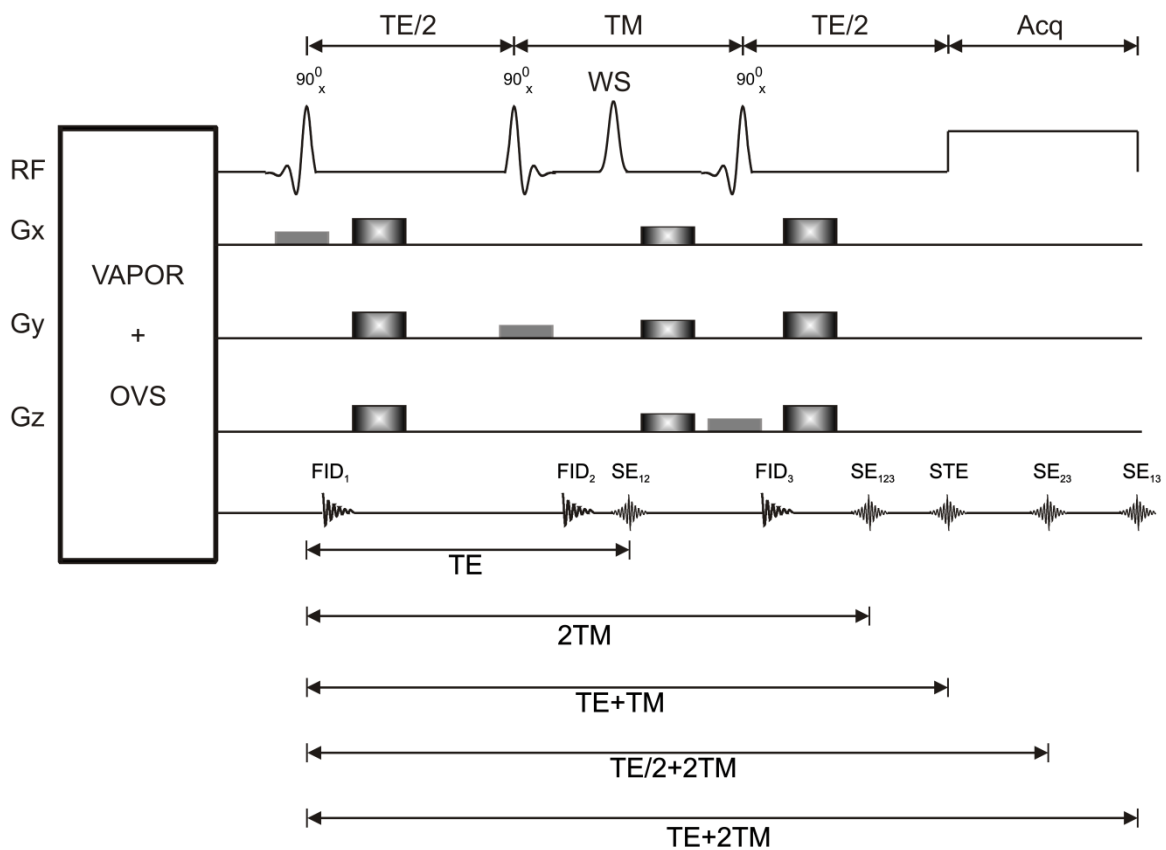


Figure 6. Diagram of the STEAM pulse sequence incorporating a preparation part consisting of water suppression (WS) and outer volume suppression (OVS) modules. The main localization is achieved by three slice-selective  $90^\circ$  pulses, yielding a total of eight signals: Three FIDs (FID<sub>1</sub>, FID<sub>2</sub> and FID<sub>3</sub>), four spin echos (SE<sub>12</sub>, SE<sub>13</sub>, SE<sub>23</sub> and SE<sub>123</sub>) and one stimulated echo (STE). Only the latter one is acquired. Since it is generated by all three slice-selective pulses jointly, it only represents signal from the selected voxel.

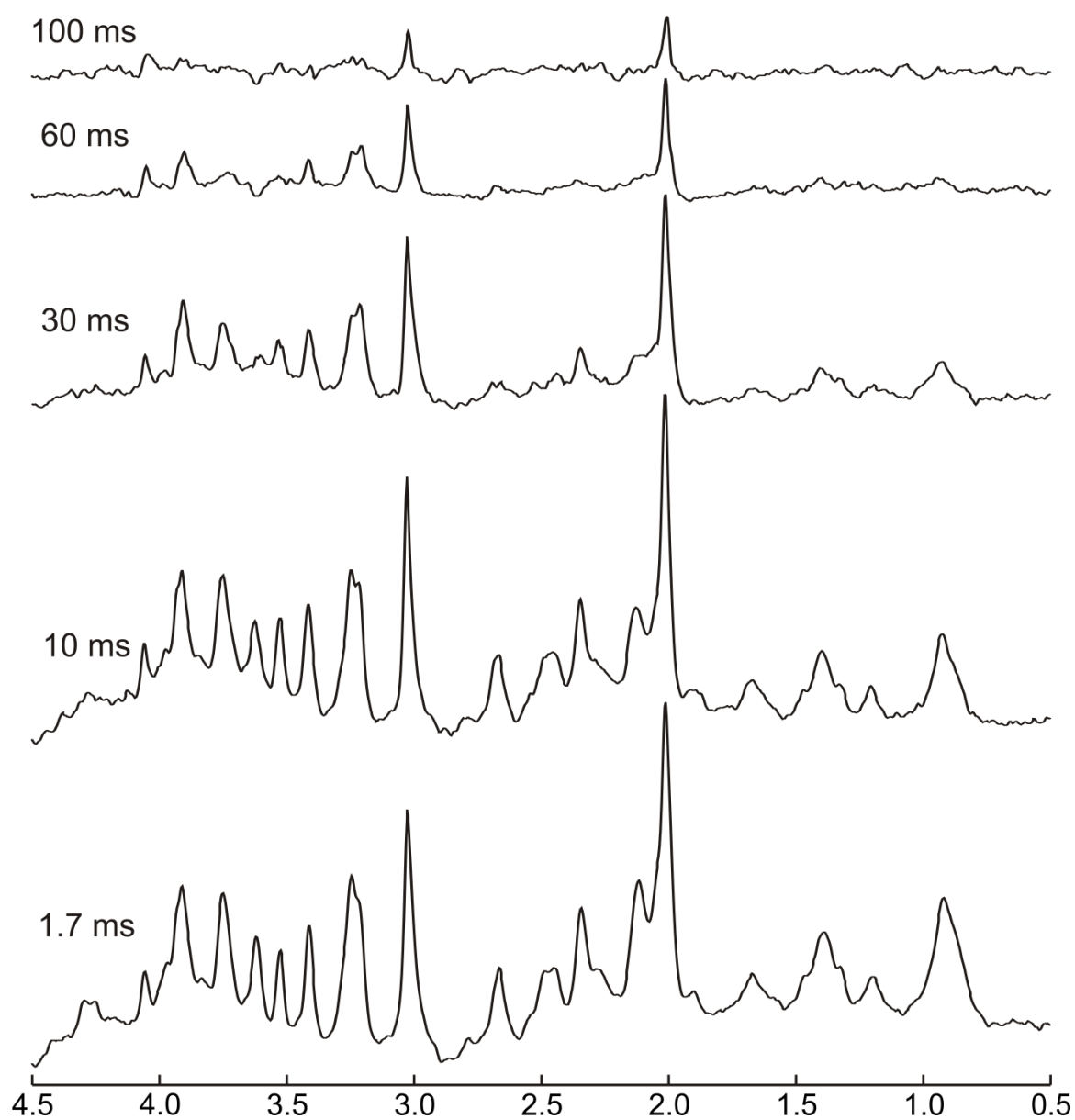


Figure 7. A series of *in vivo*  $^1\text{H}$  NMR spectra with a TE of 1.7 ms, 10 ms, 30 ms, 60 ms and 100 ms measured in a 68  $\mu\text{l}$  volume in the brain of a single rat (TR 5000 ms, TM 20 ms, 160 averages). All spectra were subjected to exponential filtering with a linebroadening of 10 Hz. All signals were scaled equally.

## 1.2 Quantification

*In vivo*  $^1\text{H}$  NMR spectroscopy makes it possible to obtain absolute metabolite concentrations (in  $\mu\text{mol/g}$  tissue mass) since the thermal equilibrium magnetization is directly proportional to the number of spins contributing to the signal. Assuming knowledge of the concentration of one (external or internal) reference signal, molar concentrations can be calculated. This requires precise determination of the amplitude and width of the overlapping and noisy resonance lines by fitting the measured spectra to model functions using appropriate and optimized techniques. Based on the fact that the Fourier transformation is a linear operation, the quantification process can be performed in principle as well in the time domain as in the frequency domain. An appropriate model function for representing NMR signals can be described as a sum of exponentially damped sinusoids in the time domain or as a sum of individual spectra in the frequency domain (Fig. 8).

In the time domain, the mathematical expression describing the exponentially damped signals depends on the lineshape assumed (7):

for Lorentzian lineshapes

$$y(t) = \hat{y}(t) + \varepsilon_t = \sum_{k=1}^K a_k e^{j\Phi_k} e^{(-d_k + j2\pi f_k)t} + b(t) + \varepsilon_t,$$

for Gaussian lineshapes

$$y(t) = \hat{y}(t) + \varepsilon_t = \sum_{k=1}^K a_k e^{j\Phi_k} e^{(-g_k t + j2\pi f_k)t} + b(t) + \varepsilon_t,$$

for Voigt lineshapes

$$y(t) = \hat{y}(t) + \varepsilon_t = \sum_{k=1}^K a_k e^{j\Phi_k} e^{(-d_k - g_k t + j2\pi f_k)t} + b(t) + \varepsilon_t,$$

$$t = t_0, \dots, t_{m-1}$$

where  $j = \sqrt{-1}$ ,  $m$  is the number of data points,  $K$  is the number of metabolites,  $a_k$  is the amplitude,  $\Phi_k$  is the phase,  $d_k$  is the damping factor,  $g_k$  is the Gaussian damping factor and  $f_k$  is the frequency shift. The background signal  $b(t)$  contains all contributions that are not modeled, since they are not included in the prior knowledge.  $\varepsilon_t$  is circular complex white Gaussian noise, where the term circular specifies that real and imaginary parts of the noise are not correlated and have equal variance. The  $\hat{y}$  describes a set of complex model signals generated by either *in vitro* measurements or numerical simulations, constituting the prior knowledge. The objective parameters such as  $a_k$ ,  $\Phi_k$ ,  $d_k$ ,  $g_k$ ,  $f_k$  and  $e_k$  can be estimated by minimizing a least squares criterion, the squared difference between the *in vivo* data  $y(t)$  and the model function

$$\sum_{t=t_0, \dots, t_{m-1}} [y(t) - \hat{y}]^2 \longrightarrow \min$$

resulting in a nonlinear least-squares (NLLS) problem, a solution to which can be found using the Levenberg-Marquardt algorithm (8, 9). Thus, NMR spectroscopy can be used as a completely quantitative method by measuring the amplitudes of the individual components in the time domain or by quantifying their areas in the frequency domain. This makes it possible to detect variations in metabolite concentrations, e.g. in different rat strains and brain regions, as demonstrated in the chapters 3 and 4, but also differences caused by pathological processes.

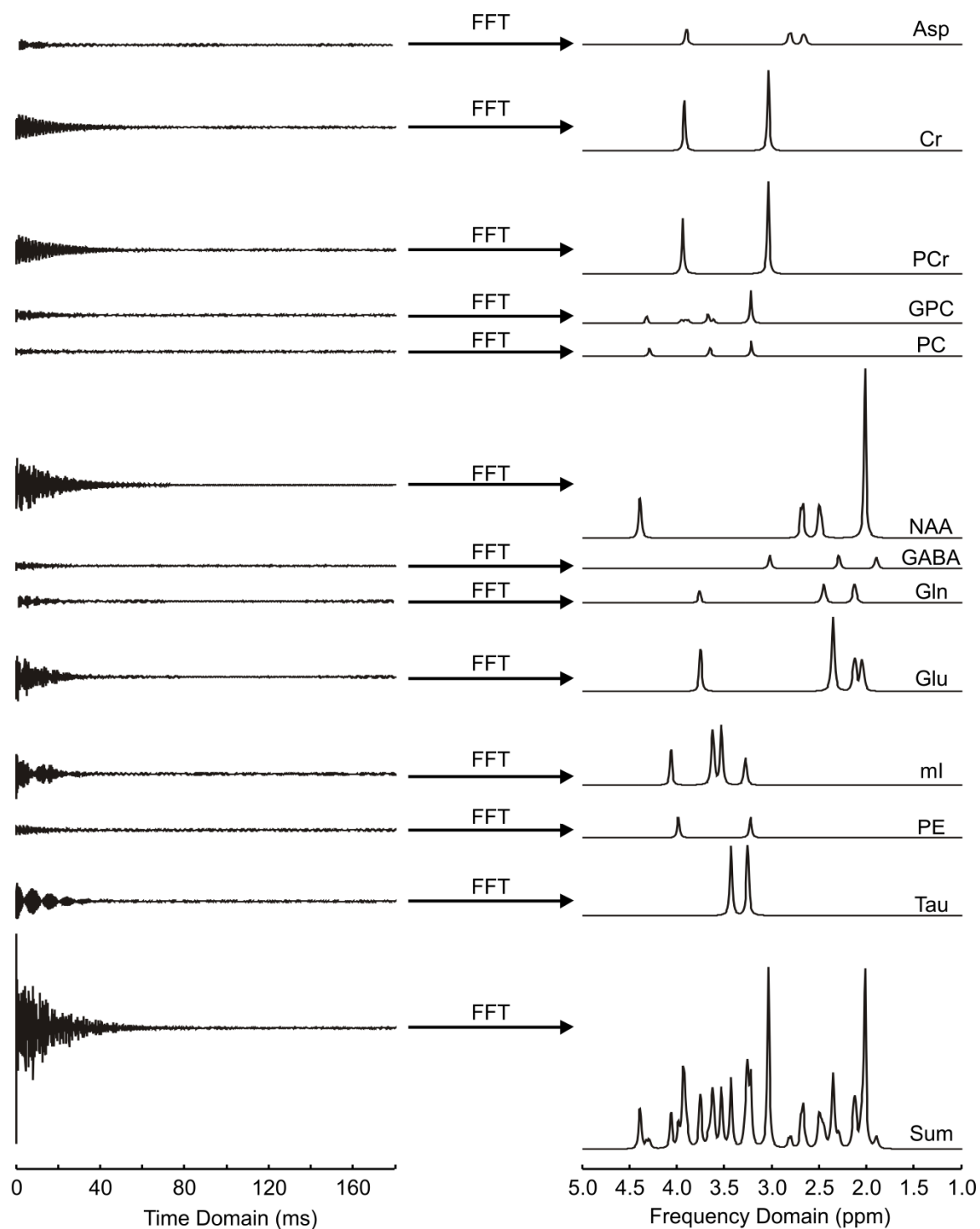


Figure 8. Signal formation in MRS. Each metabolite signal was generated by simulation and the FIDs were treated with an exponential filter (15 Hz) to imitate *in vivo* conditions. The metabolite concentrations were assumed as [Asp] : [Cr] : [PCr] : [GPC] : [PC] : [NAA] : [GABA] : [Gln] : [Glu] : [ml] : [PE] : [Tau] = 4.4 : 5.59 : 6.41 : 0.86 : 1.09 : 12.2 : 1.91 : 3.29 : 11.73 : 8.44 : 2.79 : 9.33.

The most commonly used programs for quantification of spectroscopic data are either the java-based MR user interface (jMRUI) (10), operating in the time domain, or the linear combination model (LCModel) (11), working in the frequency domain. In the experiments presented here, LCModel was used to quantify the signals due to its advantage of operating fully automatically, thus eliminating user-dependent influences.

### 1.2.1 Generation of basis spectra

Regardless of whether the signal is processed in the time domain or in the frequency domain, the accuracy of the fit can be optimized by taking advantage of prior knowledge, which is based on the fact that the metabolites existing in the brain as well as the resonance frequencies and the relative amplitudes of their spectral lines are known. To use this in the fitting procedure, a basis data set is required that contains the single spectra of all metabolites with high quality. Although this can be generated by *in vitro* measurements, using numerical simulations it is possible to obtain more reproducible basis data. Within this thesis, a routine to accurately calculate simulated spectroscopic data was used and improved to obtain a basis data set for LCModel quantification. This software is based on the density matrix formalism (12), the theoretical background of which is shortly described in the next sections, where two different ways for calculating the evolution of the spin magnetization during the sequence are presented, based on either analytical or numerical approaches.

#### 1.2.1.1 Analytical approach

To describe the behavior of large ensembles of interacting spins, the concept of the density operator is useful. It can be used to accurately find mean values for spin populations and their interactions without the need to follow the changes in the state of each individual spin. Based on the product operator formalism applying raising and lowering operators (APPENDIX), the density operators  $\sigma_I$  and  $\sigma_S$  of the spins I and S, respectively, immediately after an initial  $90^\circ_x$  slice-selective pulse in a weakly-coupled spin system (IS), can be expressed as

$$\sigma_I(0+) = \frac{i}{2}(I^+ - I^-), \quad \sigma_S(0+) = \frac{i}{2}(S^+ - S^-)$$

Following the spin behavior during the course of a STEAM sequence, the observable magnetizations of the spins I and S become

$$\begin{aligned} \sigma_I(TE + TM) &= -\frac{i}{8}(I^+ + I^-) \left[ 2 \cos^2\left(\frac{\pi JTE}{2}\right) - \sin^2\left(\frac{\pi JTE}{2}\right) \cos(\Delta\omega TM) \right] \\ \sigma_S(TE + TM) &= -\frac{i}{8}(I^+ e^{-i(\Delta\omega TM/2)} - I^- e^{+i(\Delta\omega TM/2)}) \sin^2\left(\frac{\pi JTE}{2}\right) \cos(\Delta\omega TM) \end{aligned}$$

Adding the two terms yields

$$\begin{aligned} &\sigma_I(TE + TM) + \sigma_S(TE + TM) \\ &= -\frac{i}{4}(I^+ - I^-) \cos^2\left(\frac{\pi JTE}{2}\right) + \frac{i}{8}(I^+ - I^-) \sin^2\left(\frac{\pi JTE}{2}\right) \cos(\Delta\omega TM) \\ &\quad - \frac{i}{8}I^+ \cos\left(\frac{\Delta\omega TE}{2}\right) \sin^2\left(\frac{\pi JTE}{2}\right) \cos(\Delta\omega TM) \\ &\quad + \frac{1}{8}I^+ \sin\left(\frac{\Delta\omega TE}{2}\right) \sin^2\left(\frac{\pi JTE}{2}\right) \cos(\Delta\omega TM) \\ &\quad + \frac{i}{8}I^- \cos\left(\frac{\Delta\omega TE}{2}\right) \sin^2\left(\frac{\pi JTE}{2}\right) \cos(\Delta\omega TM) \\ &\quad - \frac{1}{8}I^- \sin\left(\frac{\Delta\omega TE}{2}\right) \sin^2\left(\frac{\pi JTE}{2}\right) \cos(\Delta\omega TM) \end{aligned}$$

For quadrature detection aligned along the y axis of the rotating frame during the acquisition period, the net doublet signal  $S(TM + TE)$  is given by

$$S(TE + TM) = \frac{1}{2i}(I^+ - I^-) \times \frac{1}{2} \cos^2\left(\frac{\pi JTE}{2}\right) - \frac{1}{2i}(I^+ - I^-) \times \frac{1}{4} \cos(\Delta\omega TM) \sin^2\left(\frac{\pi JTE}{2}\right) \\ + \frac{1}{2i}(I^+ - I^-) \times \frac{1}{4} \cos\left(\frac{\Delta\omega TE}{2}\right) \sin^2\left(\frac{\pi JTE}{2}\right) \cos(\Delta\omega TM)$$

By omitting the term of a detection operator,  $I_y \left(= \frac{1}{2i}(I^+ - I^-)\right)$ , this becomes

$$S(TE + TM) = \frac{1}{2} \cos^2\left(\frac{\pi JTE}{2}\right) - \frac{1}{4} \cos(\Delta\omega TM) \sin^2\left(\frac{\pi JTE}{2}\right) + \frac{1}{4} \cos(\Delta\omega TE/2) \cos(\Delta\omega TM) \sin^2\left(\frac{\pi JTE}{2}\right) \\ = \frac{1}{2} \left\{ \cos^2\left(\frac{\pi JTE}{2}\right) - \frac{1}{2} \sin^2\left(\frac{\pi JTE}{2}\right) [1 - \cos(\Delta\omega TE/2)] \cos(\Delta\omega TM) \right\}$$

A general expression for  $I_nS$  spin systems ( $n = 1, 2$  or  $3$ ) is expressed by

$$S(TE + TM) = \frac{1}{2} \left\{ \cos^2\left(\frac{\pi JTE}{2}\right) - \frac{1}{2} \sin^2\left(\frac{\pi JTE}{2}\right) [1 - \cos^{n-1}(\pi JTM/2) \cos(\Delta\omega TE/2)] \times \cos^{n-1}(\pi JTM) \cos(\Delta\omega TM) \right\}$$

The disadvantage of this approach is on one hand the complicated calculation and on the other hand the constrictions to weakly-coupled (13) and strongly-coupled (AB and ABX) spin systems (14).

### 1.2.1.2 Numerical approach

To overcome the limitations of the analytical approach, the spin behavior in all spin systems can be simulated by density matrix calculations. The wavefunction is a linear combination of basis vectors, which is expressed as

$$|\Psi(t)\rangle = \sum_{i=1}^n c_i(t) |i\rangle$$

where the  $c_i$  are the time-dependent coefficients and  $|i\rangle$  represents the spin state (basis vectors). For two coupled  $1/2$ -spins, the above expression can be rewritten as

$$|\Psi(t)\rangle = c_1 |\alpha\alpha\rangle + c_2 |\alpha\beta\rangle + c_3 |\beta\alpha\rangle + c_4 |\beta\beta\rangle$$

The matrix representation of the density operator, i.e. the density matrix, defined by the product of the ket  $|\Psi(t)\rangle$  and the bra  $\langle\Psi(t)|$ , is given by

$$\rho(t) = |\Psi(t)\rangle\langle\Psi(t)| = \begin{bmatrix} c_1 \\ c_2 \\ c_3 \\ c_4 \end{bmatrix} [c_1^* \ c_2^* \ c_3^* \ c_4^*] = \begin{bmatrix} c_1 c_1^* & c_1 c_2^* & c_1 c_3^* & c_1 c_4^* \\ c_2 c_1^* & c_2 c_2^* & c_2 c_3^* & c_2 c_4^* \\ c_3 c_1^* & c_3 c_2^* & c_3 c_3^* & c_3 c_4^* \\ c_4 c_1^* & c_4 c_2^* & c_4 c_3^* & c_4 c_4^* \end{bmatrix}$$

The response of spins to the particular sequence can be predicted by solving the Liouville-von Neumann equation

$$\frac{d}{dt} \rho(t) = i[\rho(t), H(t)]$$

where the Hamiltonian  $\mathcal{H}(t)$  of the system including the main interactions for time-dependent spin evolution consists of several terms, each describing one type of interaction:

$$\mathcal{H} = \mathcal{H}_{zeeman} + \mathcal{H}_{J-coupling} + \mathcal{H}_{RF} + \mathcal{H}_{gradient}$$

$$\mathcal{H}_{zeeman} = \sum_{n=1}^M \omega_{In} I_{zn}$$

$$\mathcal{H}_{J-coupling} = 2\pi \sum_{\substack{i < j \\ 1 \leq i < M}} J_{ij} (I_i \cdot I_j)$$

$$\mathcal{H}_{RF} = \gamma B_1(t) [\cos \varphi \sum_{n=1}^M I_{xn} + \sin \varphi \sum_{n=1}^M I_{yn}]$$

$$\mathcal{H}_{gradient} = -\gamma \vec{G} \cdot \vec{r} \sum_{n=1}^M I_{zn}$$

where  $M$  represents the number of spins,  $B_1$  is the amplitude of the RF pulse,  $\varphi$  is the RF phase,  $\omega_{In}$  is the Larmor frequency of the spin  $i$ ,  $G$  is the strength of the gradient field,  $r$  is the distance from the center of the gradient field and  $J_{ij}$  is the scalar coupling constant between spin  $i$  and spin  $j$ . The Hamiltonian can become time-independent within a finite time segment by selecting a suitable rotating frame. In this way, the solution to the Liouville-von Neumann equation can be expressed by unitary transformations

$$\rho(t) = \exp(-i\mathcal{H}t)\rho(0)\exp(i\mathcal{H}t)$$

### 1.2.2 The density matrix simulation software

To calculate the basis spectra of all metabolites detected in the brain, which are used as prior knowledge for the quantification, a software package was used (15) that applies the numerical approach presented in the previous section to obtain simulated metabolite signals with high accuracy. The program is able to determine the temporal evolution of weakly or strongly coupled spin systems, including the effect of RF pulses and gradient fields. The chemical shift and coupling constants of 20 metabolites were taken from the literature (most values from Ref. (16), except for Asc (17), GABA (18) and NAAG (19)). All RF pulses were assumed to be ideal, nonselective  $90^\circ$  pulses, since it was shown that this does not yield significantly different behavior than with realistic slice-selective  $90^\circ$  RF pulses (20). Both weak and strong coupling were implemented and selected for each individual metabolite. All sequence parameters, such as duration and strength of spoiler gradients, TE and TM, assumed in the simulations were equal to those of the actual measurements, except for the number of data points, which was increased to 8192 for higher spectral resolution. To better resemble the *in vivo* data, an exponential filtering with a linebroadening of 2 Hz was applied. Finally, the FIDs corresponding to the simulated spectra were saved for use in LCModel (file extension of .RAW). All scripts for both simulating a spectrum and for generating the .RAW files were written with Matlab (MathWorks, Natick, MA, USA). Computation time was about 30 sec for a six spin system.

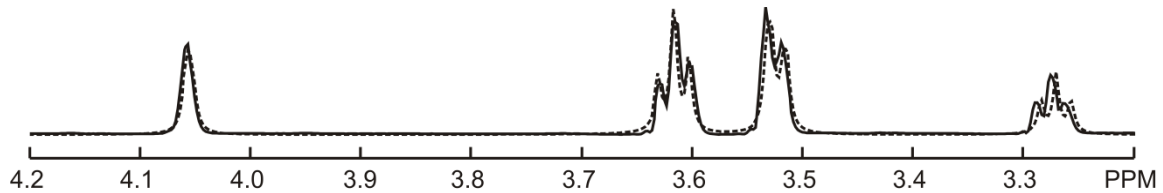


Figure 9. Comparison of a myo-Inositol spectrum acquired using the density matrix simulation (dashed line) with that acquired in a phantom measurement.

Fig. 9 shows the close agreement of an *in vitro* spectrum (ml) with a numerically calculated spectrum based on density matrix simulation.

### 1.2.3 Assessment of macromolecular signals

For spectroscopic measurements with short TE, the metabolite spectra are superimposed by broad lines from macromolecules. Due to the large size of these compounds, these signals have short  $T_2$ , which makes them disappear in experiments with larger TE, and short  $T_1$  which is used to separate their signals from those of the small metabolites. Macromolecules are mainly composed of proteins in the normal brain while contributions from lipids are observed in the diseased brain in cases of infarction (21) and tumor (22).

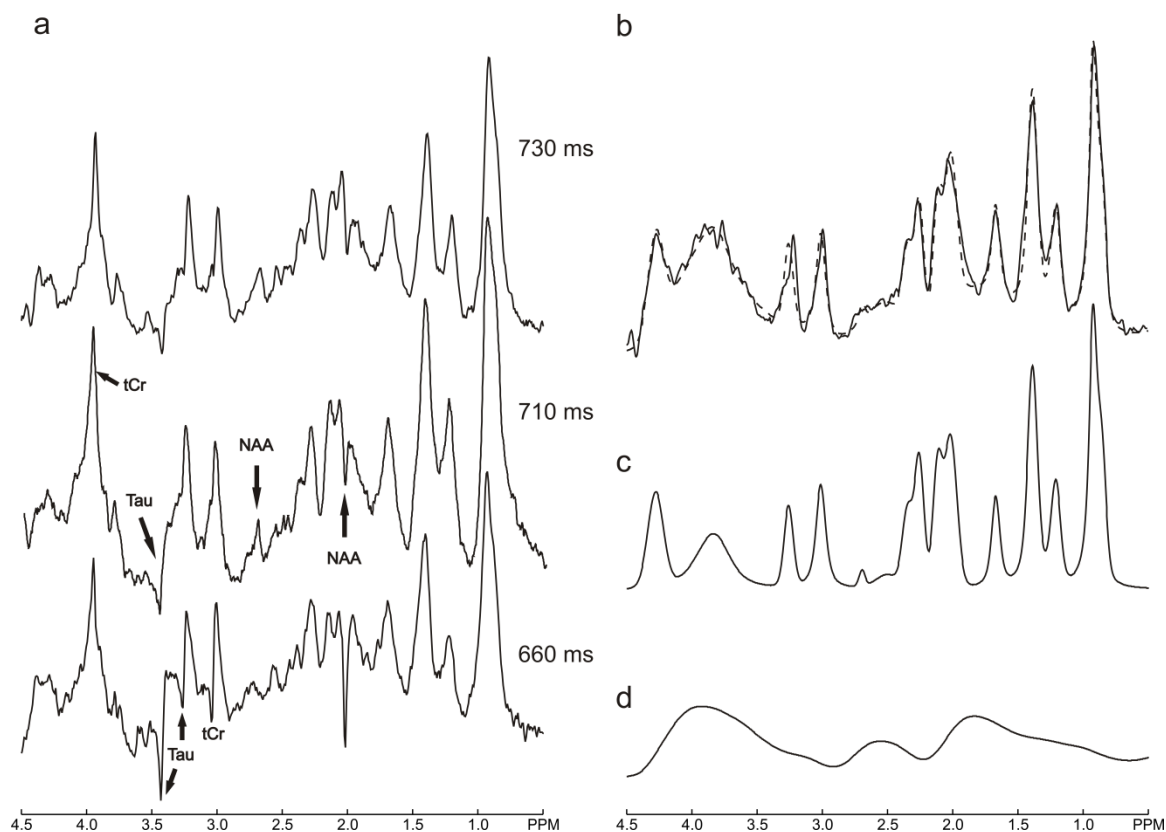


Figure 10. a: Series of MM spectra with increasing TI. The tCr signal at 3.94 ppm is positive in all spectra due to its shorter  $T_1$ . The MM spectrum with a TI of 710 ms showing residual metabolite contributions, negative peaks of NAA at 2.02 ppm and Tau at 3.422 ppm, and positive peaks of NAA at 2.68 ppm and tCr at 3.94 ppm, marked with arrows. All spectra were treated with an exponential filter with a linebroadening of 20 Hz. (b) MM components found by parameterization of the measured metabolite-nulled spectrum: the whole fitted MM components (c) and the spline baseline (d) determined in LCModel. Comparison of the fitted MM components in LCModel obtained with the measured MM spectrum and with the simulated MM spectrum (dashed line). The dashed curve is the summation of the fitted MM components (c) and the spline baseline (d). All signals (b, c, d) are scaled equally.

Several different approaches can be used to take these signals into account during the quantification. The easiest way is to include them into the regularized spline baseline, which is calculated by LCModel to contain all residual contributions. This way, the valuable information contained in those signals is wasted. In addition, an imperfect calculation of the baseline may cause errors in the quantification of the metabolites (see chapter 5). A common approach to access macromolecular signals is to obtain a pure macromolecular spectrum by an inversion-

recovery measurement and eliminating residual metabolite contributions. In this thesis, an alternative approach was used by parameterization of the single peaks found in the macromolecular spectrum (Fig. 10). After measuring amplitude, frequency and linewidth for each component, these values were implemented in LCMoDel to additionally determine the concentrations of the macromolecules within the quantification process. The advantages of this approach are the possibility to obtain quantitative values for each macromolecular component independently and to improve the metabolite quantification by releasing the constraint in the spine baseline determined by LCMoDel.

### 1.3 Conclusion

Typical problems of *in vivo*  $^1\text{H}$  NMR spectroscopy such as low SNR and narrow spectral dispersion have limited the application of this technique in the clinical and preclinical practice. The increasing static field strengths that are becoming available now can help to increase the amount of information that can be gathered from the spectra. Further improvements are possible by decreasing the echo time with the aid of high performance hardware, which makes it possible to reduce the durations of spoiler gradients and slice-selective RF pulses, resulting in increased SNR due to minimal J-modulation and reduced signal decay caused by  $T_2$  relaxation. The purpose of this thesis was to investigate the gain possible at ultra-high static field strength. For this aim, the potentials of acquiring an enhanced neurochemical profile were examined, where the accurate quantification of up to 20 metabolites was found possible (chapter 2). In addition, the precision (chapter 3) and reproducibility (chapter 4) of estimating metabolite concentrations was studied. This technique was furthermore applied to detect differences in metabolite concentrations between different rat strains and brain regions, where it is shown that the quantification is sufficiently precise to detect all variations exceeding the inter- and intra-individual differences.

## REFERENCES

1. de Graaf RA. *In vivo* NMR spectroscopy: principles and techniques. Second edition. Wiley: Chichester, 2007.
2. Brown TR, Kincaid BM, Ugurbil K. NMR chemical shift imaging in three dimensions. *Proc Natl Acad Sci U S A* 1982;79:3523-3526.
3. Thomas MA, Yue K, Binesh N, Davanzo P, Kumar A, Siegel B, Frye M, Curran J, Lufkin R, Martin P, Guze B. Localized two-dimensional shift correlated MR spectroscopy of human brain. *Magn Reson Med* 2001;46:58-67.
4. Bottomley PA. Spatial localization in NMR spectroscopy *in vivo*. *Ann N Y Acad Sci* 1987;508:333-348.
5. Frahm J, Merboldt KD, Hanicke W. Localized Proton Spectroscopy Using Stimulated Echoes. *J Magn Reson* 1987;72:502-508.
6. Starčuk Z Jr, Starčuk Z. Optimized asymmetric slice selective 90° and 180° RF pulses for localized MR spectroscopy. In: Proceedings of the SMR 2nd Annual Meeting, San Francisco, 1994. p 1137.
7. Sima DM, Van Huffel S. Separable nonlinear least squares fitting with linear bound constraints and its application in magnetic resonance spectroscopy data quantification. *J Comput Appl Math* 2007;203:264-278.
8. Levenberg K. A Method for the Solution of Certain Non-Linear Problems in Least Squares. *Q Appl Math* 1944;2:164-168.
9. Marquardt DW. An Algorithm for Least-Squares Estimation of Nonlinear Parameters. *J Soc Ind Appl Math* 1963;11:431-441.
10. Naressi A, Couturier C, Devos JM, Janssen M, Mangeat C, de Beer R, Graveron-Demilly D. Java-Based graphical user interface for the MRUI quantitation package. *Magn Reson Mater Phy* 2001;12:141–152.
11. Provencher SW. Estimation of metabolite concentrations from localized *in vivo* proton NMR spectra. *Magn Reson Med* 1993;30:672-679.
12. Ernst RR, Bodenhausen G, Wokaun A. Principles of nuclear magnetic resonance in one and two dimensions. Oxford: Oxford University Press; 1987. p 9–17.

13. Sorensen OW, Eich GW, Levitt MH, Bodenhausen G, Ernst RR. Product Operator-Formalism for the Description of NMR Pulse Experiments. *Prog Nucl Mag Res Sp* 1983;16:163-192.
14. Kay LE, McClung RED. A Product Operator Description of AB and ABX Spin Systems. *J Magn Reson* 1988;77:258-273.
15. Kaiser LG, Young K, Matson GB. Numerical simulations of localized high field  $^1\text{H}$  MR spectroscopy. *J Magn Reson* 2008;195:67-75.
16. Govindaraju V, Young K, Maudsley AA. Proton NMR chemical shifts and coupling constants for brain metabolites. *NMR Biomed* 2000;13:129-153.
17. Terpstra M, Marjanska M, Henry PG, Tkac I, Gruetter R. Detection of an antioxidant Profile in the Human Brain *In Vivo* Via Double Editing With MEGA-PRESS. *Magn Reson Med* 2006;56:1192–1199.
18. Kaiser LG, Young K, Meyerhoff DJ, Mueller SG, Matson GB. A detailed analysis of localized J-difference GABA editing: theoretical and experimental study at 4 T. *NMR Biomed* 2008;21:22–32.
19. Krawczyk H, Gradowska W. Characterisation of the  $^1\text{H}$  and  $^{13}\text{C}$  NMR spectra of N-acetylaspartylglutamate and its detection in urine from patients with canavan disease. *J Pharm Biomed Anal* 2003;31:455–463.
20. Thompson RB, Allen PS. Response of metabolites with coupled spins to the STEAM sequence. *Magn Reson Med* 2001;45:955-965.
21. Saunders DE, Howe FA, van den Boogaart A, Griffiths JR, Brown MM. Discrimination of metabolite from lipid and macromolecule resonances in cerebral infarction in humans using short echo proton spectroscopy. *J Magn Reson Imaging* 1997;7:1116-1121.
22. Kaminogo M, Ishimaru H, Morikawa M, Ochi M, Ushijima R, Tani M, Matsuo Y, Kawakubo J, Shibata S. Diagnostic potential of short echo time MR spectroscopy of gliomas with single-voxel and point-resolved spatially localised proton spectroscopy of brain. *Neuroradiology* 2001;43:353-363.

## Chapter 2

### Enhanced Neurochemical Profile of the Rat Brain using *in vivo* $^1\text{H}$ NMR Spectroscopy at 16.4 T

Sung-Tak Hong, David Zsolt Balla, G. Shajan, Changho Choi, Kamil Ugurbil, Rolf Pohmann

Published in Magnetic Resonance in Medicine 2011; 65: 28-34.

#### ABSTRACT

Single voxel magnetic resonance spectroscopy with ultra-short echo time was implemented at 16.4 T to enhance the neurochemical profile of the rat brain *in vivo*. A TE of 1.7 ms was achieved by sequence optimization and by using short-duration asymmetric pulses. Macromolecular signal components were parameterized individually and included in the quantitative analysis, replacing the use of a metabolite-nulled spectrum. Due to the high spectral dispersion, several signals close to the water line could be detected and adjacent peaks could be resolved. All 20 metabolites detected in this study were quantified with Cramér-Rao lower bounds (CRLB) below 20%, implying reliable quantification accuracy. The signal of acetate was detected for the first time in rat brain *in vivo* with CRLB of 16% and a concentration of 0.52  $\mu\text{mol/g}$ . The absolute concentrations of most metabolites showed close agreement with values previously measured using *in vivo*  $^1\text{H}$  NMR spectroscopy and *in vitro* biochemical assay.

Key words:  $^1\text{H}$  magnetic resonance spectroscopy (MRS); STEAM; Ultra-short TE; LCModel; Parameterization; Macromolecular; Ultrahigh-field

## 2.1 INTRODUCTION

Localized *in vivo*  $^1\text{H}$  NMR spectroscopy provides a unique opportunity for measuring brain metabolite concentrations noninvasively, thus providing neurochemical information of *in vivo* processes (1). This capability has been shown to benefit from increasing magnetic field strength because of gains in signal-to-noise ratio (SNR) and chemical shift resolution. These advantages were demonstrated by detecting and quantifying 18 metabolites in the rat brain *in vivo* with an ultra-short echo time stimulated echo acquisition mode (STEAM) sequence at 9.4 T (2). Subsequently the detection of ascorbate (Asc) was reported with both ultra-short TE STEAM and a J-difference editing technique (3), also at 9.4 T. Recently, several signals adjacent to the water peak, including N-acetylaspartate (NAA) at 4.38 ppm, glycerophosphorylcholine (GPC) at 4.31 ppm and phosphorylcholine (PCho) at 4.27 ppm, were resolved with narrow RF bandwidths for water suppression, taking advantage of the increased spectral dispersion at 14.1 T (4).

The availability of 16.4 T provides the potential of quantifying additional metabolites not detectable at lower field strength. Acetate (Ace), composed of a short-chain organic acid, is widely recognized to be a substrate for glial cells (5). With *in vivo*  $^1\text{H}$  NMR spectroscopy, the detection of the Ace methyl resonance at 1.9 ppm has not yet been possible due to its low concentration and virtually complete overlap with the methylene resonances of both  $\gamma$ -aminobutyric acid (GABA) at 1.889 ppm and N-acetylaspartylglutamate (NAAG) at 1.9 ppm. Detection of Ace has therefore been limited to  $^1\text{H}$ - $^{13}\text{C}$ -NMR spectroscopy (6) and high resolution  $^1\text{H}$ -NMR on perchloric acid (PCA) extracts of the rat brain (7).

Although ultra-short TE makes it possible to obtain valuable metabolite information, it also leads to larger contributions from signals of macromolecules (MM); assessing this component is a critical factor in accurate metabolite quantification. Three different methods have been used to take account of the MM components in short TE *in vivo*  $^1\text{H}$  NMR spectra. The first approach is to acquire an MM spectrum with an inversion-recovery metabolite-nulled measurement and then use this as a basis set in the quantification procedure (2). The second is to obtain both a metabolite spectrum and an MM spectrum from each study and subtract the MM spectrum from the metabolite spectrum before quantification (8). The third approach is to simulate MM components based on prior knowledge parameterized using a measured MM spectrum (9). Although the first method is the most widely used, the third approach is employed in this study because of the advantage of allowing less constraints on the baseline by fitting each MM component or small groups of adjacent components separately (10), increasing the possibility to detect metabolites with very low concentrations, and to enable studies where MM concentrations vary due to pathologies.

In this work, the echo time of a STEAM sequence was minimized by reducing the duration of the slice-selective RF pulses and the spoiler gradients at a field strength of 16.4 T. This maximizes the SNR by minimizing signal decay due to  $T_2$  relaxation and reduces J-modulation effects, resulting in improved accuracy of metabolite quantification as well as providing the feasibility of detecting metabolites previously unresolved in *in vivo* spectra. Therefore, the purpose of the present study was 1) to provide an improved neurochemical profile of the rat brain *in vivo* with reasonable accuracy 2) to demonstrate the feasibility of simulated MM components to substitute the metabolite-nulled spectrum.

## 2.2 MATERIALS AND METHODS

### 2.2.1 Animal Handling

Twelve male Sprague-Dawley rats ( $204 \pm 12$  g) were used in the experiments. All rats experienced a 12-h alternating light-dark schedule in a temperature-controlled ( $23 \pm 2$  °C) room with free access to food and water. Experiments were performed in accordance with the European guidelines for care and use of laboratory animals and with permission of the local review board.

Anesthesia was initially induced by inhalation of a mixture of O<sub>2</sub> and isoflurane at a 4–5% concentration and then maintained using 1.5–2.5% isoflurane. Rectal temperature was monitored and maintained at  $37 \pm 0.5$  °C by an electric heating pad placed under the torso.

In a supplementary measurement performed in one single rat, Ace was infused to ascertain the assignment of its methyl signal at 1.9 ppm. A three molar solution of Ace (adjusted to a pH of 7.0 with NaOH) was administered through a tail vein at a variable rate over 2 h, using a protocol described previously (11).

### **2.2.2 Localized Proton Magnetic Resonance Spectroscopy (MRS)**

All measurements were performed on a 16.4 T/ 26 cm horizontal magnet (Magnex Scientific, Abingdon, UK) interfaced to a Bruker spectrometer (Bruker BioSpin GmbH, Ettlingen, Germany). The actively shielded gradient with 12 cm inner diameter has a maximum strength of 1000 mT/m and a rise time of 212  $\mu$ s. A home-built quadrature RF surface coil, composed of two geometrically decoupled single-turn coils (18 mm diameter), was employed for both transmitting and receiving. The position of the volume-of-interest (VOI) was carefully selected based on multi-slice axial  $T_1$ -weighted MR images obtained using a rapid acquisition with relaxation enhancement (RARE) sequence (repetition time TR = 1500 ms, TE = 7.5 ms, slice thickness = 1.0 mm, matrix size = 256 x 256). A rectangular VOI (6.5 x 3.5 x 2.5 mm<sup>3</sup>) was positioned in the thalamus of the rat brain. Localization was achieved with an ultra-short TE STEAM sequence (TR = 5000 ms, TM = 20 ms, TE = 1.7 ms, 256 averages, 2048 complex data points) consisting of three asymmetric 90° pulses (duration 700  $\mu$ s, bandwidth 7400 Hz) (12). The water signal was suppressed with the VAPOR (Variable Power RF Pulses with Optimized Relaxation Delays) technique, using seven chemical shift-selective gaussian RF pulses (9.1 ms, 300 Hz) interleaved with three outer volume saturation (OVS) modules (12). To increase water suppression efficiency, an additional gaussian RF pulse was employed in the TM period. Adjustment of all first- and second-order shim terms was accomplished with the fast automatic shimming technique by mapping along the projections (FASTMAP) (13), resulting in a total Creatine (tCr) linewidth of  $23 \pm 3$  Hz (0.033 ppm) *in vivo*. For the Ace infusion experiment, TR was increased to 6000 ms and a 5.2 x 2.5 x 2.5 mm<sup>3</sup> voxel, mainly encompassing the hippocampus, was used.

For modeling the MM components, an inversion-recovery module was applied prior to the STEAM sequence, employing an additional nonselective adiabatic full-passage pulse with a duration of 2 ms and a bandwidth of 11930 Hz. A sequence of metabolite-nulled spectra was measured with a TR of 2500 ms and inversion times (TI) of 660 ms, 710 ms, 730 ms, 770 ms and 840 ms. These experiments consisted of 640 averages, except for the 710 ms-measurement (1280 averages). The short TR in these experiments helped to further minimize contributions of residual metabolite signals by partially saturating them, while allowing the MM signals to recover completely because of their short  $T_1$  relaxation times (14).

The short TE for all experiments was achieved using spoiler gradients with a duration of 431  $\mu$ s and a strength of 820 mT/m and 852 mT/m in the first and second half of the TE, respectively. The calculated diffusion weighting factor (b-value) was 64.1 s/mm<sup>2</sup>, indicating negligible diffusion-induced signal loss for an apparent diffusion coefficient (ADC) on the order of 10<sup>-3</sup> mm<sup>2</sup>/s (15).

A reference spectrum composed of eight averages without water suppression was acquired prior to the actual measurement for eddy current correction (16).

### **2.2.3 Data Processing and Quantification**

No post-processing such as baseline correction, apodization or water subtraction was applied to keep the original metabolite information.

Metabolite concentrations were analyzed with LCMoDel (17), using numerically calculated basis spectra generated with an in-house Matlab program (MathWorks, Natick, MA, USA), which uses the Liouville-von Neumann equation to calculate the evolution of the spin density matrix under the Hamiltonian with the actual parameters used in the STEAM sequence. Product-operator based transformation matrices for slice-selective 90° pulses were generated and used to calculate the

density operator evolution over the sequence, including summation of density matrices over space (18, 19). The spatial resolution for the simulation of slice selection was 1% of the slice thickness. The following 20 metabolites were included in the LCModel basis data: Ace, alanine (Ala), aspartate (Asp), Asc, creatine (Cr), GABA, glucose (Glc), glutamate (Glu), glutamine (Gln), Glycine (Gly), glutathione (GSH), GPC, PCho, myo-inositol (ml), lactate (Lac), NAA, NAAG, phosphocreatine (PCr), phosphorylethanolamine (PE), and taurine (Tau). All chemical-shift values and coupling constants were taken from (7) except for Asc (20), NAAG (21) and GABA (22). For absolute quantification, tCr was used as an internal reference, assumed to be 8.5  $\mu\text{mol/g}$  (2).

MM signals were also included in the LCModel basis set. The necessary prior knowledge was obtained from the metabolite-nulled spectrum, by applying the Hankel Lanczos singular value decomposition (HLSVD) routine (23), built in jMRUI (24), to eliminate residual contributions from water and metabolite signals. LCModel parameters of MM signals were obtained from this spectrum and fine-adjusted based on the fitting result found with the metabolite-nulled spectrum to reach optimum agreement.

## 2.3 RESULTS

A representative *in vivo*  $^1\text{H}$  NMR spectrum from the thalamus with fitting results is shown in Fig. 1. Compared to the spectrum from 9.4 T (2), a clear separation was observable between two Glu methylene signals at 2.04 ppm and 2.11 ppm. All NAAG resonances including the glutamate moiety at 1.9 ppm and 4.14 ppm were clearly distinguishable. The separation of the GPC methylene signals at 3.603 ppm and 3.664 ppm was visible. Three metabolites, GPC at 4.314 ppm, PCho at 4.28 ppm and NAA at 4.38 ppm, co-resonating with MM, were clearly resolved.

The series of spectra acquired by inversion recovery measurements with different TI are shown in Figure 2. In addition to a negative NAA peak at 2.02 ppm, two distinctly inverted peaks, tCr at 3.03 ppm and Tau at 3.246 ppm are visible at a TI of 660 ms and, having already crossed the null point, at 730 ms (Fig. 2b). A TI of 710 ms was found as optimum, yielding minimal contributions of NAA at 2.02 ppm as well as of Tau at 3.246 ppm and 3.422 ppm. HLSVD was applied to further eliminate the residual metabolite signals, NAA at 2.02 ppm and 2.68 ppm, Tau at 3.422 ppm and tCr at 3.94 ppm from this spectrum. The results of the parameterization of all MM components are summarized in Table 1. To model the complex structures between 2.0 ppm and 2.7 ppm and at around 3.8 ppm, signals M20 and M38 were composed of six and three single resonances with fixed amplitude ratios, respectively. The M09 signal was modeled by two overlapping components M09a and M09b that were fitted independently, yielding a good replication of its lineshape with minimum residual.

Remaining discrepancies between simulated and measured peaks, especially in the region of the M38 component, which could not be modeled satisfactorily by the Gaussian-Lorentzian lineshape generated by LCModel (25), are compensated by the elaborately regularized spline baseline obtained with a knot spacing of 0.15 in LCModel. Adding this baseline to the fitted MM components shows close agreement between the fitted and the measured MM spectrum (Fig. 3c). Consistent and reliable determination of MM components is indicated by the low standard deviations and CRLBs (Table 1).

The fitting result of the LCModel analysis with the basis set including all 20 metabolites and MM components demonstrates the reliable determination of each individual metabolite and MM contributions reflected by the flat baseline (Fig. 1b). The high sensitivity and increased chemical dispersion make it possible to resolve metabolites with very low concentrations such as Ace resonating at 1.9 ppm and Gly at 3.55 ppm in all rats measured in this study.

Quantitative metabolite concentrations are summarized in Table 2, with and without including Ace and Gly in the basis set in the LCModel analysis. All analyzed metabolites demonstrate average CRLBs below 20%. The inclusion of Gly in the LCModel analysis had no influence on the quantification of the overlapping line of ml. NAAG, one of the overlapping metabolites with Ace, also shows a consistent concentration with and without including Ace in the basis data, while the

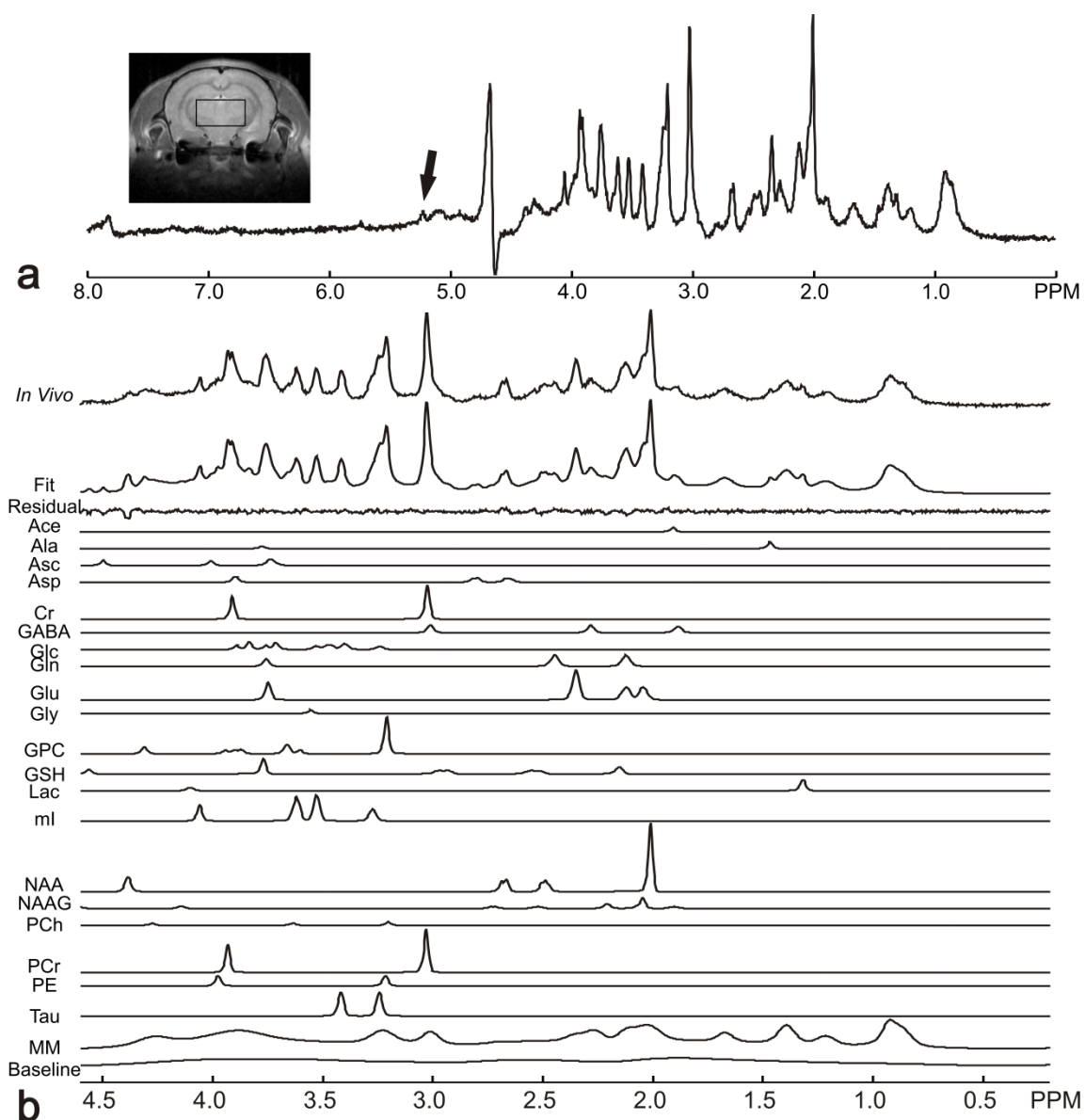


Figure 1. a: Representative *in vivo*  $^1\text{H}$  NMR spectrum from the thalamus of the rat brain acquired with ultra-short TE STEAM. The spectrum was processed only with eddy current correction, Fourier-transformation and phase correction; no apodization or baseline correction was applied. The Glc methine resonance at 5.22 ppm is marked by an arrow. b: Expanded region between 0.2 ppm and 4.6 ppm illustrating LCMoDel results with the basis set including both 20 metabolites and MM components. Shown are (from top to bottom) the *in vivo* spectrum, the fitted spectrum, the residual, fitting results of 20 individual metabolites, the MM components and the spline baseline. Note a partially saturated methine signal of NAA at 4.38 ppm owing to the water suppression pulses, resulting in a marked negative signal in the residual. All spectra in b are scaled identically.

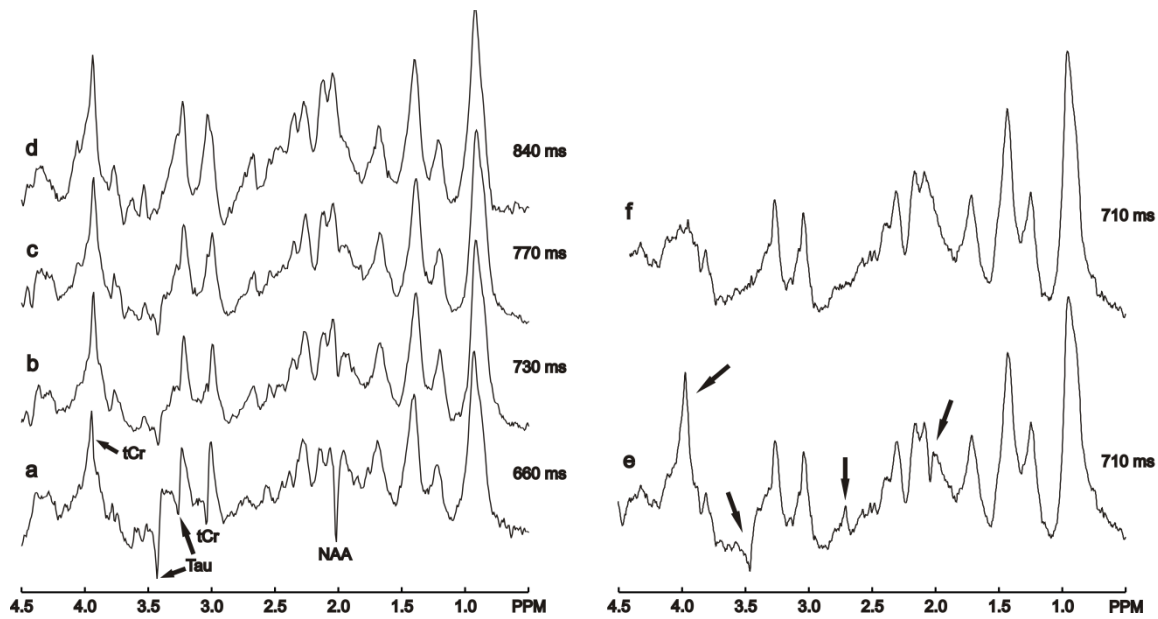


Figure 2. Series of MM spectra with a TI of (a) 660 ms, (b) 730 ms, (c) 770 ms and (d) 840 ms (TR = 2500 ms, TE = 1.7 ms, TM = 20 ms, 640 averages). The tCr line at 3.9 ppm has positive signal in all spectra due to its shorter  $T_1$ . (e) The MM spectrum with a TI of 710 ms showing residual metabolites contributions, negative peaks of NAA at 2.0 ppm and Tau at 3.44 ppm, and positive peaks of NAA at 2.68 ppm and tCr at 3.94 ppm, marked with arrows (TR = 2500 ms, TE = 1.7 ms, TM = 20 ms, 1280 averages). (f) The spectrum after eliminating the residual metabolites with the HLSVD routine. All spectra applied exponential multiplication with a linebroadening of 20 Hz.

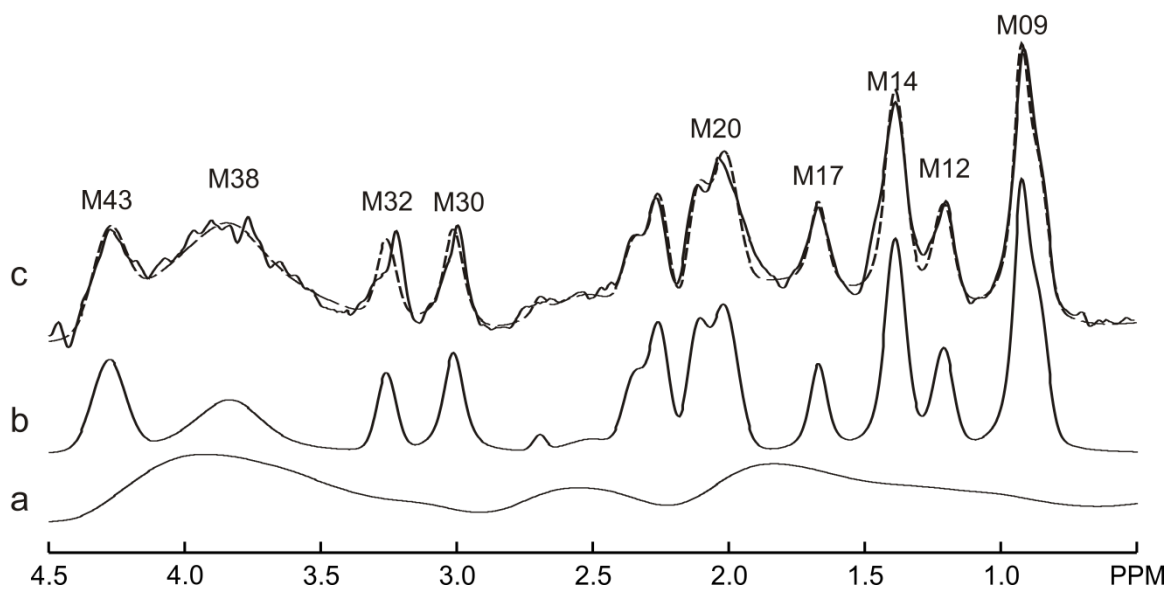


Figure 3. Final MM components found by parameterization of the measured MM spectrum. (a) The spline baseline and (b) the whole fitted MM components determined in LCModel. (c) Comparison of the fitted MM components in LCModel obtained with the measured MM spectrum and with the simulated MM spectrum (dashed line). The dashed curve is the summation of (a) the spline baseline and (b) the fitted MM components. All spectra are scaled equally.

Table 1

Parameterization of individual macromolecular components derived from the metabolite-nulled spectrum. Fitting results in the LCModel analysis were expressed with relative standard deviation (SD) and CRLB.

MM component <sup>a</sup>	Frequency (ppm)	Linewidth (ppm)	Amplitude (a.u.)	SD (%) <sup>d</sup>	CRLB (%)
M09 <sup>b</sup>				18	9
M09a	0.86	0.10	3.2		
M09b	0.92	0.04	5.0		
M12	1.22	0.10	2.5	20	12
M14	1.41	0.08	4.0	10	7
M17	1.67	0.07	2.0	12	9
M20	2.05	0.12	1.9	18	7
	2.15	0.08	1.1		
	2.29	0.08	1.2		
	2.38	0.09	0.8		
	2.54	0.20	0.3		
	2.73	0.05	0.1		
M30	3.00	0.07	2.3	21	9
M32	3.20	0.10	2.5	16	10
M38	3.85	0.26	1.7	14	13
	3.82	0.15	1.2		
	3.77	0.15	0.9		
M43 <sup>c</sup>	4.35	0.16	0.9		

<sup>a</sup>Labeling assigned according to the resonance frequency in ppm. M20 and M38 are composed of six and three single components, respectively, and are labeled with the resonance frequency of the first component.

<sup>b</sup>M09a and M09b were quantified independently. As they form single signal, the SD of their sum and their average CRLB are given.

<sup>c</sup>The fitting result was not determined since it was outside of the spectral range between 0.2 ppm to 4.3 ppm in the LCModel analysis.

<sup>d</sup>SD is expressed in percent of the mean.

Table 2

Comparison of average absolute concentration ( $\pm$ SD) and average CRLB determined with (left column) and without (right column) including Ace and Gly in the LCModel analysis. The average SNR as determined by LCModel was  $38 \pm 3$ .

Metabolites	Concentrations ( $\mu$ mol/g)	CRLB (%)	Concentrations ( $\mu$ mol/g)	CRLB (%)
Ace	$0.52 \pm 19\%$	16		
Ala	$0.65 \pm 21\%$	14	$0.65 \pm 22\%$	14
Asc	$2.39 \pm 9\%$	7	$2.49 \pm 9\%$	7
Asp	$2.62 \pm 15\%$	8	$2.66 \pm 16\%$	8
Cr	$3.36 \pm 9\%$	5	$3.43 \pm 8\%$	5
GABA	$1.58 \pm 16\%$	7	$1.83 \pm 13\%$	6
Glc	$0.94 \pm 24\%$	11	$0.86 \pm 25\%$	13
Gln	$3.57 \pm 13\%$	3	$3.71 \pm 14\%$	3
Glu	$7.61 \pm 10\%$	2	$7.86 \pm 10\%$	2
Gly	$0.78 \pm 28\%$	17		
GPC	$1.30 \pm 9\%$	4	$1.28 \pm 9\%$	4
GSH	$1.75 \pm 10\%$	5	$1.82 \pm 9\%$	5
Lac	$1.27 \pm 22\%$	8	$1.29 \pm 23\%$	8
ml	$6.18 \pm 4\%$	2	$6.29 \pm 4\%$	2
NAA	$7.42 \pm 9\%$	2	$7.55 \pm 9\%$	2
NAAG	$1.11 \pm 10\%$	6	$1.11 \pm 9\%$	7
PCh	$0.69 \pm 19\%$	14	$0.59 \pm 20\%$	16
PCr	$5.14 \pm 6\%$	3	$5.07 \pm 5\%$	3
PE	$1.98 \pm 7\%$	7	$1.96 \pm 8\%$	7
Tau	$4.17 \pm 16\%$	3	$4.15 \pm 17\%$	3
GPC + PCh	$1.99 \pm 9\%$	5	$1.87 \pm 10\%$	5

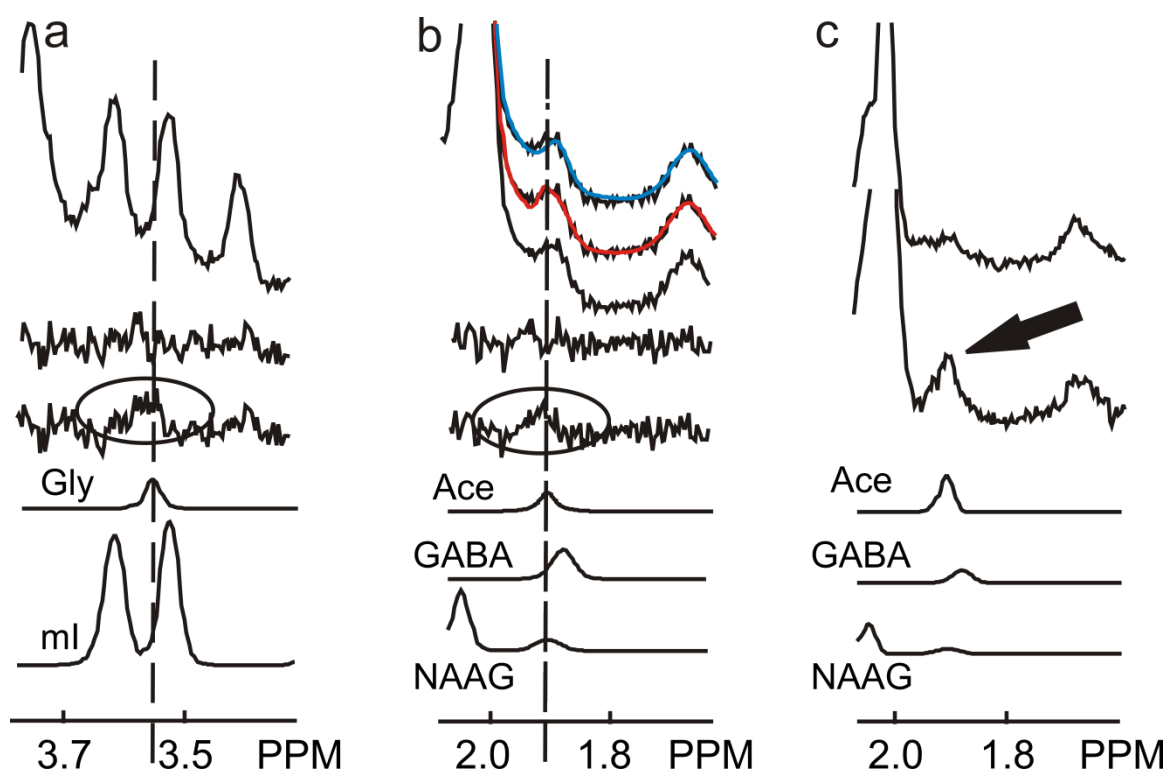


Figure 4. Verification of the detection of Ace and Gly in the LCModel analysis. The column of a and b shows the spectral regions of the Gly and the Ace peak, respectively. Shown are (from top to bottom): *in vivo* spectra, residuals (scaled two times vertically) with and without inclusion of Gly and Ace in the basis data, and fitting results for the examined and its overlapping metabolites. Spurious signals in the residuals are marked with circles. Column b also shows the fitted spectra without (blue line) and with (red line) including Ace in the LCModel analysis. Column c shows the spectra before (1st row) and during (2nd row) Ace infusion. The substantial increase of Ace is marked with an arrow. Only eddy current correction, Fourier-transformation and phase correction were applied to all spectra.

concentration of GABA shows a slight change which may indicate a small dependence between these two signals. Figure 4 shows the residuals of LCModel analysis, with and without including Ace and Gly in the basis data. While the latter display distinct peaks at 1.9 ppm and at 3.55 ppm, these spurious signals disappear when including the two metabolites in the basis data. For Ace, the change in the fitted spectra leading to the disappearance of the residual peak when including Ace in the basis set is displayed in Fig. 4b (uppermost). The spectrum acquired with Ace infusion is presented in Fig. 4c, showing substantial increase of the Ace signal (1.39  $\mu\text{mol/g}$ , CRLB 8%) with unchanged amplitudes of the overlapping two metabolites, GABA (1.03  $\mu\text{mol/g}$ , CRLB 16%) and NAAG (0.99  $\mu\text{mol/g}$ , CRLB 10%). Thus, only the Ace concentration was modified compared to the values measured without Ace infusion without affecting the methylene signals of GABA at 1.889 ppm and of NAAG at 1.9 ppm, which confirms the stable and independent detection of the Ace signal.

## 2.4 DISCUSSION

This study presents the first measurements of *in vivo*  $^1\text{H}$  NMR spectra at 16.4 T, showing for the first time the possibility to detect Ace in the rat brain *in vivo* using ultra-short TE  $^1\text{H}$  NMR spectroscopy. Acquisition and quantification of the extended neurochemical profile are achieved by taking advantage of the increased spectral dispersion and sensitivity at 16.4 T in combination with an improved LCModel basis set, containing both metabolite and MM information. The practical

problems of high field, including the increased chemical shift displacement, the decreased  $T_2$  relaxation time and the high sensitivity to susceptibility effects are compensated by using short-duration asymmetric pulses with a high bandwidth, by minimizing TE and by correcting the field inhomogeneities with FASTMAP.

The simulated MM components found by parameterization of the metabolite-nulled spectrum determined the underlying MM contributions of the data acquired with ultra-short TE. The simulated MM signals are able to accurately model the MM contributions to the spectra, as is demonstrated especially in the MM dominant region between 0.5 ppm and 2.0 ppm, where no significant residual signals remain. The alternative method of acquiring individual MM datasets for each spectrum will be difficult at high field, since assigning and eliminating residual metabolites can become a very demanding task even with the HLSVD method. The double inversion-recovery approach has been shown to reproduce the experimental baseline only poorly at 14.1 T, because of the different  $T_1$ -weighting in the MM spectrum (4). These problems may be avoided with the simulation approach used in the present study. Since regional differences in MM components have been shown to have only negligible effects on quantifying metabolite concentrations (26), the parameterization performed with the metabolite-nulled spectrum from the hippocampus can be used as basis for metabolite quantification in all brain regions. This was also ascertained by obtaining metabolite-nulled spectra from thalamus, hippocampus and striatum, which did not show significant differences (data not shown).

The stable quantification of Gly was a challenging factor even with short TE at 9.4T mainly due to the direct overlap with ml (27). To overcome this problem, several alternative approaches including the use of relatively long TE (27), TE-averaged PRESS (28) and the employment of triple refocusing pulses implemented at optimized TE (18) were reported to induce significant degradation of the ml signal while maintaining the Gly signal. In this study, Gly was resolved and quantified in all rats with average CRLB of 17%, reflecting a reliable Gly detection. The concentration was found to be 0.78  $\mu\text{mol/g}$ , which is consistent with previous data from *in vitro* rat brain tissue extracts (29).

A prior high resolution NMR study showed that the Ace methyl resonance in PCA extracts of rat brain can be contaminated during the extraction procedure or sample storage (30). This illustrates the importance of *in vivo* measurements of this metabolite, which clearly avoids this problem. In the present study, the Ace singlet at 1.9 ppm was detected and quantified both in the normal brain and during infusion of Ace. The Ace concentration determined as 0.52  $\mu\text{mol/g}$  was in agreement with previous *in vitro* studies of rodent brain extracts (31, 32). Excluding Ace from the basis data resulted in a slight increase of the GABA concentration by 16%. Although this is in the order of the standard deviation of the quantification, it might indicate a small overestimation of the GABA methylene resonance at 1.889 ppm when Ace is not quantified due to the overlap of these two resonances.

In conclusion, a substantial enhancement of *in vivo*  $^1\text{H}$  NMR spectra was achieved at 16.4 T. In addition, simulated MM components showed their suitability to substitute the measured MM spectrum. Two experimentally challenging metabolites, Ace and Gly, were consistently detected with CRLB below 20%, indicating reliable quantification. These improvements will further facilitate the use of *in vivo* MR spectroscopy at 16.4 T to investigate neurochemical variations in the rat brain.

## REFERENCES

1. Tkac I, Rao R, Georgieff MK, Gruetter R. Developmental and regional changes in the neurochemical profile of the rat brain determined by *in vivo*  $^1\text{H}$  NMR spectroscopy. *Magn Reson Med* 2003;50:24–32.
2. Pfeuffer J, Tkac I, Provencher SW, Gruetter Rolf. Toward an *in vivo* neurochemical profile: quantification of 18 metabolites in short-echo-time  $^1\text{H}$  NMR spectra of the rat brain. *J Magn Reson* 1999;141:104–120.
3. Terpstra M, Tkac I, Rao RL, Gruetter R. Quantification of vitamin C in the rat brain *in vivo* using short echo-time  $^1\text{H}$  MRS. *Magn Reson Med* 2006;55:979–983.
4. Mlynarik V, Cudalbu C, Xin L, Gruetter R.  $^1\text{H}$  NMR spectroscopy of rat brain *in vivo* at 14.1 Tesla: Improvements in quantification of the neurochemical profile. *J Magn Reson* 2008;194:163–168.
5. Chateil JF, Biran M, Thiaudiere E, Canioni P, Merle M. Metabolism of [1-( $^{13}\text{C}$ )] glucose and [2-( $^{13}\text{C}$ )] acetate in the hypoxic rat. *Neurochem Int* 2001;38:399–407.
6. Deelchand DK, Shestov AA, Koski DM, Ugurbil K, Henry PG. Acetate transport and utilization in the rat brain. *J Neurochem* 2009;109 (Suppl.1):46–54.
7. Govindaraju V, Young K, Maudsley AA. Proton NMR chemical shifts and coupling constants for brain metabolites. *NMR Biomed* 2000;13:129–153.
8. Kassem MNE, Bartha R. Quantitative proton short-echo-time LASER spectroscopy of normal human white matter and hippocampus at 4 Tesla incorporating macromolecule subtraction. *Magn Reson Med* 2003;49:918–927.
9. Seeger U, Klose U, Mader I, Grodd W, Nagele T. Parameterized evaluation of macromolecules and lipids in proton MR Spectroscopy of brain diseases. *Magn Reson Med* 2003;49:19–28.
10. Pfeuffer J, Juchem C, Merkle H, Nauerth A, Logothetis NK. High-field localized  $^1\text{H}$  NMR spectroscopy in the anesthetized and in the awake monkey. *Magn Reson Imaging* 2004;22:1361–1372.
11. Patel AB, de Graaf RA, Mason GF, Rothman DL, Shulman RG, Behar KL. The contribution of GABA to glutamate/glutamine cycling and energy metabolism in the rat cortex *in vivo*. *Proc Natl Acad Sci USA* 2005;102:5588–5593.
12. Tkac I, Starcuk Z, Choi IY, Gruetter R. *In vivo*  $^1\text{H}$  NMR spectroscopy of rat brain at 1 ms echo time. *Magn Reson Med* 1999;41:649–656.
13. Gruetter R. Automatic, localized *in vivo* adjustment of all first- and second-order shim coils. *Magn Reson Med* 1993;29:804–811.
14. Terpstra M, Gruetter R.  $^1\text{H}$  NMR Detection of vitamin C in human brain *in vivo*. *Magn Reson Med* 2004;51: 225–229.
15. de Graaf RA, Braun KPJ, Nicolay K. Single-Shot Diffusion Trace  $^1\text{H}$  NMR Spectroscopy. *Magn Reson Med* 2001;45:741–748.

16. Klose W. *In vivo* proton spectroscopy in presence of eddy currents. *Magn Reson Med* 1990;14:26–30.
17. Provencher SW. Estimation of metabolite concentrations from localized *in vivo* proton NMR spectra. *Magn Reson Med* 1993;30:672–679.
18. Choi C, Bhardwaj PP, Seres P, Kalra S, Tibbo PG, Coupland NJ. Measurement of Glycine in Human Brain by Triple Refocusing  $^1\text{H}$ -MRS *In Vivo* at 3.0T. *Magn Reson Med* 2008;59:59–64.
19. Ernst RR, Bodenhausen G, Wokaun A. Principles of nuclear magnetic resonance in one and two dimensions. Oxford: Oxford University Press; 1987. p 9–17.
20. Terpstra M, Marjanska M, Henry PG, Tkac I, Gruetter R. Detection of an antioxidant Profile in the Human Brain *In Vivo* Via Double Editing with MEGA-PRESS. *Magn Reson Med* 2006;56:1192–1199.
21. Krawczyk H, Gradowska W. Characterisation of the  $^1\text{H}$  and  $^{13}\text{C}$  NMR spectra of N-acetylaspartylglutamate and its detection in urine from patients with canavan disease. *J Pharm Biomed Anal* 2003;31:455–463.
22. Kaiser LG, Young K, Meyerhoff DJ, Mueller SG, Matson GB. A detailed analysis of localized J-difference GABA editing: theoretical and experimental study at 4 T. *NMR Biomed* 2008;21:22–32.
23. Pijnappel WWF, van den Boogaart, de Beer R, van Ormondt D. SVD-Based quantification of magnetic resonance signals. *J Magn Reson* 1992;97:122-134.
24. Naressi A, Couturier C, Devos JM, Janssen M, Mangeat C, de Beer R, Graveron-Demilly D. Java-Based graphical user interface for the MRUI quantitation package. *Magn Reson Mater Phy* 2001;12:141–152.
25. Provencher SW. LCMModel & LCMgui user's manual; 2010. p 137.
26. Xin L, Mlynarik V, Lei H, Gruetter R. Influence of regional macromolecular baseline on the quantification of neurochemical profile in rat brain. *Proc Intl Soc Mag Reson Med* 2010;18:321.
27. Gambarota G, Xin L, Perazzolo C, Kohler I, Mlynarik V, Gruetter R. *In vivo*  $^1\text{H}$  NMR measurement of glycine in rat brain at 9.4 T at short echo time. *Magn Reson Med* 2008;60:727–731.
28. Prescott AP, deB Frederick B, Wang L, Brown J, Jensen JE, Kaufman MJ, Renshaw PF. *In Vivo* Detection of brain glycine with echo-time-averaged  $^1\text{H}$  magnetic resonance spectroscopy at 4.0 T. *Magn Reson Med* 2006;55:681–686.
29. Shank RP, Aprison MH. The metabolism *in vivo* of glycine and serine in eight areas of the rat central nervous system. *J Neurochem* 1970;17:1461–1475.
30. Martin M, Labouesse J, Canioni P, Merle M. N-acetyl-L-aspartate and acetate  $^1\text{H}$  NMR signal overlapping under mild acidic pH conditions. *Magn Reson Med* 1993;29:692–694.
31. Colon A, Berl S, Clarke DD. Acetylation of synaptosomal protein: effect of  $\text{Na}^+$ . *Neurochem Res* 1987;12:431–438.

32. Mathew R, Arun P, Madhavarao CN, Moffett JR, Namboodiri MAA. Progress toward Acetate Supplementation Therapy for Canavan Disease: Glycerol Triacetate Administration Increases Acetate, but Not N-Acetylaspartate, Levels in Brain. *J Pharmacol Exp Ther* 2005;315:297–303.

## Chapter 3

### Rat-strain dependent variations in brain metabolites detected by *in vivo* $^1\text{H}$ NMR spectroscopy at 16.4 T

Sung-Tak Hong, David Z. Balla, Changho Choi, Rolf Pohmann

NMR in Biomedicine (in press)

#### ABSTRACT

Localized *in vivo*  $^1\text{H}$  NMR spectroscopy is playing an increasing role in preclinical studies, due to its ability to quantify the concentrations of up to 20 metabolites in the rat brain. To assess differences between often-used rat strains, the neurochemical profiles of Sprague-Dawley, Wistar and Fischer rats were determined at ultra-short echo time at 16.4 T. To ascertain high-qualitative quantification, a first experiment examined the dependence of measuring time on the quantification results and precision by varying the number of averages between 16 and 320. It was shown that most metabolites can be quantified precisely within short scan time, yielding Cramér-Rao lower bounds below 20% and stable concentrations for 16 metabolites with as few as 32 or 64 averages in thalamus and hippocampus, respectively.

Interstrain differences in metabolite concentrations were shown to be moderate, with taurine varying significantly between Sprague-Dawley and Wistar rats, and slightly more distinct differences to the Fischer rats, including variations in glutamate and myo-Inositol. The high spectral quality and quantification precision of all data again demonstrated the potential of *in vivo*  $^1\text{H}$  NMR spectroscopy at ultra-high field.

*Key words: in vivo  $^1\text{H}$  NMR spectroscopy; STEAM; Ultra-short TE; LCModel; CRLB; interstrain differences*

## 3.1 INTRODUCTION

Localized *in vivo*  $^1\text{H}$  NMR spectroscopy is able to provide comprehensive and noninvasive information about neurochemicals representing energy metabolism, membrane metabolism, neurotransmission and the antioxidant system (1), and thus has become an invaluable tool in clinical and preclinical studies for investigations of the healthy and diseased brain. Examinations of the rat brain have proven helpful in understanding pathologic changes in various disease models (2). It is, however, often difficult to take advantage of the results from one published study by using their results in a different setting, since differences in the animal model used, or in the brain region that is examined, may cause undetermined variations in the metabolite concentrations measured. Furthermore, it is not possible to interpret a result obtained on one rat as pathologic, based on a different study performed on a different rat strain that has shown similar results to be related to the investigated disease. In fact, *in vivo*  $^1\text{H}$  NMR spectroscopy studies in the mouse brain have shown certain differences in metabolite concentrations between strains (3, 4) while little is known about such variations in the rat brain.

Recently, technological improvements as well as increasing field strengths used in magnetic resonance measurements have boosted the quality and accuracy of quantitative *in vivo*  $^1\text{H}$  NMR spectroscopy. Higher fields benefit from increased signal-to-noise ratio (SNR) as well as a higher spectral dispersion, thus causing easier and more reliable quantification of metabolite concentrations. A comparative study between 4 T and 7 T reported an SNR increase by a factor of 2 and a 14% increase in spectral resolution, demonstrating comparable quantification results at 7 T with those at 4 T for a 16-fold decreased scan time (5). With a field strength of 9.4 T, it became possible to accurately quantify 18 metabolites in the rat brain (6), while recent experiments at 16.4 T obtained quantitative values for 20 metabolites, including alanine (Ala), ascorbate (Asc), glucose (Glc) and N-acetylaspartylglutamate (NAAG) with Cramér-Rao lower bounds (CRLB) below 20%, indicating good agreement between fitting results and to the data (7).

The aim of this study was to take advantage of this gain in spectral quality to obtain highly quantitative data for variations in the concentrations of 20 metabolites in two different brain regions from three rat strains, thus detecting possible influences of the strain on the outcome of *in vivo*  $^1\text{H}$  NMR spectroscopy measurements. In order to be sure to collect meaningful data, a preparatory study examined the influence of the scan time on quantification precision, setting lower limits for the scan duration for a desired spectral quality. This study should also be useful in assessing the advantages gained with moving to ultra-high field strength, and in differentiating influences of the increased SNR and the spectral dispersion caused by the high field on the quantification results.

## 3.2 MATERIALS AND METHODS

### 3.2.1 Animal Handling

Experiments were performed on twelve male Sprague-Dawley rats ( $204 \pm 12$  g), six male Wistar rats ( $179 \pm 7$  g) and three Fischer rats ( $175 \pm 8$  g). The weight of the animals was precisely controlled to avoid metabolite variations due to aging (8). All rats experienced a 12 hour alternating light-dark schedule (lights on at 7:00 pm) in a temperature-controlled ( $23 \pm 2$  °C) room with free access to food and water.

For MR measurements, anesthesia was induced by 4–5% and maintained by 1.5–2.5% isoflurane in mixture with  $\text{O}_2$ . Body temperature was kept at  $37 \pm 0.5$  °C by an electric heating pad and controlled through a rectal temperature sensor. The respiratory rate (40 – 60/min) was monitored and maintained by adjusting the isoflurane concentration. All experiments were approved by the institutional Animal Care and Use Committee and complied with European guidelines for the use of laboratory animals.

### 3.2.2 *In vivo* $^1\text{H}$ NMR Spectroscopy

All MR measurements were performed on a Bruker BioSpec console (Bruker BioSpin GmbH, Ettlingen, Germany) interfaced to a horizontal 16.4 T magnet with a bore size of 26 cm (Magnex Scientific, Abingdon UK) and equipped with an actively shielded gradient with an inner diameter of 12 cm, a maximum strength of 1000 mT/m and a rise time of 212  $\mu$ s. A home-made quadrature RF surface coil, composed of two geometrically decoupled single-turn coils (18 mm diameter), was employed both for transmitting and receiving. The volume-of-interest (VOI) was positioned with the aid of multi-slice axial RARE (Rapid Acquisition with Relaxation Enhancement) images obtained using the following parameters: Repetition Time TR = 1500 ms, Echo Time TE = 7.5 ms, slice thickness = 1.0 mm, matrix size = 256 x 256, Field-of-View = 28 x 28 mm. Spectra were acquired from regions-of-interest (ROIs) located in two different brain regions, the thalamus (voxel size 6.5 x 3.5 x 2.5 mm<sup>3</sup>) and the hippocampus (7.0 x 2.0 x 3.0 mm<sup>3</sup>), using a STEAM (Stimulated Echo Acquisition Mode) sequence (9) with short echo time (TR = 5000 ms, TE = 1.7 ms, Mixing Time TM = 20 ms, 2048 complex data points), consisting of three short asymmetric pulses (duration 700  $\mu$ s, bandwidth 7400 Hz) (10). Water suppression was performed with VAPOR (variable power RF pulses with optimized relaxation delays) using seven chemical shift-selective gaussian shaped RF pulses (9.1 ms, 300 Hz) interleaved with three outer volume saturation (OVS) modules (11). To increase the water suppression efficiency, an additional gaussian shaped pulse (9.133 ms, 300 Hz) was applied during the TM period. Static field inhomogeneities were corrected by automated adjustment of all first- and second-order shim terms with FASTMAP (fast automatic shimming technique by mapping along the projections) (12). Center frequency and reference pulse gain were adjusted for each voxel. In a preliminary experiment, the localization accuracy of the STEAM sequence was investigated by implementing imaging gradients (phase- and frequency-encoding) after the third slice-selective RF pulse to encode all transverse magnetization generated during the selection of a VOI (13). Then, to investigate the dependence of the quantification precision on the number of averages (NA), spectra were acquired from the thalamus and hippocampus of 6 Sprague-Dawley rats. In these measurements, 320 scans were acquired and stored individually, incorporating a phase cycling scheme to compensate for imperfections of the spoiler gradients. Finally, each of the two brain regions was examined in Sprague-Dawley, Wistar and Fischer rats by conventional spectroscopy experiments, with 256 averages in the thalamus and 320 averages in the hippocampus, summed during acquisition.

### **3.2.3 Data Processing**

In all experiments, the effect of eddy currents was compensated by using the reference signal (8 averages) acquired without water suppression (14). No additional post-processing such as zero filling, apodization, water subtraction or baseline correction was applied in any experiment. All processing was performed using home-written routines in Matlab (MathWorks, Natick, MA, USA).

To obtain the dependence of the quantification precision on the number of averages, the phase of the individually acquired FIDs was corrected using an automated technique (15) for coherent averaging. Frequency variations due to field drift were compensated based on the frequency of the NAA peak at 2.02 ppm, which could be identified accurately in all single-shot spectra without averaging. Finally, different numbers of these FIDs were summed to obtain 6 different spectra with 16, 32, 64, 128, 256 and 320 averages, respectively, resulting in a total 72 spectra from two brain regions and six rats.

As neither the linewidth nor SNR was improved significantly by the frequency correction, all further experiments for the examination of strain-specific differences were undertaken in the conventional way by simply adding all signals during acquisition.

### **3.2.4 Quantification**

Quantitative analysis was done with LCModel (16), using the basis set described in detail previously (7). Briefly, 20 numerically calculated metabolite spectra were generated by a density matrix computation program, containing the following metabolites: acetate (Ace), Ala, aspartate (Asp), Asc, creatine (Cr),  $\gamma$ -aminobutyric acid (GABA), Glc, glutamine (Gln), glutamate (Glu),

Glycine (Gly), glutathione (GSH), glycerophosphorylcholine (GPC), phosphorylcholine (PCho), myo-inositol (mi), lactate (Lac), N-acetylaspartate (NAA), NAAG, phosphocreatine (PCr), phosphorylethanolamine (PE) and taurine (Tau). Signals from macromolecular (MM) components, derived by parameterization of a metabolite-nulled spectrum, were included in the basis set used in the LCModel analysis, assuming negligible variations in MM content with brain region (17) and rat strain. In the comparison of rat strains, those values that were quantified with CRLB higher than 40% were discarded. In the study on the influence of the number of averages, quantification results with CRLBs exceeding 50% were excluded from the analysis; metabolites that do not reach this criterion in at least half of the rats were considered non-quantifiable with the corresponding number of averages. Absolute quantification was performed with reference to the signal of tCr, which was assumed to have a concentration of 8.5  $\mu\text{mol/g}$  (6). Before investigating interstrain differences in metabolite concentrations, the unquantified tCr signal as found in LCModel analysis in arbitrary units was compared to assess the stability of this reference signal.

### 3.2.5 Statistical Analysis

Statistical analysis was performed with PASW (Windows Version 18.0, SPSS Inc., Chicago, IL). Assuming equal variance, a one-way analysis of variance (ANOVA) was used for comparing metabolite concentrations in different strains with Bonferroni correction for multiple comparisons. P values below 0.05 were considered as statistically significant.

## 3.3 RESULTS

### 3.3.1 Quantification vs. number of averages

Fig. 1 shows positions and sizes of the VOIs located in the thalamus and the hippocampus. To demonstrate voxel position and localization accuracy, the STEAM localization sequence was combined with imaging gradients, yielding images of voxels showing sharp profiles with minimal sidebands. However, minor partial volume effects from corpus callosum and cortex in the spectra of the hippocampus could not be completely excluded due to the size and shape of the voxel, covering both hemispheres. Fig. 2a shows a series of *in vivo*  $^1\text{H}$  NMR spectra from the hippocampus for different numbers of averages. The SNR increase follows closely the theoretically expected relationship of the square root of the number of averages (Fig. 2b). A dependable correction of frequency drifts is indicated by the constant linewidth irrespective of NA.

Fig. 3 shows the variations of the CRLBs for the quantification of metabolites in the hippocampus for NA varying from 16 to 320. Most metabolites are shown to be already quantifiable precisely (CRLB < 20%) with 64 averages or less, while especially Ace and Gly require sufficient SNR with 256 averages or more to reach CRLBs below 20%. Similar patterns are observed in the thalamus (data not shown). A comparison of the concentrations determined in the experiments with different NA shows similar results (Fig. 4): Neither concentration values nor their standard deviations vary significantly with increasing NA for most metabolites, indicating stable quantification even at low SNR. Only signals with high CRLBs show deviations, though all metabolite concentrations become stable for 128 averages and more, even for CRLBs above 20%.

The SNR and linewidth were independent of the number of averages even when the frequency correction of the single spectra was omitted, which indicates a stable static magnetic field and physiological conditions of the animals as well as a well-established animal fixation minimizing the respiratory motion. Thus, all further experiments were performed by summing the FIDs during the data acquisition.

### 3.3.2 Metabolite quantification in thalamus and hippocampus

High quality *in vivo*  $^1\text{H}$  NMR spectra from both brain regions show sufficient sensitivity to quantify 20 metabolites. Excellent water suppression is reflected by the low amplitude of the water signal compared to the methyl signal of NAA at 2.02 ppm in all spectra regardless of rat strain and brain region. The high sensitivity is demonstrated by the clear observation of the  $\alpha$ -Glc methine signal at

5.2 ppm. Noticeable spectral variations between the two brain regions are the substantially decreased Tau methylene signals at 3.25 ppm and at 3.42 ppm and the increased GABA methylene signal at 1.9 ppm in the thalamus compared with those in the hippocampus.

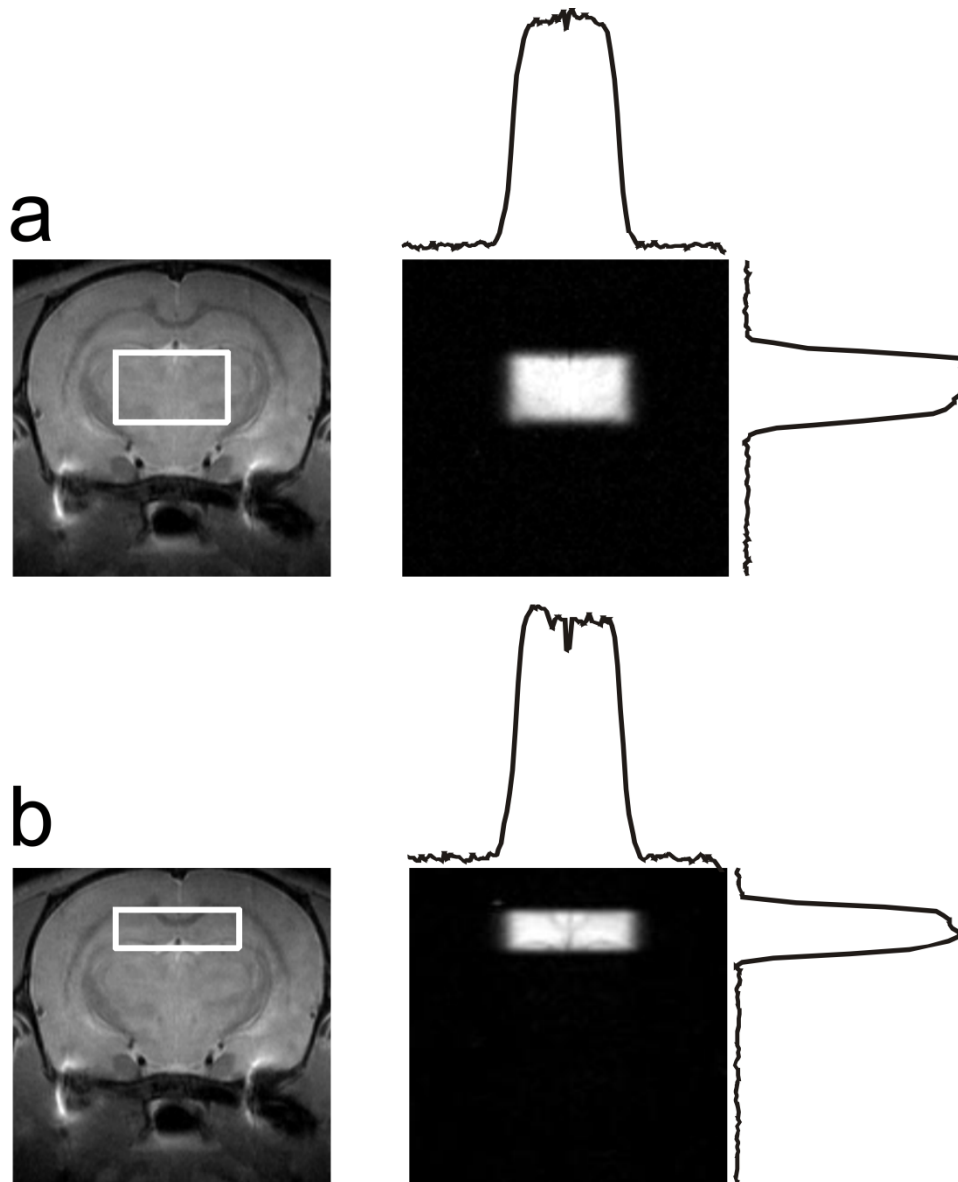


Figure 1. Voxel positions in the thalamus (a) and hippocampus (b). Due to the localization scheme, only minor partial volume effects from adjacent tissues is observed (FOV = 28 X 28 mm, matrix size = 128 X 128).

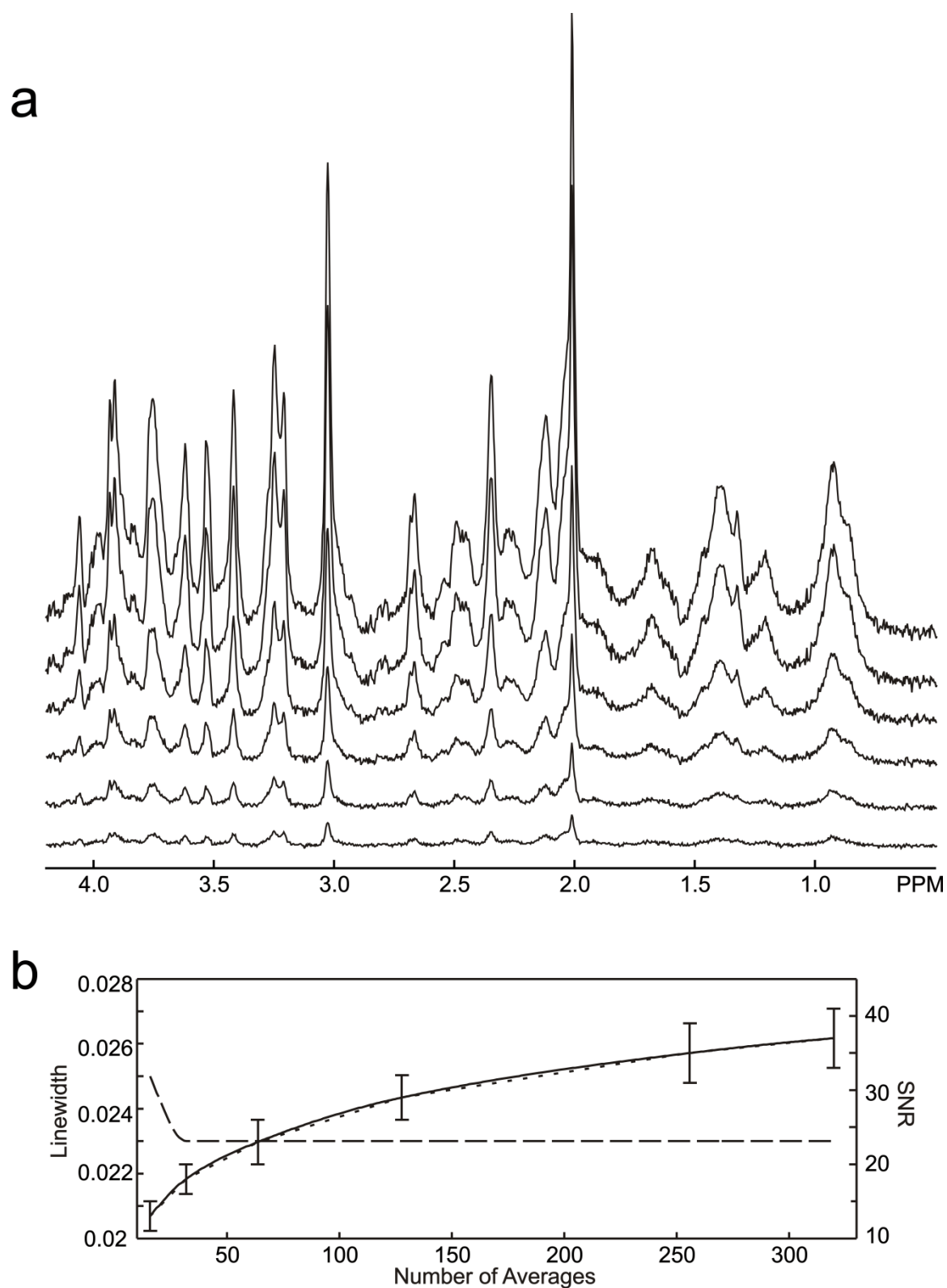


Figure 2. a: Serial *in vivo*  $^1\text{H}$  NMR spectra measured in the hippocampus of the Sprague-Dawley rat with 16, 32, 64, 128, 256 and 320 averages (from bottom to top). b: Corresponding SNR (solid line, with standard deviations) in comparison to the expected relationship (dotted line), and tCr linewidth in ppm (dashed line) as a function of number of averages as found in the LCMoel analysis.

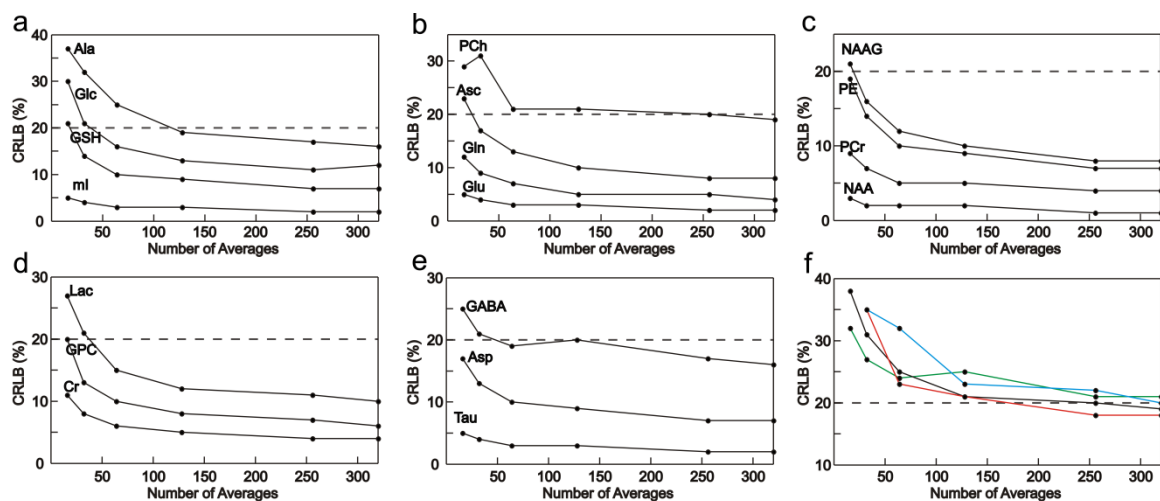


Figure 3. CRLBs found in the LCModel analysis for increasing number of averages. a-e: CRLBs of 18 metabolites found in the hippocampus. f: CRLBs of Ace and Gly in the thalamus and hippocampus (black: Ace in the thalamus, green: Ace in the hippocampus, red: Gly in the thalamus, blue: Gly in the hippocampus). Gly is considered non-quantifiable for 16 averages due to CRLBs higher than 50% in more than half of the animals.

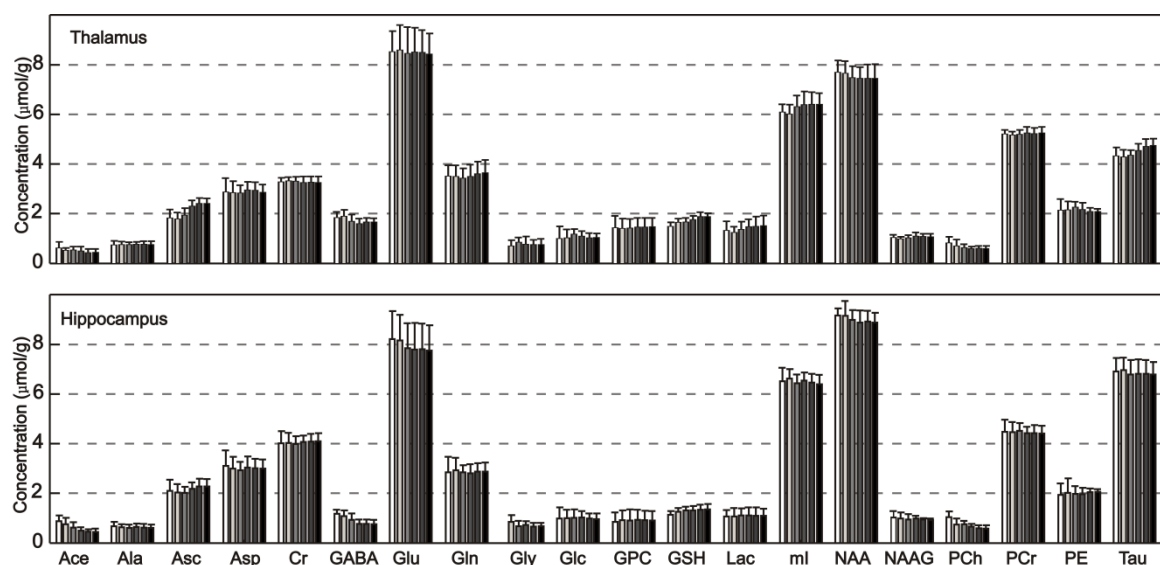


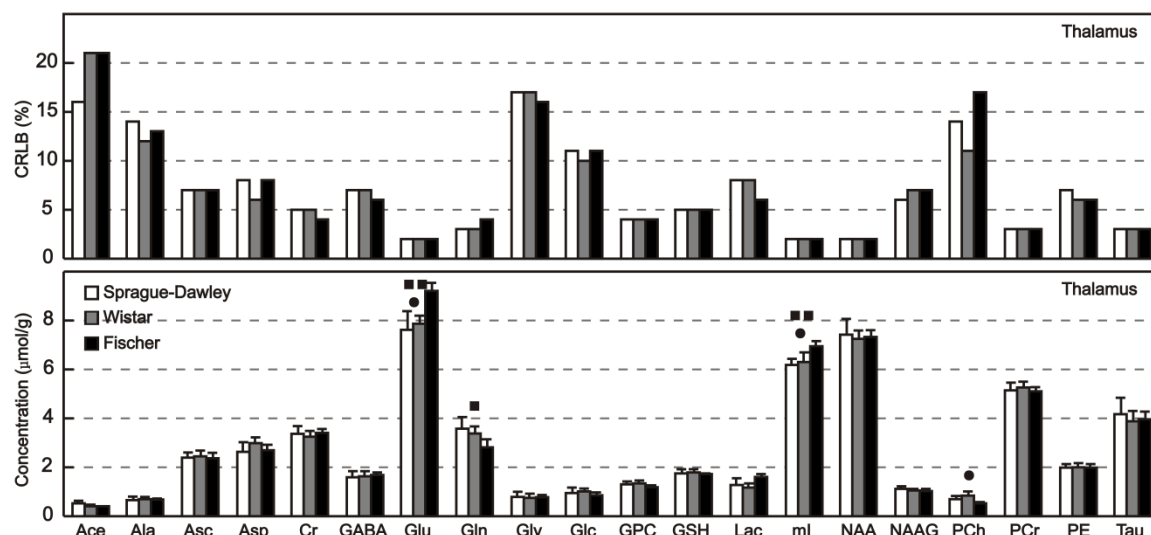
Figure 4. Metabolite concentrations in thalamus (top) and hippocampus (bottom) in Sprague-Dawley rats for number of averages between 16 (white) and 320 (black) in six rats. Error bars indicate standard deviation.

### 3.3.3 Rat strain variability

The average full width at half maximum (FWHM) found by LCModel was  $0.025 \pm 0.004$  ppm ( $17 \pm 3$  Hz) in the thalamus and  $0.024 \pm 0.003$  ppm ( $17 \pm 2$  Hz) in the hippocampus of the Sprague-Dawley rats, and similar in the Wistar and Fischer rats. Quantitative metabolite concentrations in Sprague-Dawley, Wistar and Fischer rats are presented in Fig. 5. Ace is quantified in all regions investigated irrespective of rat strains with CRLB below or only slightly exceeding 20%. Gly shows CRLBs below 20% in the thalamus, while reaching somewhat higher values in the hippocampus of Wistar and Fischer rats. Most metabolites show negligible interstrain differences except Glu, Gln, ml and PCh in the thalamus, and Ala, Glu, GPC and Tau in the hippocampus. Somewhat stronger

deviations were found for the Fischer rats, which show a prominent increase in Glu in both brain regions.

**a**



**b**

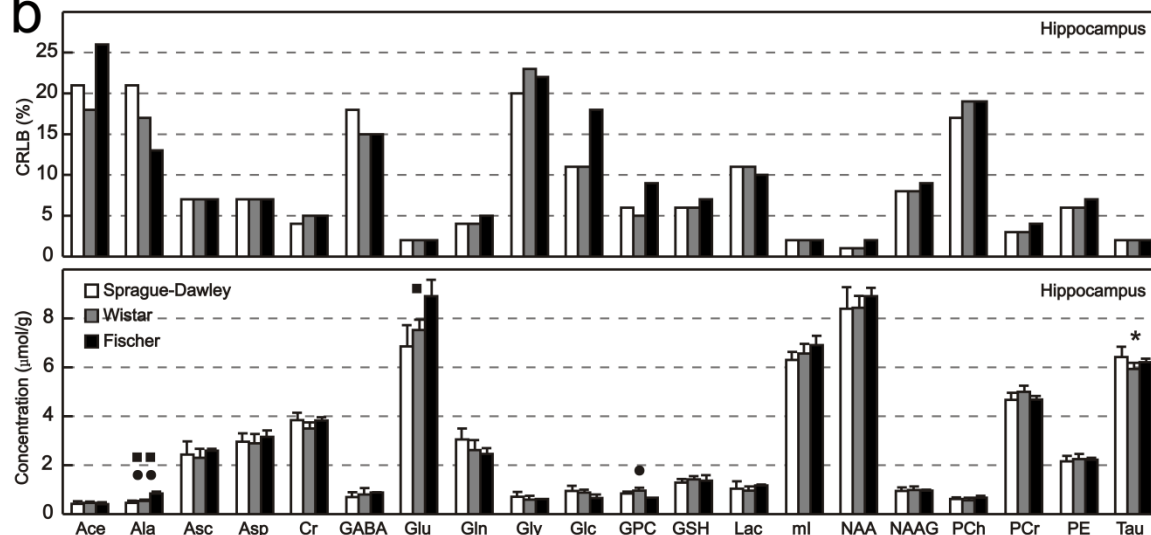


Figure 5. Comparison of metabolite concentrations in the thalamus (a) and in the hippocampus (b) of three different strains, Sprague-Dawley (white,  $n = 12$ ), Wistar (gray,  $n = 6$ ) and Fischer (black; thalamus:  $n = 3$ ; hippocampus:  $n = 2$ ) rats, with corresponding CRLBs. Interstrain differences in metabolite concentrations were determined by one-way ANOVA, \* $p < 0.05$  between Sprague-Dawley and Wistar rats, ■ $p < 0.05$  and ■■ $p < 0.005$  between Sprague-Dawley and Fischer rats and ● $p < 0.05$  and ●● $p < 0.005$  between Wistar and Fischer rats. Error bars indicate standard deviation.

### 3.4 DISCUSSION

The goal of this study, a detailed analysis of metabolite concentrations as a function of brain region and rat strain, required highly accurate and stable quantitative measurements. The good CRLB values, and, even more, the low standard deviations obtained for all metabolites, ascertain the stable quantification and thus the high spectral quality of the acquired data at 16.4 T in

conjunction with the analysis used in these experiments. Of special interest is here the dependence of quantification results and CRLBs on the number of averages, which showed that for most metabolites neither CRLBs nor standard deviations change much for a ten-fold increase in measurement time: Only for the low-concentration metabolites such as Ace, Glc, Gly, NAAG, PCh and PE does the standard deviation of the quantification values change by more than 10% when increasing the number of averages from 32 to 320. This indicates that, due to the high spectral dispersion, most metabolites can be quantified well with a low number of averages, or, alternatively, a significantly reduced voxel size. For the low-concentration metabolites, however, quantification will become imprecise for decreasing SNR.

While no previous studies are available that compare metabolite concentrations in the rat brain of different strains *in vivo* with comparable accuracy, the results shown here are in part corroborated by published data: The lack of region-dependent variations in the Ace concentration is in agreement with an *in vitro* study demonstrating an overall homogenous distribution of Ace in the rat brain (18). Another *in vitro* study using HPLC (High Performance Liquid Chromatography) (19) detected lower NAA and higher NAAG concentrations in the thalamus than in the hippocampus in Sprague-Dawley rats, in agreement with our findings. Based on these results, it can be assumed that in most cases, metabolite variations due to pathology will also be similar between different strains. However, care has to be taken in more subtle pathologies, like in psychiatric diseases (2), where the strain dependence still may be an important factor, especially in cases where one of the strain-dependent metabolites is involved, as in examinations of Huntington's disease, which is connected to variations in Glu (20).

The barely significant variations found between Wistar and Fischer rats for the low-concentration metabolites PCh and GPC have to be seen with caution, since even minor variations in the individual MM components between strains may cause changes in their quantification. Especially a modulation of the MM signals centered at 3.2 ppm and 3.8 ppm would cause differences in the calculated concentrations of these substances. Furthermore, due to the low SNR of those signals, a larger number of experiments on Fischer rats would be needed to definitely confirm those variations. In contrast, differences in the Glu, Gln and ml signals can be expected to be stable due to their high SNR.

In this study, we used the signal of tCr as a reference for the quantification of metabolite concentrations. In contrast, the water signal was used to calculate absolute concentrations in previous studies with *in vivo*  $^1\text{H}$  NMR spectroscopy (6, 21), which may cause the slight differences in concentrations determined here compared to other studies. Both approaches may be affected by concentration variations over the brain, as was shown for water in the rat (22) and the cat brain (23), as well as for Cr in the rabbit brain (24). While a region-dependent bias thus cannot be completely excluded, it can be safely assumed that the tCr concentrations in the same brain regions do not vary significantly between the strains. This was corroborated by observing a lack of significant differences in the unquantified tCr signal in the interstrain study ( $p > 0.05$ ; one-way ANOVA). Using an electric reference to access *in vivo* concentrations (ERETIC) (25) might be an effective approach to establish a very stable reference signal between different brain regions as well as different animal types, like normal controls and disease models. We also assumed similar MM concentrations in all rat strains, which was supported by negligible differences ( $p > 0.05$  in both the thalamus and the hippocampus, one-way ANOVA) found with LCModel.

In conclusion, interstrain variations in metabolite concentrations were observed for two different brain regions, thereby also demonstrating the high quantification precision at 16.4 T for up to 20 metabolites. In addition, the advantages of increasing the static field strength were explored by comparing metabolite concentrations and CRLBs as a function of NA. The observed independence on measuring times for most signals may make it possible to significantly decrease scan times for many applications, which is critical for dynamic studies such as functional MRS or indirect  $^{13}\text{C}$  NMR spectroscopy with increased temporal resolution.

**REFERENCES**

1. Shulman RG, Rothman DL. Brain energetics and neuronal activity: applications to fMRI and medicine. Wiley: Chichester, West Sussex; Hoboken, NJ; 2004.
2. Michaelis T, Boretius S, Frahm J. Localized proton MRS of animal brain *in vivo*: Models of human disorders. Prog Nucl Mag Res Spectrosc 2009;55:1-34.
3. Schwarcz A, Natt O, Watanabe T, Boretius S, Frahm J, Michaelis T. Localized proton MRS of cerebral metabolite profiles in different mouse strains. Magn Reson Med 2003;49:822-827.
4. Tkac I, Henry PG, Andersen P, Keene CD, Low WC, Gruetter R. Highly resolved *in vivo*  $^1\text{H}$  NMR spectroscopy of the mouse brain at 9.4 T. Magn Reson Med 2004;52:478-484.
5. Tkac I, Oz G, Adriany G, Ugurbil K, Gruetter R. *In vivo*  $^1\text{H}$  NMR spectroscopy of the human brain at high magnetic fields: metabolite quantification at 4T vs. 7T. Magn Reson Med 2009;62:868-879.
6. Pfeuffer J, Tkac I, Provencher SW, Gruetter R. Toward an *in vivo* neurochemical profile: quantification of 18 metabolites in short-echo-time  $^1\text{H}$  NMR spectra of the rat brain. J Magn Reson 1999;141:104-120.
7. Hong ST, Balla DZ, Shajan G, Choi C, Ugurbil K, Pohmann R. Enhanced neurochemical profile of the rat brain using *in vivo*  $^1\text{H}$  NMR spectroscopy at 16.4 T. Magn Reson Med 2011;65:28-34.
8. Agrawal HC, Davis JM, Himwich WA. Postnatal Changes in Free Amino Acid Pool of Rat Brain. J Neurochem 1966;13:607-615.
9. Frahm J, Merboldt KD, Hanicke W. Localized Proton Spectroscopy Using Stimulated Echoes. J Magn Reson 1987;72:502-508.
10. Starčuk Z Jr, Starčuk Z. Optimized asymmetric slice selective  $90^\circ$  and  $180^\circ$  RF pulses for localized MR spectroscopy. In: Proceedings of the SMR 2nd Annual Meeting, San Francisco, 1994. p 1137.
11. Tkac I, Starcuk Z, Choi IY, Gruetter R. *In vivo*  $^1\text{H}$  NMR spectroscopy of rat brain at 1 ms echo time. Magn Reson Med 1999;41:649-656.
12. Gruetter R. Automatic, localized *in vivo* adjustment of all first- and second-order shim coils. Magn Reson Med 1993;29:804-811.
13. De Graaf RA. *In vivo* NMR spectroscopy : principles and techniques. Second edition. Wiley: Chichester, 2007.
14. Klose U. *In vivo* proton spectroscopy in presence of eddy currents. Magn Reson Med 1990;14:26-30.
15. Chen L, Weng ZQ, Goh LY, Garland M. An efficient algorithm for automatic phase correction of NMR spectra based on entropy minimization. J Magn Reson 2002;158:164-168.
16. Provencher SW. Estimation of metabolite concentrations from localized *in vivo* proton NMR spectra. Magn Reson Med 1993;30:672-679.

17. Xin L, Mlynarik V, Lei H, Gruetter R. Influence of regional macromolecular baseline on the quantification of neurochemical profile in the rat brain. *Proc Intl Soc Mag Reson Med* 2010;18:321.
18. Kiselevski Y, Oganessian N, Zimatkin S, Szutowicz A, Angielski S, Niezabitowski P, Uracz W, Gryglewski RJ. Acetate metabolism in brain mechanisms of adaptation to ethanol. *Med Sci Monit* 2003; 9:BR218-222.
19. Koller KJ, Zaczek R, Coyle JT. N-Acetyl-Aspartyl-Glutamate - Regional Levels in Rat-Brain and the Effects of Brain-Lesions as Determined by a New HPLC Method. *J Neurochem* 1984;43:1136-1142.
20. Tkac I, Keene CD, Pfeuffer J, Low WC, Gruetter R. Metabolic changes in quinolinic acid-lesioned rat striatum detected non-invasively by *in vivo*  $^1\text{H}$  NMR spectroscopy. *J Neurosci Res* 2001;66:891–898.
21. Mlynarik V, Cudalbu C, Xin L, Gruetter R.  $^1\text{H}$  NMR spectroscopy of rat brain *in vivo* at 14.1Tesla: improvements in quantification of the neurochemical profile. *J Magn Reson* 2008;194:163-168.
22. Schwab M, Bauer R, Zwiener U. The distribution of normal brain water content in Wistar rats and its increase due to ischemia. *Brain Res* 1997;749:82-87.
23. Shigeno T, Brock M, Shigeno S, Fritschka E, Cervosnavarro J. The Determination of Brain Water-Content - Microgravimetry Versus Drying-Weighing Method. *J Neurosurg* 1982;57:99-107.
24. Petroff OAC, Ogino T, Alger JR. High-Resolution Proton Magnetic-Resonance Spectroscopy of Rabbit Brain - Regional Metabolite Levels and Postmortem Changes. *J Neurochem* 1988;51:163-171.
25. Heinzer-Schweizer S, De Zanche N, Pavan M, Mens G, Sturzenegger U, Henning A, Boesiger P. In-vivo assessment of tissue metabolite levels using  $^1\text{H}$  MRS and the Electric REference To access *In vivo* Concentrations (ERETIC) method. *NMR Biomed* 2010;23:406-413.

## Chapter 4

### Determination of regional variations and reproducibility in *in vivo* $^1\text{H}$ NMR spectroscopy of the rat brain at 16.4 T

Sung-Tak Hong, David Z. Balla, Rolf Pohmann

Published in Magnetic Resonance in Medicine 2011; 66: 11-17.

#### ABSTRACT

*In vivo*  $^1\text{H}$  NMR spectroscopy was used to obtain the neurochemical profile in the posterior parts of the brain, the cerebellum and the medulla oblongata in comparison to the hippocampus and the thalamus. Using small voxel sizes between 16  $\mu\text{l}$  and 32  $\mu\text{l}$  to avoid partial volume effects, most metabolites demonstrated significant regional differences except acetate,  $\gamma$ -aminobutyric acid and phosphorylcholine. Noticeable regional differences in metabolite concentrations were the significant increase of total creatine in the cerebellum and the substantial decrease of taurine in thalamus and medulla oblongata. In particular, the glycine concentration in the medulla oblongata was determined to be  $4.37 \pm 0.68 \mu\text{mol/g}$  (Cramér-Rao lower bounds 7%) and thus significantly higher than in the other regions, consistent with findings reported in both *in vivo*  $^1\text{H}$  NMR spectroscopy and *in vitro* biochemical assays. Intra-individual reproducibility and inter-individual variability were investigated by acquiring spectra from the thalamus of the same rats in two sessions. No prominent influence on measurement session was observed in metabolite concentrations with coefficients of variations being below 20% in 16 metabolites.

*Key words:* *in vivo*  $^1\text{H}$  NMR spectroscopy; STEAM; Ultra-short TE; CRLB; CV; Regional differences; Reproducibility

## 4.1 INTRODUCTION

Localized *in vivo*  $^1\text{H}$  NMR spectroscopy of the brain is able to provide invaluable comprehensive and noninvasive information for investigating the healthy and diseased brain. In preclinical research, it has helped to understand pathologic changes in various disease models. Lately, the information content of *in vivo*  $^1\text{H}$  NMR spectroscopy has been boosted by increasing magnetic field strengths available in modern MR instruments, making it possible to accurately quantify as many as 20 metabolites in the rat brain.

An important factor for determining the applicability of *in vivo*  $^1\text{H}$  NMR spectroscopy in preclinical studies is the quality of the localization, since metabolite concentrations have been shown to differ between tissues types. Thus, partial volume effects from adjacent brain structures have to be strictly avoided. A double localization strategy, combining a stimulated echo acquisition mode (STEAM) volume selection with outer volume suppression (1), has been established as a reliable technique for many *in vivo*  $^1\text{H}$  NMR spectroscopy studies, efficiently suppressing contributions from unwanted signal, while maximizing signal-to-noise ratio (SNR) and information by using short echo time (TE).

Avoiding partial volume effects, however, is still difficult in many applications due to the large voxel sizes necessary to gather sufficient signal within acceptable measurement time. Thus, the selected volumes often contain more than one tissue type, which affects both the information content of the data as well as the reproducibility, since slight changes in the positioning of the voxel between sessions cause variations in the results. Voxel size and accurate positioning, thus, are important factors in determining the quality of the experiment. Smaller voxels also help to improve  $B_0$  field homogeneity, which is beneficial for acquiring spectra from brain regions where nearby susceptibility jumps cause field variations. Thus, it has been possible to acquire neurochemical profiles from the medulla oblongata of the rat brain (2) or the hypothalamus of the mouse brain (3) with high quality.

While the reliability of the quantification of one spectrum can be assessed by means of the Cramér-Rao lower bounds (CRLB) (4), the practical applicability of spectroscopy depends even more on the reproducibility in longitudinal studies and on the variability for larger numbers of subjects. While these issues have been examined in humans (5), reporting differences in the coefficient of variations (CV) between brain regions, few studies have addressed the reproducibility issue in animal studies (6) in spite of the wide applications of *in vivo*  $^1\text{H}$  NMR spectroscopy in the rat brain.

Although we recently have shown the possibility to quantify up to 20 metabolites in the rat brain at 16.4 T (7, 8), the relatively large voxel sizes used in that study imply contributions from different tissue types in each spectrum. With the goal of obtaining data with minimal partial volume effects, the current study was designed to show that spectra from much smaller voxels can be acquired without significant loss in information. Thus, the aim of this study was threefold: First, we want to demonstrate that high-quality quantitative *in vivo*  $^1\text{H}$  NMR spectra are possible with voxels that are small enough ( $16\ \mu\text{l}$  to  $32\ \mu\text{l}$ ) to avoid partial volume effects from other brain structures, including those from the posterior and ventral region. Second, these data are used to detect differences in metabolite concentrations between four examined regions, namely hippocampus, thalamus, cerebellum and medulla oblongata. Third, the applicability of this protocol is assessed by estimating the intra-individual reproducibility and the inter-individual variability.

## 4.2 Materials and Methods

### 4.2.1 Animal preparation

Seven male Sprague-Dawley rats ( $212 \pm 14$  g) were examined. All rats were accommodated at constant temperature ( $23 \pm 2$  °C) with a 12 hour alternating light-dark schedule (lights on at 7:00 pm) and given free access to food and water.

For MR measurements, spontaneously breathing rats were anaesthetized by 4–5% and maintained by 1.5–2.5% isoflurane in mixture with O<sub>2</sub>. The rectal temperature was measured by a thermosensor and kept at 37 ± 0.3 °C using an electric heating pad. The respiratory rate was monitored and maintained at 40 – 60/min by adjusting the isoflurane concentration. All animal procedures were approved by the institutional Animal Care and Use Committee and complied with European guidelines on handling laboratory animals.

#### 4.2.2 *In vivo* <sup>1</sup>H NMR Spectroscopy

All experiments were performed on a Bruker BioSpec console (Bruker BioSpin GmbH, Ettlingen, Germany) interfaced to a 16.4 T/ 26 cm horizontal magnet (Magnex Scientific, Abingdon UK) and equipped with an actively shielded gradient (maximum strength = 1000 mT/m, rise time = 212 μs). A home-made stereotactic holder mounted on an animal cradle was used to immobilize the anaesthetized rats during the experiment. Radiofrequency transmission and reception were performed by a home-built quadrature surface coil, composed of two geometrically decoupled single-loops (18 mm diameter). RARE images (TR = 1500 ms, TE = 7.5 ms, slice thickness = 1.0 mm, field of view = 28 mm X 28 mm, matrix size = 256 x 256, number of average = 1) were acquired to position the volumes-of-interest (VOI). Static field inhomogeneities were corrected automatically by adjusting all first- and second-order shim terms with FASTMAP (fast automatic shimming technique by mapping along the projections) (9). Localization was accomplished by STEAM (10), preceded by a VAPOR (Variable Power RF Pulses with Optimized Relaxation Delays) preparation, utilizing seven chemical shift-selective Gaussian shaped RF pulses (duration 9.1 ms, bandwidth 300 Hz) for water suppression, interleaved with three outer volume saturation (OVS) modules (1). Ultra-short TE was achieved by minimizing the duration of the slice-selective asymmetric RF pulses (duration 700 μs, bandwidth 7400 Hz) (11) and spoiler gradients. An additional Gaussian shaped pulse (9.133 ms, 300 Hz) was applied during the mixing time (TM) to improve the efficiency of the water suppression. For investigating regional differences in the metabolite concentrations, *in vivo* <sup>1</sup>H NMR spectra were acquired in four different regions, hippocampus (3.0 x 1.8 x 3.0 mm<sup>3</sup>), thalamus (2.8 x 2.8 x 2.8 mm<sup>3</sup>), cerebellum (2.5 x 2.5 x 2.5 mm<sup>3</sup>) and medulla oblongata (4.0 x 2.0 x 4.0 mm<sup>3</sup>), with the following parameters: TR = 5000 ms, TE = 1.7 ms, TM = 20 ms, 2048 complex data points, 320 averages in the hippocampus and thalamus and 480 averages in the cerebellum and medulla oblongata, respectively. The relatively low bandwidth of the excitation pulses results in a chemical shift displacement of up to 28% over the spectral range of 3 ppm in all dimensions. In all measurements, center frequency and reference pulse gain were adjusted individually for each VOI. No changes in the position of the animal or the RF-coil were done between acquiring signals from the different voxels. An unsuppressed water signal, acquired in a reference measurement (8 averages), was used as an internal reference for calculating absolute metabolite concentrations. Each of the water-suppressed free induction decays (FIDs) was stored separately, though maintaining the phase cycling scheme to offset incomplete spoiling of unwanted magnetization.

An additional set of experiments was performed to estimate the reproducibility of the *in vivo* quantification of metabolite concentrations with the technique used here: In a first experiment, spectra from the thalamus of five rats were acquired in two different sessions each within approximately one week. These data were used to assess variations between sessions, both between different and within the same animals. Another experiment was done to compare the variability achieved with this protocol at 16.4 T with similar published data at lower field strength (6) by increasing the voxel size to 6.5 x 3.5 x 2.5 mm<sup>3</sup> and acquiring 720 repetitions.

#### 4.2.3 Data processing

The separately stored signals were reconstructed by first sequentially summing sixteen FIDs, resulting in 20 or 30 blocks, depending on the number of averages, to obtain sufficient SNR for correcting the frequency drifts with reference to the methyl signal of NAA at 2.02 ppm. Due to the higher SNR in the experiments with larger voxel size, this summation was not necessary for those

spectra. Instead, 144 FIDs were considered as one block resulting in 5 blocks per rat to investigate intra-individual reproducibility. The resulting blocks and FIDs were corrected for phase variations (12), static magnetic field drifts and eddy currents (13), and Fourier transformed. No further post-processing, like zero filling, apodization, water subtraction or baseline correction, was performed in any experiment. All processing was conducted using home-written scripts in Matlab (MathWorks, Natick, MA, USA).

#### 4.2.4 Quantification

For the quantification of *in vivo*  $^1\text{H}$  NMR spectra, LCModel (14) was used with the previously described basis set (7). The following 20 metabolite spectra were numerically generated, using density matrix theory (15): acetate (Ace), alanine (Ala), aspartate (Asp), ascorbate (Asc), creatine (Cr),  $\gamma$ -aminobutyric acid (GABA), glucose (Glc), glutamine (Gln), glutamate (Glu), Glycine (Gly), glutathione (GSH), glycerophosphorylcholine (GPC), phosphorylcholine (PCho), myo-inositol (ml), lactate (Lac), N-acetylaspartate (NAA), N-acetylaspartylglutamate (NAAG), phosphocreatine (PCr), phosphorylethanolamine (PE) and taurine (Tau). Macromolecular components were determined by implementing prior knowledge, derived by parameterization of a metabolite-nulled spectrum in LCModel. The individual macromolecular components were included in the fit for each spectrum based on the same parameterization, since it was shown that these components did not vary significantly between rat brain regions (16) and rat strains (8). Concentration values with CRLB > 50% were excluded from the analysis. The unsuppressed water signal, obtained with 8 averages, was used as an internal reference to calculate absolute metabolite concentrations, including the effect of regional differences in water content. Water concentrations of 45.156 M (81.28%), 42.795 M (77.03%), 43.411 M (78.14%) and 40.317 M (72.57%) were assumed in hippocampus, thalamus, cerebellum and medulla oblongata, respectively (17).

#### 4.2.5 Statistical Analysis

Statistical analysis was performed with PASW (Windows Version 18.0, SPSS Inc., Chicago, IL). To compare the regional differences in metabolite concentrations, first, the homogeneity of variances (Levene test) in each metabolite was estimated. The metabolites, for which this test confirmed homogenous distributions, were subjected to one-way analysis of variance (ANOVA) without multiple comparisons while those metabolites that failed to pass the Levene test were analyzed with a Kruskal-Wallis test. *P* values of less than 0.05 were considered statistically significant. To provide an indicator of reproducibility, the coefficient of variance (CV) was calculated for each metabolite.

### 4.3 RESULTS

Representative *in vivo*  $^1\text{H}$  NMR spectra acquired in the four examined regions are shown in Fig. 1. The quality of the shim is indicated by the linewidth (full width at half maximum, FWHM) of the tCr signal of  $14.79 \pm 1.91$  Hz (0.0212 ppm) in the hippocampus,  $16.78 \pm 1.43$  Hz (0.024 ppm) in the thalamus,  $19.64 \pm 0.85$  Hz (0.0281 ppm) in the cerebellum and  $27.45 \pm 3.4$  Hz (0.0393 ppm) in the medulla oblongata. The spectra show remarkable variations between brain regions, such as significantly decreased Tau methylene signals at 3.25 ppm and at 3.42 ppm in thalamus and medulla oblongata, and an increased tCr signal at 3.02 ppm in the cerebellum.

Quantitative concentration values found by LCModel are summarized in Table 1. Twenty metabolites were quantified in all regions investigated within the limits of CRLBs below 50%, except for Gly in the cerebellum. In all regions, at least 14 metabolites are detected with CRLBs < 20% in spite of the small voxel size, which indicates the high precision of the metabolite quantification. The weakly-represented metabolites Ace and PCh are quantified with CRLBs between 18% and 26%.

For investigating regional differences in metabolite concentrations, all metabolites are analyzed by one-way ANOVA, except for Gly, GPC and PCr which fail the Levene test. Significant regional

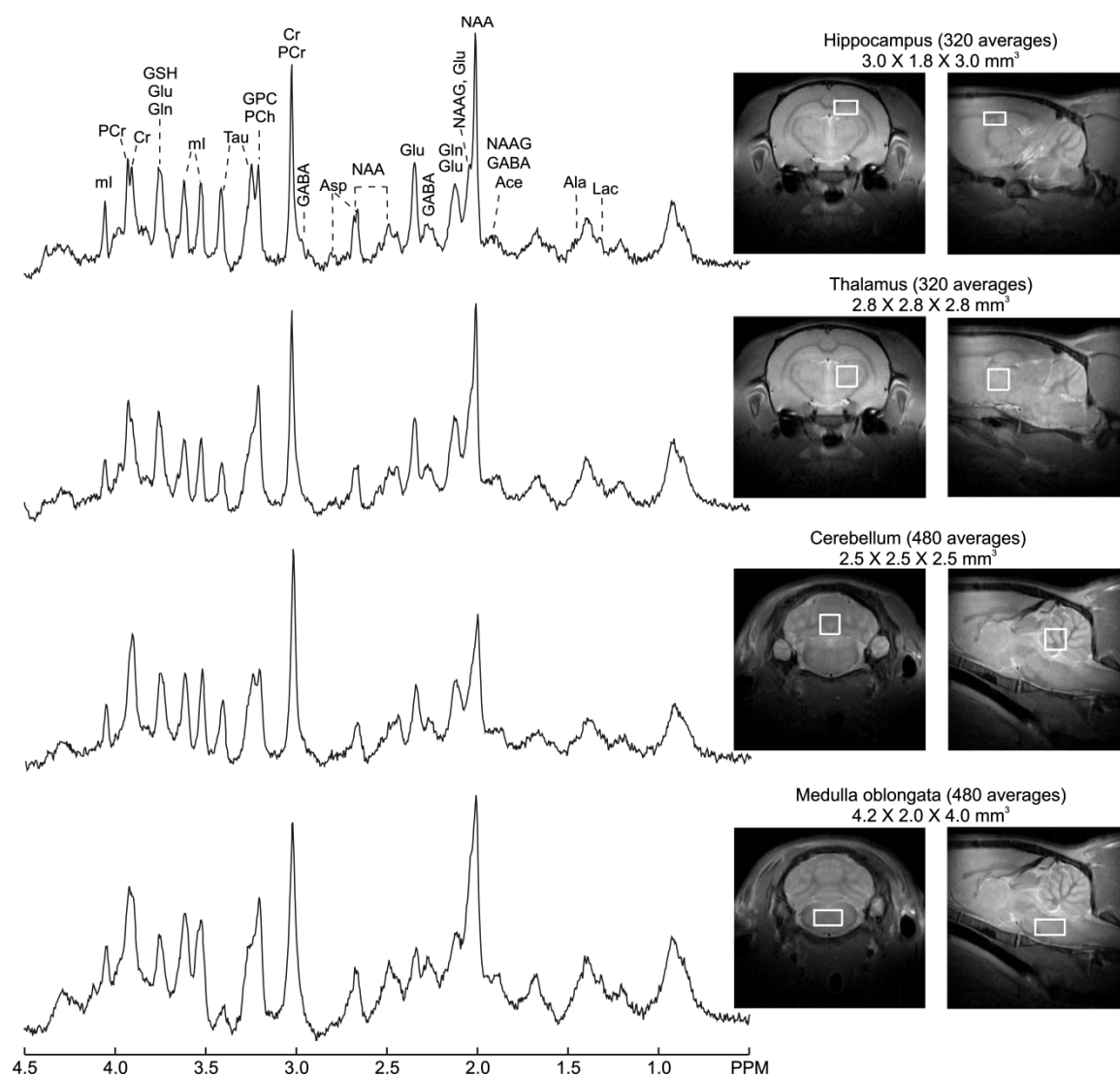


Figure 1. Representative *in vivo*  $^1\text{H}$  NMR spectra acquired in hippocampus, thalamus, cerebellum and medulla oblongata with corresponding RARE images illustrating the VOI location. In all spectra, exponential filtering (2 Hz) was applied for modest SNR enhancement.

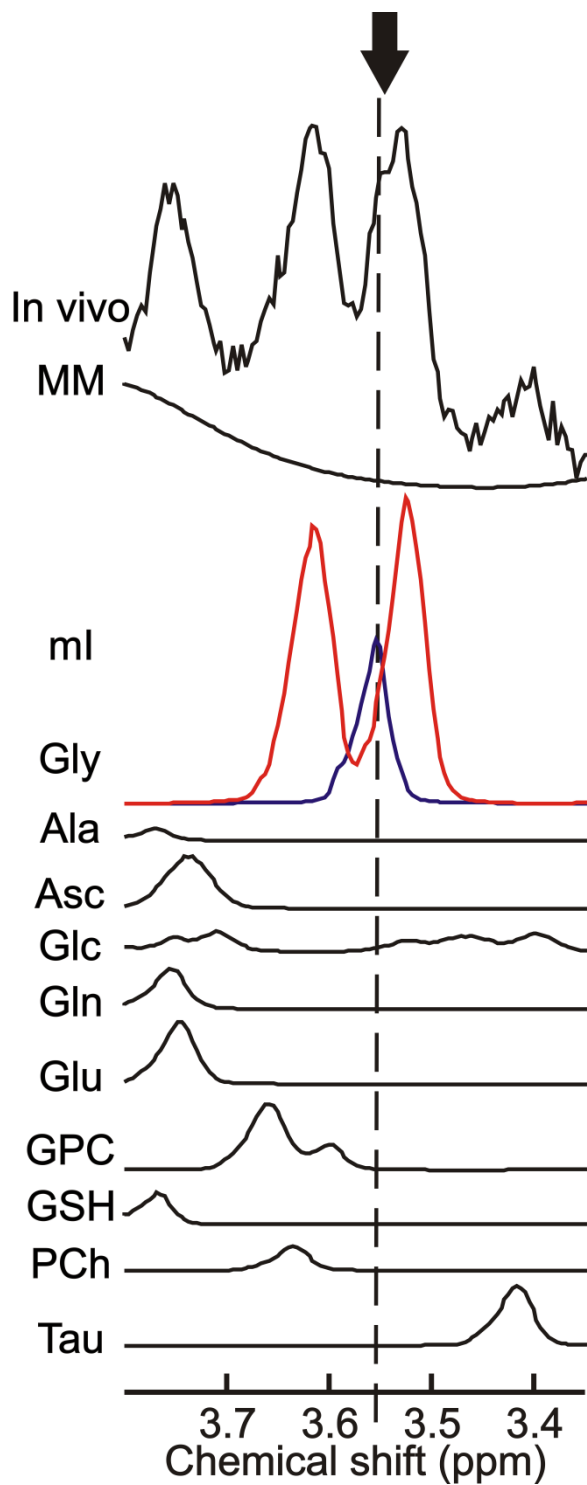


Figure 2. Expanded *in vivo*  $^1\text{H}$  NMR spectrum from the medulla oblongata, together with LCMoel fitting results of individual metabolites (ml and Gly are shown in red and blue, respectively). Only metabolites resonating between 3.35 ppm and 3.8 ppm are shown. The well-resolved resonance of Gly is marked by an arrow. Post-processing included Fourier-transformation, eddy current correction and phase correction (no apodization).

Table 1. Quantitative analysis on spectra acquired in four different brain regions.

	Ace	Ala	Asc	Asp	Cr	GABA	Glc <sup>c</sup>	Gln	Glu	Gly <sup>a</sup>	GPC	GSH	Lac <sup>c</sup>	ml	NAA	NAAG	PCh	PCr	PE	Tau	FWHM	SNR
<b>Hippocampus</b>																						
Mean (μmol/g)	0.81	0.83	3.15	4.4	5.59	1.91	1.47	3.29	11.73	1.0	0.86	2.07	1.21	8.44	12.2	1.34	1.09	6.41	2.79	9.33	14.79	23
SD (μmol/g)	0.13	0.19	0.63	0.39	0.31	0.34	0.47	0.74	0.29	0.24	0.19	0.11	0.24	0.79	0.5	0.21	0.26	0.28	0.27	1.15	1.91	3
CRLB (%)	24	25	13	10	5	13	15	9	3	28	13	9	18	3	2	12	22	5	11	3		
<b>Thalamus</b>																						
Mean (μmol/g)	0.72	0.58	2.45	2.85	4.84	2.27	1.55	4.44	8.95	0.76	1.26	2.3	1.32	7.38	9.51	1.61	1.0	6.36	2.97	5.76	16.78	22
SD (μmol/g)	0.14	0.12	0.24	0.34	0.42	0.18	0.43	0.47	0.67	0.18	0.08	0.14	0.25	0.24	0.37	0.1	0.11	0.49	0.3	1.22	1.43	2
CRLB (%)	22	30	13	13	6	9	11	5	3	33	7	7	13	3	2	8	18	5	8	4		
<b>Cerebellum</b>																						
Mean (μmol/g)	0.88	0.55	3.48	2.68	8.15	2.12	1.13	4.67	8.67		1.2	1.74	1.29	10.99	9.99	1.42	0.94	7.32	1.48	8.24	19.64	23
SD (μmol/g)	0.23	0.1	0.51	0.39	0.93	0.27	0.44	0.6	1.17		0.19	0.24	0.4	0.65	0.76	0.23	0.13	0.89	0.29	0.61	0.85	2
CRLB (%)	25	40	11	16	5	11	22	6	4		10	11	18	3	3	11	26	6	22	3		
<b>Medulla oblongata</b>																						
Mean (μmol/g)	0.71	0.82	2.77	2.86	4.84	1.79	0.76	2.22	4.21	4.37	1.29	0.8	1.64	9.02	8.77	2.09	0.93	5.28	1.71	2.05	27.45	19
SD (μmol/g)	0.14	0.25	0.51	0.71	0.96	0.45	0.19	0.58	1.0	0.68	0.27	0.22	0.55	1.15	0.73	0.19	0.25	0.49	0.44	0.43	3.4	3
CRLB (%)	26	27	12	14	8	12	30	10	7	7	9	22	13	3	3	7	25	7	17	12		
<i>P</i> value		*	**	***	***			***	***	**b	*b	***		***	***	***		**D	***	***		

Statistical significance was determined by one-way ANOVA and Kruskal-Wallis test. \* represents different statistical significance in four different brain regions, \* $P < 0.05$ , \*\* $P < 0.005$  and \*\*\*  $P < 0.0005$ . The tCr signal was employed to calculate FWHM (expressed in Hz) and SNR was found in the LCModel analysis.

a. Gly in the cerebellum was considered not to be measurable due to CRLB > 50%.

b. Represents statistical significance calculated by the Kruskal-Wallis test.

c. Glc and Lac were not analyzed due to the dependence on physiological condition.

Table 2. Comprehensive analysis of inter-individual and intra-individual CVs (%) of the spectra acquired in the thalamus

	Ace	Ala	Asc	Asp	Cr	GABA	Glc	Gln	Glu	Gly	GPC	GSH	Lac	ml	NAA	NAAG	PCh	PCr	PE	Tau	FWHM	SNR
<b>First session<sup>a</sup></b>																						
Mean ( $\mu\text{mol/g}$ )	0.74	0.59	2.45	2.75	4.8	2.3	1.59	4.46	9.07	0.75	1.24	2.31	1.43	7.34	9.46	1.59	1.04	6.42	2.94	5.94	16.47	22
SD ( $\mu\text{mol/g}$ )	0.18	0.14	0.23	0.33	0.28	0.12	0.5	0.57	0.77	0.22	0.07	0.17	0.21	0.28	0.34	0.11	0.08	0.58	0.34	1.32	1.38	2
CV (%)	24	24	9	12	6	5	32	13	8	29	5	7	15	4	4	7	8	9	11	22		
<b>Second session<sup>b</sup></b>																						
Mean ( $\mu\text{mol/g}$ )	0.65	0.8	2.8	3.21	4.61	2.32	1.51	4.25	9.62	0.83	1.18	2.1	1.41	7.41	9.44	1.54	1.07	6.35	2.99	5.85	17.44	20
SD ( $\mu\text{mol/g}$ )	0.22	0.16	0.68	0.35	0.63	0.32	0.36	0.34	0.36	0.3	0.12	0.39	0.25	0.8	0.81	0.24	0.3	0.93	0.22	1.19	1.73	3
CV (%)	34	20	24	11	14	14	24	8	4	36	10	19	18	11	9	15	28	15	7	20		
<b>Inter-individual<sup>c</sup></b>																						
CV (%)	29	22	17	12	10	10	28	11	6	33	8	13	17	8	7	11	18	12	9	21		
<b>Intra-individual</b>																						
(small voxel size)																						
CV (%)	23	22	17	12	9	6	22	4	7	32	6	12	9	5	3	6	19	3	9	9		
(large voxel size)																						
CV (%)	16	9	8	9	6	5	14	3	6	14	3	3	6	1	3	6	8	2	8	1	18.65	28
																					0.66	0

a. Values from five rats in first session

b. Values from the same five rats in second session (retest).

c. Mean of CVs for test and retest measurements

dependence on metabolite concentrations is observed in most metabolites except Ace, GABA and PCh. Particularly, the concentration of Gly in the medulla oblongata is substantially increased (more than 4 times) compared to the other regions. Similarly, Tau reveals significant regional variations, being relatively low in the medulla oblongata and highest in the hippocampus.

Metabolite concentrations and CVs for intra-individual reproducibility and inter-individual variability found in the corresponding measurements are summarized in table 2. No significant differences were found in the mean values measured in two sessions in the same animals. Inter-individual CVs are below 30% for all signals except Gly, and below 20% for 15 metabolites. Intra-individual measurements of the CVs of the same animals from both sessions show equal or much smaller variations except for a few metabolites, which pinpoints substances that vary strongly between animals. Variations below 10% are reached for 12 metabolites, for four substances the CVs differ by more than a factor of two between intra- and inter-individual measurements. Increasing the voxel size leads to a significant decrease in CVs as is expected due to the higher SNR.

## 4.4 DISCUSSION

In the current study, the goal of differentiating between signals from different brain structures required the necessity for decreasing the voxel sizes by a factor of up to 3.5 compared to previous studies (7, 8) to avoid partial volume effects. Combined with the well-established double localization scheme, combining OVS with STEAM volume selection, this made it possible to acquire spectra with negligible lipid contamination as well as minimal partial volume effects in all examined brain regions. In spite of the small voxel size, quantifying 20 metabolites was accomplished routinely in all regions except for the cerebellum, where Gly could not be quantified, with sufficient sensitivity to detect significant regional variations in the concentrations even for the less abundant substances. Reliable quantification precision was reached by carefully correcting the inhomogeneities of the static field reflected by the narrow linewidth, the sufficient water suppression indicated by an amplitude lower than that of the methyl peak of NAA at 2.02 ppm and the stable determination and fitting of the macromolecular components, using the parameterization approach presented in Ref. 7, illustrated by a flat baseline.

Acquiring reliable *in vivo*  $^1\text{H}$  spectra in the posterior parts of the brain is susceptible to several sources of impairment leading to poor spectral quality such as reduced SNR and field homogeneity, which has limited the acquisition of *in vivo*  $^1\text{H}$  spectra in this region to only few studies in humans (18) and rodents (2, 19). SNR may be decreased especially in the medulla oblongata due to its position in the posterior part of the brain. In addition, normally positioned coils for the rat brain will not reach their full sensitivity for those positions. The higher linewidth in the posterior parts of the brain is due to the heterogeneous tissue distribution in the cerebellum and the proximity of the medulla to the sinuses. A shim system with higher order coils would be necessary to correct for the resulting susceptibility variations, since the used second-order shims were not able to further improve the  $B_0$  homogeneity, in spite of still sufficient power reserve. In addition, these brain structures may be more susceptible to motion, which was avoided in the cerebellum by carefully positioning the VOI in the bottom and anterior part of the cerebellum, yielding a comparable linewidth as in the thalamus and hippocampus. In the medulla oblongata, a further reduction of the linewidth may be possible by further decreasing the VOI size, since the SNR is still sufficient and comparable to that of the other regions. A comparison to previously published data from 9.4 T (2) shows the similar precision in spite of the differences in scan time, which was reduced by almost a factor of two, reflecting the sensitivity gain due to the higher field strength. Both studies have similar relative linewidth, in spite of the increasing susceptibility variations at high field, which confirms the high performance of the shim coils and the adjustment routines used here.

The significant increase of Gly in the medulla oblongata was consistent with the findings in *in vitro* (20, 21) as well as *in vivo*  $^1\text{H}$  NMR spectroscopy (2). While this signal can be identified clearly (Fig. 2), the overlap with the mI methine resonance at 3.52 ppm makes its quantification difficult, especially in the other brain regions. Yet, even at short TE, we were able to quantify Gly with CRLBs of 28% and 33% in hippocampus and thalamus, respectively, which is sufficient to detect the significant Gly variations between those regions and the medulla oblongata. The inability to detect Gly in the cerebellum might imply low Gly concentration, as was reported in an *in vitro* biochemical study (21). The concentration of tCr was found to be highest in the cerebellum, which is in agreement with observations in the human (18) and in the mouse brain (19), indicating high kinase activity. The reduced level of GSH in the medulla oblongata is also in agreement with previous findings (22).

The reproducibility study resulted in CV values similar to the CRLBs of the quantification. In addition, the inter-individual measurements show a significantly higher variability, in agreement with similar data from the human brain (23). This indicates that, first, the variations in the concentrations found can be fully accredited to the quantification inaccuracies of the single spectrum, and, second, that quantification errors are smaller than the differences between animals. This finding confirms the ability of *in vivo*  $^1\text{H}$  NMR spectroscopy to obtain reliable data on metabolite alterations in longitudinal studies. Only a few signals show a variability much higher than the CRLBs, indicating strong variations between different scans within the same animals. Especially the Glc concentration, which is known to depend strongly on the recent food intake of the rat before the experiment, shows high variations.

Measuring the same animals in different sessions may cause further deviations due to differences in the exact positioning of the subjects or physiologic variations between the two measurement sessions, resulting in decreased reproducibility. Although VOIs were positioned carefully by the same experimenter based on multi-slice RARE images to replicate the voxel position, metabolite variations caused by discrepancies in VOI locations between two scans cannot completely be excluded. In addition, the physiologic condition may differ. Therefore, further improvements in the reproducibility may be possible by using an automatic VOI repositioning technique (24) and improving the physiologic monitoring. While only the thalamus was examined in the reproducibility study, comparable results can be expected from the hippocampus or cerebellum, since a correlation of reproducibility with spectral quality has been shown (25).

The gain caused by the high field strength is illustrated by the reproducibility measurements with larger voxel size, making it possible to directly compare the results to those found in a previous study using a similar experiment at lower field strength. The variability found here is decreased considerably, especially for the low-concentrations metabolites, yielding improvements by a factor of more than two for substances like Asp, GPC and NAAG (6).

In conclusion, we have presented the acquisition of reliable data for the neurochemical profile of hippocampus, thalamus, cerebellum and medulla oblongata, detecting significant regional differences in metabolite concentrations. The high spectral quality in the relatively small voxel sizes obtained in these experiments indicates that further reduction of voxel size would be possible with still sufficient quantification precision in acceptable time, extending the scope of *in vivo*  $^1\text{H}$  NMR spectroscopy at ultra-high field.

**REFERENCES**

1. Tkac I, Starcuk Z, Choi IY, Gruetter R. *In vivo*  $^1\text{H}$  NMR spectroscopy of rat brain at 1 ms echo time. *Magn Reson Med* 1999;41:649-656.
2. Xin L, Gambarota G, Duarte JMN, Mlynarik V, Gruetter R. Direct *in vivo* measurement of glycine and the neurochemical profile in the rat medulla oblongata. *NMR Biomed* 2010;23:1097-1102.
3. Lei H, Poitry-Yamate C, Preitner F, Thorens B, Gruetter R. Neurochemical profile of the mouse hypothalamus using *in vivo*  $^1\text{H}$  MRS at 14.1T. *NMR Biomed* 2010;23:578-583.
4. Cavassila S, Deval S, Huegen C, van Ormondt D, Graveron-Demilly D. Cramer-Rao bounds: an evaluation tool for quantitation. *NMR Biomed* 2001;14:278-283.
5. Venkatraman TN, Hamer RM, Perkins DO, Song AW, Lieberman JA, Steen RG. Single-voxel  $^1\text{H}$  PRESS at 4.0T: precision and variability of measurements in anterior cingulate and hippocampus. *NMR Biomed* 2006;19:484-491.
6. Pfeuffer J, Tkac I, Provencher SW, Gruetter R. Toward an *in vivo* neurochemical profile: quantification of 18 metabolites in short-echo-time  $^1\text{H}$  NMR spectra of the rat brain. *J Magn Reson* 1999;141:104-120.
7. Hong ST, Balla DZ, Shajan G, Choi C, Ugurbil K, Pohmann R. Enhanced neurochemical profile of the rat brain using *in vivo*  $^1\text{H}$  NMR spectroscopy at 16.4 T. *Magn Reson Med* 2011;65:28-34.
8. Hong ST, Balla DZ, Choi C, Pohmann R. Rat-strain dependent variations in brain metabolites detected by *in vivo*  $^1\text{H}$  NMR spectroscopy at 16.4 T. *NMR Biomed*, in press.
9. Gruetter R. Automatic, localized *in vivo* adjustment of all first- and second-order shim coils. *Magn Reson Med* 1993;29:804-811.
10. Frahm J, Merboldt KD, Hanicke W. Localized Proton Spectroscopy Using stimulated Echoes. *J Magn Reson* 1987;72:502-508.
11. Starčuk Z Jr, Starčuk Z. Optimized asymmetric slice selective  $90^\circ$  and  $180^\circ$  RF pulses for localized MR spectroscopy. In: Proceedings of the SMR 2nd Annual Meeting, San Francisco, 1994. p 1137.
12. Chen L, Weng ZQ, Goh LY, Garland M. An efficient algorithm for automatic phase correction of NMR spectra based on entropy minimization. *J Magn Reson* 2002;158:164-168.
13. Klose U. *In vivo* proton spectroscopy in presence of eddy currents. *Magn Reson Med* 1990;14:26-30.
14. Provencher SW. Estimation of metabolite concentrations from localized *in vivo* proton NMR spectra. *Magn Reson Med* 1993;30:672-679.
15. Ernst RR, Bodenhausen G, Wokaun A. Principles of nuclear magnetic resonance in one and two dimensions. Oxford: Oxford University Press; 1987. p 9–17.
16. Xin L, Mlynarik V, Lei H, Gruetter R. Influence of regional macromolecular baseline on the quantification of neurochemical profile in the rat brain. *Proc Intl Soc Mag Reson Med* 2010;18:321.

17. Schwab M, Bauer R, Zwiener U. The distribution of normal brain water content in Wistar rats and its increase due to ischemia. *Brain Res* 1997;749:82-87.
18. Mascalchi M, Brugnoli R, Guerrini L, Belli G, Nistri M, Politi LS, Gavazzi C, Lolli F, Argenti G, Villari N. Single-voxel long TE  $^1\text{H}$ -MR spectroscopy of the normal brainstem and cerebellum. *J Magn Reson Imaging* 2002;16:532-537.
19. Tkac I, Henry PG, Andersen P, Keene CD, Low WC, Gruetter R. Highly resolved *in vivo*  $^1\text{H}$  NMR spectroscopy of the mouse brain at 9.4 T. *Magn Reson Med* 2004;52:478-484.
20. Hudson DB, Vernadakis A, Timiras PS. Regional Changes in Amino Acid Concentration in Developing Brain and Effects of Neonatal Administration of Estradiol. *Brain Research* 1970;23:213-222.
21. Aprison MH, Shank RP, Davidoff RA. A Comparison of Concentration of Glycine a Transmitter Suspect in Different Areas of Brain and Spinal Cord in 7 Different Vertebrates. *Comp Biochem Physiol* 1969;28:1345-1355.
22. Berl S, Waelsch H. Determination of Glutamic Acid, Glutamine, Glutathione and Gamma-Aminobutyric Acid and Their Distribution in Brain Tissue. *J Neurochem* 1958;3:161-169.
23. Schirmer T, Auer DP. On the reliability of quantitative clinical magnetic resonance spectroscopy of the human brain. *NMR Biomed* 2000;13:28-36.
24. Hancu L, Blezek DJ, Dumoulin MC. Automatic repositioning of single voxels in longitudinal  $^1\text{H}$  MRS studies. *NMR Biomed* 2005;18:352-361.
25. Mullins PG, Rowland L, Bustillo J, Bedrick EJ, Lauriello J, Brooks WM. Reproducibility of  $^1\text{H}$ -MRS measurements in schizophrenic patients. *Magn Reson Med* 2003;50:704-707.

## Chapter 5

### Quantification issues of *in vivo* $^1\text{H}$ NMR spectroscopy of the rat brain investigated at 16.4 T

Sung-Tak Hong, Rolf Pohmann

Submitted to NMR in Biomedicine

#### ABSTRACT

The accuracy and precision of quantifying metabolite concentrations in *in vivo*  $^1\text{H}$  NMR spectroscopy are affected by linewidth and signal-to-noise ratio (SNR). To study the effect of both factors for *in vivo*  $^1\text{H}$  NMR spectra acquired at ultra-high field, a reference spectrum was generated by summing nine *in vivo*  $^1\text{H}$  NMR spectra obtained in the rat brain with a stimulated echo acquisition mode (STEAM) sequence at 16.4 T. Progressive deterioration of linewidth and SNR was applied to generate 6400 spectra. In an accuracy study, mean concentration values of 5 metabolites varied mainly depending on SNR, while 11 metabolites were predominantly susceptible to linewidth. The standard deviations of the concentration values obtained, on the other hand, depend almost exclusively on the SNR. Insignificant correlation was found between heavily overlapping metabolite peaks, indicating independent and reliable quantification. Two different approaches for taking macromolecular signals into account were evaluated. Using prior knowledge derived by parameterization of a metabolite-nulled spectrum demonstrated improved fitting quality with reduced Cramér-Rao lower bounds (CRLB) compared to the calculation of a regularized spline baseline. The possibility of quantifying serine was investigated, showing that even at high SNR the CRLBs (> 30%) are still insufficient to ascertain reliable quantification.

*Key words:* *in vivo*  $^1\text{H}$  NMR spectroscopy; accuracy; precision; linewidth; SNR; macromolecules; serine; LCModel; CRLB;

## 5.1 INTRODCUTION

One of the major challenges of *in vivo*  $^1\text{H}$  NMR spectroscopy is the accurate quantification of the metabolite signals which overlap heavily due to the narrow range of the chemical shift dispersion and which are superimposed by a strong baseline of broad macromolecular signals. This problem is further enhanced in the presence of inhomogeneities of the static magnetic field, since a poor shim causes a reduction of the signal-to-noise ratio (SNR) as well as an increase in linewidth. Both factors have been shown to adversely influence accuracy and precision of estimating metabolite concentrations in the human brain (1).

The fast growth of ultra-high field MR raises the expectation for quantitative evaluations with high quality. Recent measurements at 16.4 T have demonstrated the possibility of acquiring and quantifying up to 20 metabolites in the rat brain (2). However, it is still unclear whether the accuracy of the quantification at high field strength is sufficiently high to detect the small variations expected in many preclinical and neuroscientific applications.

This study examines a few questions that are connected to *in vivo*  $^1\text{H}$  NMR spectroscopy in the rat brain at ultra-high field, especially when acquired with short echo time (TE). One of the main challenges in the quantification of spectra is the often substantial overlap between different peaks together with the limited SNR. In spite of the use of highly sophisticated quantification routines, like LCModel (3), both linewidth and SNR may cause systematic variations in the metabolite concentrations found, thus affecting the accuracy of the measured data. In addition, the uncertainty of the quantification may be influenced by the same factors, leading to limited reproducibility and precision of the experiments. Here, we investigate the influence of linewidth and SNR on mean concentrations, as well as on their standard deviations, using artificially degraded *in vivo* data in conjunction with Monte-Carlo simulations. Furthermore, the interdependence of heavily overlapping lines is examined, since especially in the presence of noise or large field inhomogeneities, the quantification routines may falsely assign parts of signals from one metabolite as belonging to another.

A further problem of *in vivo*  $^1\text{H}$  NMR spectra obtained at short TE is the strong contribution of macromolecular signals, which form a broad baseline underlying the metabolite resonances. In normal brain, these signals are generated by proteins while significant contributions from mobile lipids are observed in spectra of brain tumors (4). Various techniques have been proposed to reliably isolate macromolecular signals and include them in the quantification procedure. The differences in MR properties can be used to obtain a pure macromolecular spectrum, exploiting e.g. the shorter  $T_1$  relaxation times or the lower apparent diffusion coefficient (ADC) of macromolecules compared to metabolite signals, as used in inversion recovery (5) or saturation recovery measurements (6), or by combining an inversion pulse with diffusion gradients (7). This signal can then be subtracted from the full spectrum to get rid of those signals. Alternatively, mathematical approaches can be applied to model macromolecular signals based on prior knowledge derived by the parameterization of a metabolite-nulled spectrum (2), a regularized spline baseline (3) or a semi-parametrical approach (8). In this study, the effect of two of the latter schemes to implement macromolecular signals in the quantification of metabolite concentrations are investigated by, on the one hand, modeling the baseline based on the parameterization of a metabolite-nulled spectrum, and, on the other hand, having a regularized spline baseline calculated by LCModel.

Finally, the increasing field strength may raise the question whether it is possible to find additional metabolites that may be examined. Here, serine, an amino acid which serves as signaling molecule in the brain, is an interesting candidate due to its relatively high concentration of  $\sim 1 \mu\text{mol/g}$  in the rat brain (9), which might be sufficient for quantification. This metabolite is thought to be involved in pathological processes in neuro-psychiatric and neurodegenerative diseases (10) and thus would be an interesting target in preclinical studies. In spite of the sufficient concentration, however, it has so far not been included in the analysis of *in vivo* spectroscopic data because of its severe overlap with other metabolites. In this study, we investigate spectra

acquired in the hippocampus, which is known to have a relatively high Ser concentration, to find out whether serine might be accessible for quantification in the healthy rat brain.

## 5.2 MATERIALS AND METHODS

### 5.2.1 Animal preparation

All animal experiments followed a protocol approved by the institutional Animal Care and Use Committee and complied with European guidelines on handling laboratory animals. Nine male Sprague-Dawley rats weighing 194 – 227 g were examined. All rats were accommodated at constant temperature ( $23 \pm 2$  °C) with a 12 hour light/dark cycle and free access to food and water. For MR measurements, anesthesia was induced by 4–5% and maintained by 1.5–2.5% isoflurane in mixture with O<sub>2</sub>. During experiments, the body temperature was monitored by a rectally inserted thermo-sensor, and maintained at  $37 \pm 0.3$  °C by an electric heating pad placed under the torso. The respiratory rate was monitored by a pneumatic sensor and kept at 40 – 60/min by adjusting the isoflurane concentration.

### 5.2.2 *In vivo* <sup>1</sup>H NMR Spectroscopy

MR measurements were performed on a Bruker Biospec spectrometer (Bruker BioSpin GmbH, Ettlingen, Germany) interfaced to a 16.4 T/ 26 cm horizontal magnet (Magnex Scientific, Abingdon, UK), equipped with an actively shielded gradient (inner diameter of 12 cm) with a maximum strength of 1000 mT/m and a rise time of 212 μs. The radiofrequency coil assembly consisted of two geometrically decoupled single-turn coils with an inner diameter of 18 mm for quadrature detection. Anatomical images were acquired by a RARE (rapid acquisition with relaxation enhancement) sequence (Repetition Time TR = 1500 ms, Echo Time TE = 7.5 ms, slice thickness = 1.0 mm, matrix size = 256 x 256, Field-of-View = 28 x 28 mm). A volume-of-interest (VOI) was positioned in the hippocampus (3.0 x 1.8 x 3.0 mm<sup>3</sup>) of the rat brain, and localized spectra were acquired using a STEAM (stimulated echo acquisition mode) sequence (11) with the following parameters: TR = 5000 ms, TM = 20 ms, TE = 1.7 ms, 320 averages, 2048 complex data points. A composite module composed of seven frequency-selective Gaussian RF pulses (VAPOR) and three outer volume suppression (OVS) schemes was applied to suppress the signal from water as well as that from outside the selected VOI (12). To correct static field inhomogeneities in the VOI, all first- and second-order shim terms were adjusted by FASTMAP (fast automatic shimming technique by mapping along the projections (13)). Additionally, an unsuppressed water signal (8 averages) was obtained to subsequently correct the effects of eddy currents. Each free induction decay (FID) was saved separately, though including a phase cycling scheme, to allow for retrospective corrections of frequency drifts during the *in vivo* <sup>1</sup>H NMR spectroscopy measurements.

### 5.2.3 Quantification

All spectra were quantified by LCModel (3). Density matrix simulation was used to generate a basis data set containing 20 metabolites: acetate (Ace), alanine (Ala), aspartate (Asp), ascorbate (Asc), creatine (Cr), γ-aminobutyric acid (GABA), glucose (Glc), glutamate (Glu), glutamine (Gln), Glycine (Gly), glutathione (GSH), glycerophosphorylcholine (GPC), phosphorylcholine (PCh), myo-inositol (ml), lactate (Lac), N-acetylaspartate (NAA), N-acetylaspartylglutamate (NAAG), phosphocreatine (PCr), phosphorylethanolamine (PE) and taurine (Tau). In addition, macromolecular signals were included in the basis data set based on prior knowledge derived by parameterization of a metabolite-nulled spectrum.

LCModel quantification was launched by a shell script to make it possible to process a large number of spectra with one combination of linewidth and SNR at a time. The stored result files were read by a routine written in Matlab (MathWorks, Natick, MA, USA) to calculate average metabolite concentrations and standard deviations for sets of 100 spectra. Absolute concentrations were calculated, assuming the concentration of the tCr signal to be 8.5 μmol/g (5).

#### **5.2.4 Influence of linewidth and SNR on quantification accuracy and precision**

The accuracy and precision of the metabolite quantification are important factors in assessing the usability of the technique in preclinical studies. To investigate the influence of linewidth and SNR on those parameters, changes in the concentration values obtained as well as their standard deviations with varying spectral quality were examined. After correction of phases, eddy currents and frequency drifts as described previously (14), the nine spectra from all rats were summed to construct a reference spectrum, resulting in a high SNR of 158 with a narrow linewidth (15 Hz). An exponential filter was applied to progressively increase the linewidth from 15 Hz to 29 Hz (2 Hz increment). Subsequently, Gaussian white noise was added to each of the resulting datasets to create spectra with an SNR of 30, 40, 50, 70, 90, 110, 130 and 150 for each linewidth, where the SNR was determined as the ratio of the amplitude of the methyl resonance of NAA at 2.02 ppm to the standard deviation of noise between 8.8 ppm and 12.7 ppm. To obtain a power statistical analysis, 100 signals for each combination of linewidth and SNR were obtained, resulting in a total of 6400 spectra.

All spectra were subjected to LCModel quantification and mean values and standard deviations of metabolite concentrations were extracted to evaluate changes in accuracy and precision.

#### **5.2.5 Interdependence of metabolite concentrations**

Quantification of heavily overlapping metabolite peaks may result in interdependence of the resulting values due to partial misassignment of a signal from one metabolite to another. Previous studies at lower field strength have found strong correlation between the concentration values of such peaks, indicating a high degree of misallocation of signal (5). To investigate whether this is improved at high field, the set of 100 spectra with a linewidth of 15 Hz and an SNR 40 was examined, since these values agree closely to the average of the nine *in vivo*  $^1\text{H}$  NMR spectra. For the heavily overlapping metabolite pairs GPC / PCh, Gln / Glu, Gly / ml and NAA / NAAG, the correlation coefficients were calculated to quantify interactions between the peaks.

#### **5.2.6 Estimation of macromolecular signal contributions**

The 100 spectra with a linewidth of 15 Hz and an SNR of 40 were also used to examine the effect of different approaches of including macromolecular signals in the metabolite quantification.

These spectra were processed in two ways: First, the macromolecular data obtained from a metabolite-nulled spectrum was parameterized and the different components included in the LCModel analysis. This approach was also used in the above experiments and is described in detail in Ref. (2). Alternatively, the macromolecular signals were included in the baseline by the LCModel quantification. To enable an improved determination of the macromolecular baseline in LCModel, the parameter 'dkntmn', which is used to define the knot spacing for the regularized spline baseline, was reduced to 0.05 and the simulation of macromolecules was inhibited by setting 'nsumul', which determines the number of simulated components, to zero. The reduced value of 'dkntmn' was a rough approximation of the linewidth of macromolecular component M09 (2,5).

#### **5.2.7 Detectability of Ser**

To investigate the possibility of quantifying the Ser concentration, the simulated signal of Ser is included in the basis data set as 21st metabolite. The constructed spectra with lowest linewidth (15 Hz) and different SNR ranging from 30 to 150 are processed with LCModel and CRLBs and variability of the outcome of the LCModel Ser quantification are analyzed.

### **5.3 RESULTS**

Representative spectra obtained by adding nine single spectra, shown in Fig. 1, present some examples of varied spectral quality due to adding noise (Fig. 1b), increasing the linewidth (Fig. 1c)

or both (Fig. 1d). The high spectral quality of the original data is reflected by the good water suppression and flat baseline.

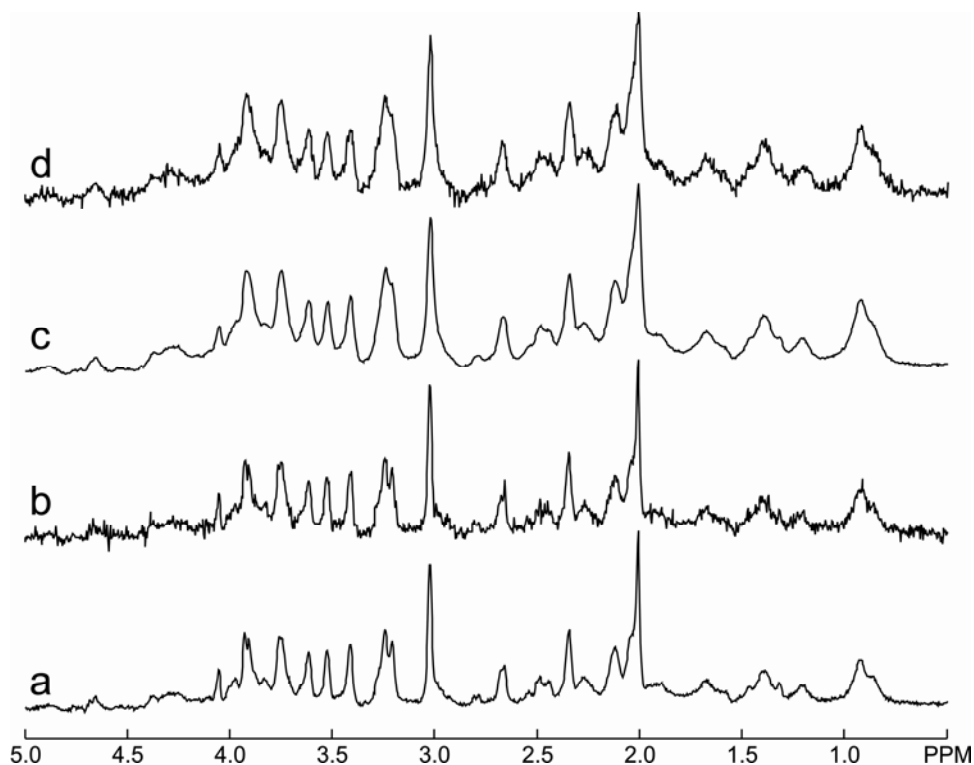


Figure 1. (a) Simulated spectra with (a) linewidth = 15 Hz and SNR = 150, (b) linewidth = 15 Hz and SNR = 30, (c) linewidth = 23 Hz and SNR = 150 and (d) linewidth = 23 Hz and SNR = 30.

### 5.3.1 Influence of linewidth and SNR on quantification accuracy and precision

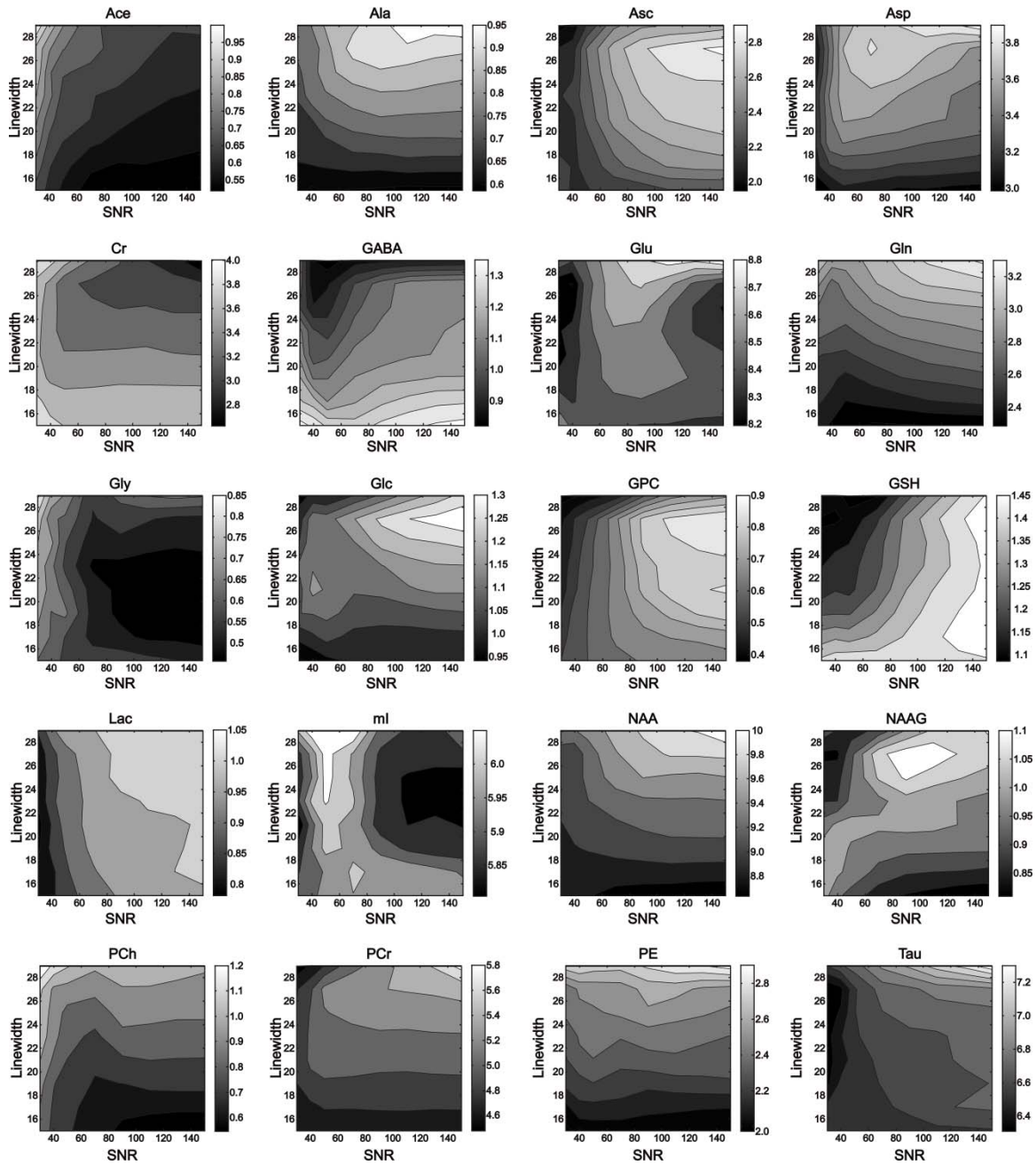
Mean metabolite concentrations found in the best spectra (linewidth = 15 Hz and SNR = 150) were considered as reference. Fig. 2a shows the variations of the metabolite concentrations found as a function of linewidth and SNR for 20 metabolites. In a coarse classification, three different patterns can be recognized depending on whether the values are mainly sensitive to SNR, to linewidth or to both factors. This is summarized in table 1. By assuming a concentration of 2  $\mu\text{mol/g}$  as criterion differentiating between substances with low and high concentrations, group 1 is mainly composed of low-concentrated metabolites (except Asc), while those in group 2, that are influenced by linewidth, have higher concentration (except Ala, GABA, Glc, NAAG and PCh). This is in agreement with the observation that in regions with low SNR at the left side of the plots, the values change mainly with increasing SNR for most substances, while high SNR regions prove to be most sensitive to linewidth changes, indicating that SNR is only decisive up to a certain level. The differences in the obtained concentrations between realistic measurement conditions (linewidth = 15 Hz and SNR = 40) and reference spectra (linewidth = 15 Hz and SNR = 150) show small variations (less than 5%) for 14 metabolites while significant alterations are detected in 6 metabolites, Ace (21%), Gly (17%), GPC (16%), Lac (15%), NAAG (18%) and PCh (39%).

The variations of the standard deviation, shown in Fig. 2b, illustrate consistently predominant susceptibility to SNR for all metabolites. The percentage differences between realistic and reference spectra are small (less than 10%) for all metabolites except Ace (14%), Ala (18%), GABA (11%), Gly (17%), Glc (13%), GPC (11%), Lac (13%) and PCh (17%).

### 5.3.2 Interdependence of metabolite concentrations

Figure 3 presents pairs of concentration values for heavily overlapping metabolites. No strong dependence between the obtained values can be observed. A negative correlation is only found

a



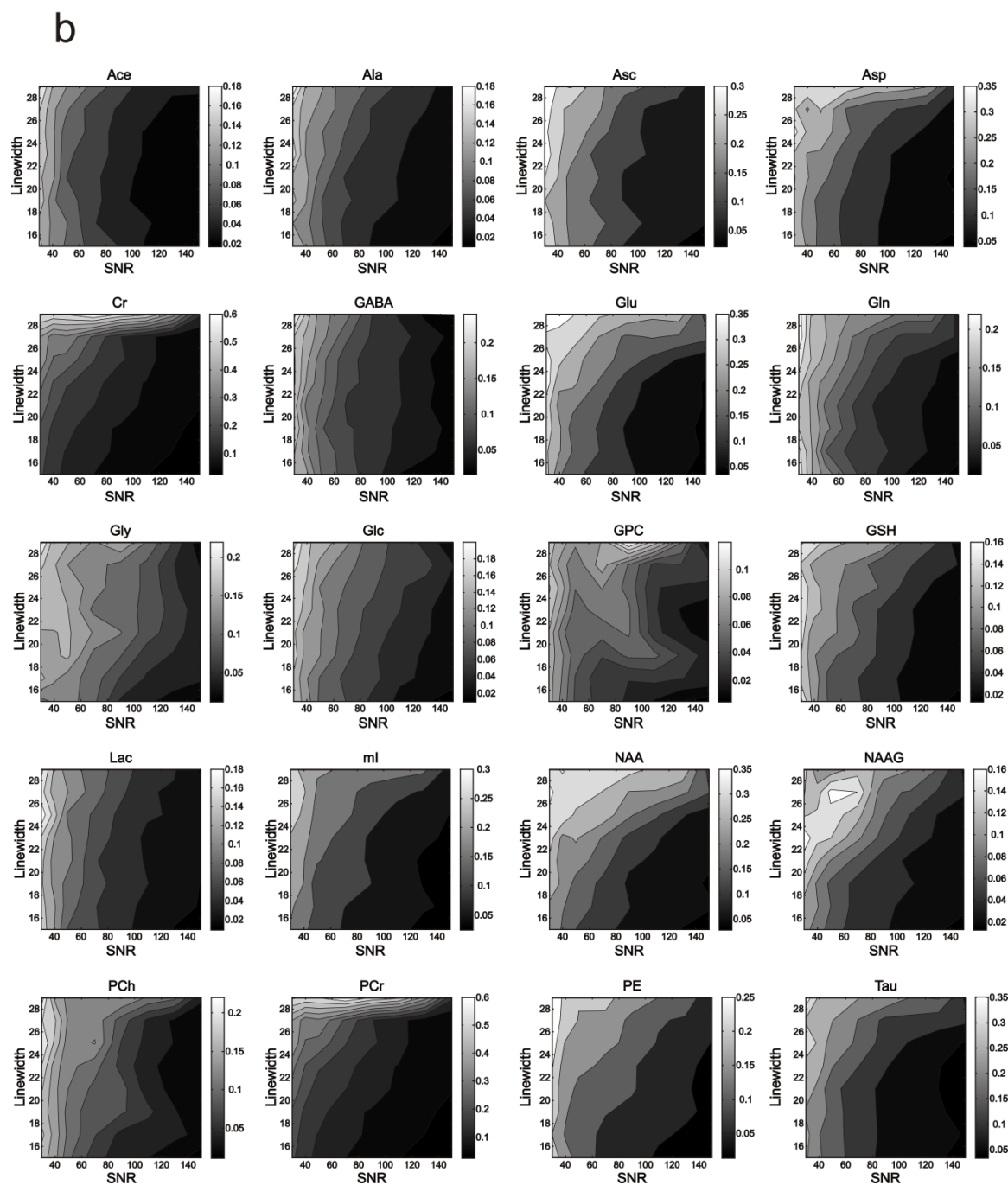


Figure 2. The responses of quantifying metabolite concentrations with changing linewidth and SNR. Mean concentration values (a) and corresponding standard deviations (b) over sets of 100 spectra as a function of SNR (x axis) and linewidth (y axis) for 20 metabolites.

Table 1. Metabolites divided into three groups with respect to response of the quantification results to varied linewidth and SNR.

Group	Concentration ( $\mu\text{mol/g}$ ) <sup>a</sup>
<b>Group 1 (sensitive to SNR)</b>	
Ace	0.42
Asc	2.43
Gly	0.7
GPC	0.83
Lac	1.03
<b>Group 2 (sensitive to linewidth)</b>	
Ala	0.45
Asp	2.95
Cr	3.84
GABA	0.69
Glc	0.94
Gln	3.04
NAA	8.39
NAAG	0.94
PCh	0.61
PCr	4.66
PE	2.15
<b>Group 3 (sensitive to both)</b>	
Glu	6.85
GSH	1.28
ml	6.29
Tau	6.42

<sup>a</sup>Values in a literature 14.

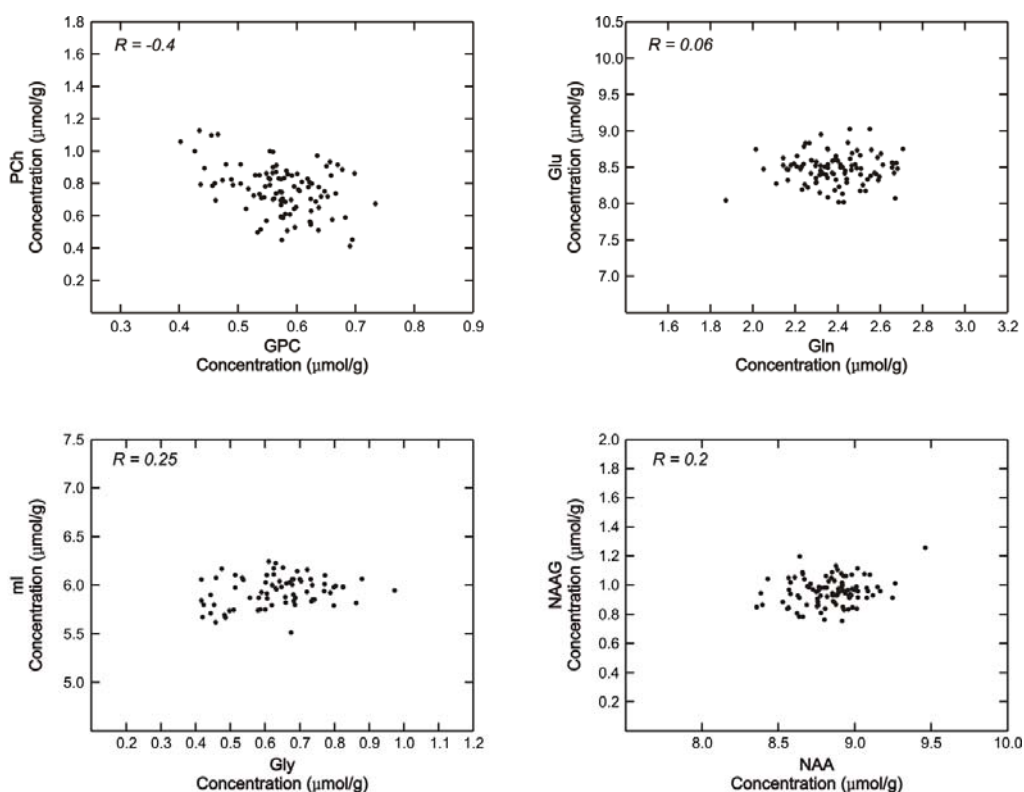


Figure 3. Correlation of pairs of heavily overlapping metabolites: GPC / PCh, Gln / Glu, Gly / ml and NAA / NAAG as obtained from 100 spectra with linewidth 15Hz and SNR 40.

for the GPC / PCh signals, though the resulting correlation coefficient is small (-0.4). The other metabolite pairs show even small positive correlation, with coefficients of 0.06 for Gln / Glu, 0.25 for Gly / ml and 0.2 for NAA / NAAG (Fig. 3), indicating independent quantification of the concentrations of those metabolites.

### 5.3.3 Estimation of macromolecular signal contributions

Figure 4 shows fitted macromolecular spectra found by two different approaches, either by including a set of signals found by parameterization of a metabolite-nulled spectrum into the basis data, or by calculating the regularized spline baseline in LCMoDel. The quantification results, shown in Fig. 5, demonstrate only minor differences (less than 10%) for the metabolite concentrations (Asc, Cr, Glc, Glu, Gly, ml, NAA, PCr, PE and Tau), while substantial differences are observed in the other half, Asp (24%), GABA (20%), Gln (16%), GPC (25%), GSH (34%), Lac (49%), NAAG (32%) and PCh (21%). Generally, the regularized spline baseline approach causes increased CRLBs in most metabolites with remarkable differences of up to 100% in Lac and NAAG. Ace and Ala are considered as not measurable with the regularized spline baseline since the CRLBs exceed 50% in 71 and 93 of 100 spectra, respectively.

### 5.3.4 Detectability of Ser

The Ser signals between 3.8 ppm and 4.0 ppm are located in a very crowded region of the *in vivo*  $^1\text{H}$  NMR spectra and overlap heavily with peaks from metabolites like Glc, the methylene signals of Cr and PCr at 3.91 ppm and at 3.93 ppm, respectively, the methine signal of Asp at 3.89 ppm, the methine and methylene signals of GPC around 3.9 ppm, the methylene signal of PE at 3.98 ppm and the methine signal of Asc at 4.01 ppm (Fig. 6).

LCMoDel quantification of the Ser signal with lowest linewidth reached average CRLBs above 30% for all SNRs. Assuming sufficiently precise values for CRLBs below 20%, this excludes the possibility of obtaining sound concentrations for Ser even at this field strength.

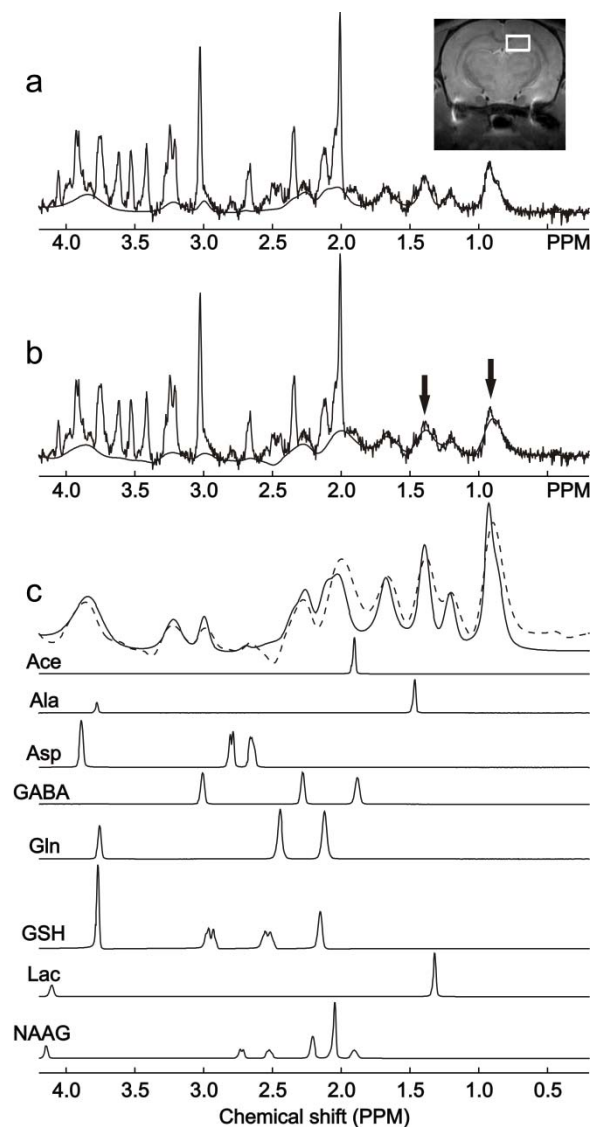


Figure 4. Representative simulated  $^1\text{H}$  NMR spectra (linewidth 15 Hz and SNR 40) based on a reference spectrum acquired by the STEAM sequence ( $\text{TR}/\text{TE}/\text{TM} = 5000/1.7/20$  ms, 2048 data points) with fitted macromolecules by using parameterization (a) and the regularized spline baseline (b). A corresponding VOI, positioned in the hippocampus ( $3.0 \times 1.8 \times 3.0$  mm $^3$ ) of the rat brain, is illustrated on an axial RARE image ( $\text{TR}/\text{TE} = 1500/7.5$  ms, slice thickness = 1.0 mm, field of view = 28 mm X 28 mm). Arrows indicate the incomplete fitting of macromolecules at a metabolite-free region with the regularized spline baseline. (c) Zoomed fitting results of macromolecules with parameterization (solid line) and with the regularized spline baseline (dashed line). Fitting results of individual metabolites showing large variations in metabolite concentrations with the two different approaches.

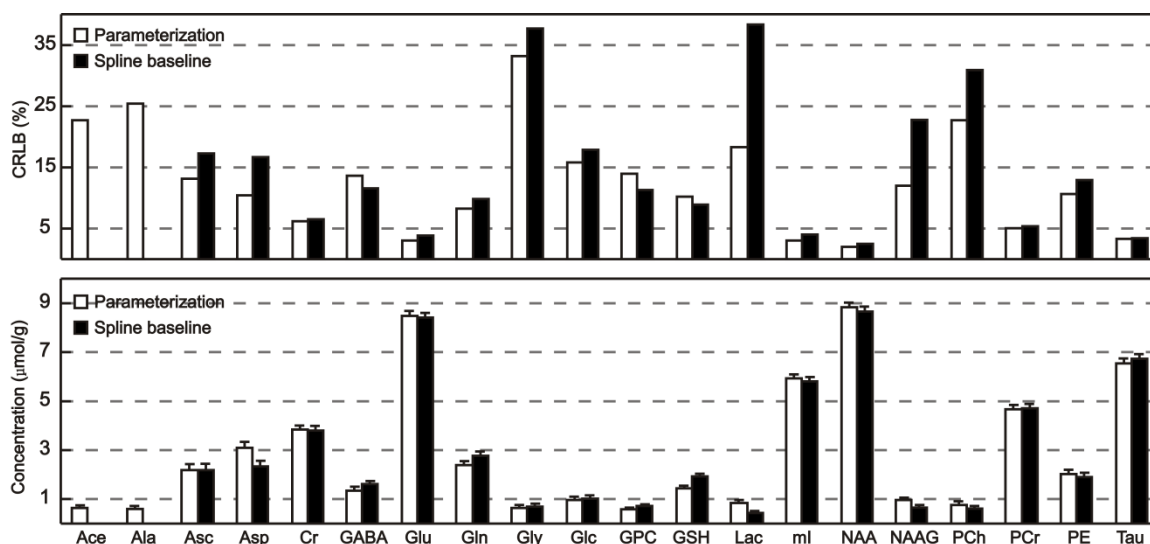


Figure 5. Comparison of metabolite concentrations found by using the two approaches for estimating macromolecular contributions: Fitting of parameterized macromolecular signals (white) and estimating the regularized spline baseline (black). Mean concentrations and the corresponding CRLBs are shown. Ace and Ala were considered not observable using the spline baseline approach due to  $CRLB > 50\%$  in more than half of the spectra. Error bars indicate standard deviation.

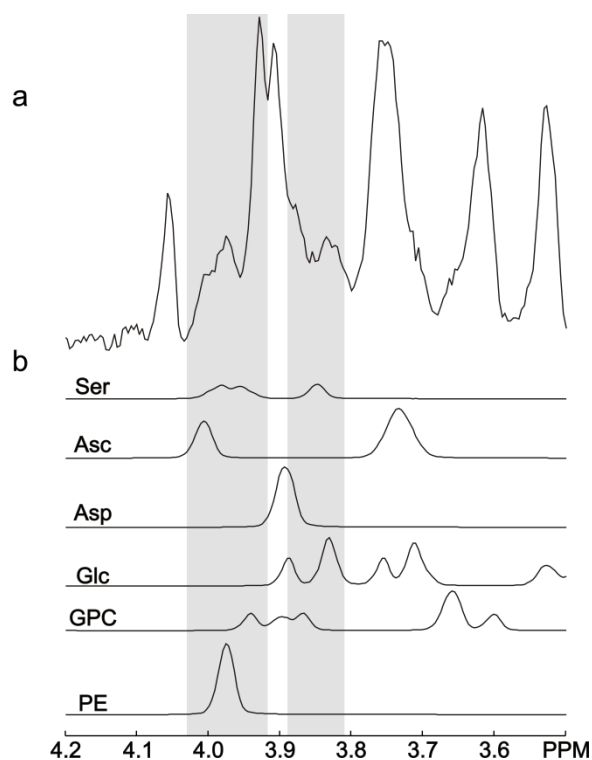


Figure 6. Expanded *in vivo*  $^1\text{H}$  NMR spectrum (linewidth 15 Hz, SNR 150) ranging from 3.5 ppm to 4.2 ppm (a) and fitted individual metabolites with overlapping peaks in that range found by LCMoDel analysis (b). A gray area highlights the spectral range of Ser. Major peaks, including the methine resonance of ml at 4.05 ppm, the methylene resonances of Cr at 3.91 ppm and of PCr at 3.93 ppm, are omitted for simplicity.

## 5.4 DISCUSSION

In this study, the characteristics of *in vivo*  $^1\text{H}$  NMR spectroscopy at ultra-high field were investigated in order to be able to assess the benefits and limitations of this technique in preclinical studies, where the need to differentiate between spectra with only slight variations may impose high demands on the accuracy and precision of the quantification.

In contrast to similar studies in the human brain (1,15), that were based on *in vitro* spectra as starting point for their investigations, *in vivo* spectra were used here to generate a reference spectrum. This has the advantage of a more realistic spectral shape, especially concerning the macromolecular components, which may play a more prominent role in our study due to the short TE of 1.7 ms at ultra-high field, which may not be sufficiently resolved by simple subtraction of a macromolecular spectrum (16). While using *in vivo* spectra limited the minimum possible linewidth to 15 Hz, significantly lower values will hardly be achieved in practice, since the hippocampus, where the spectra were acquired, is characterized by a narrow linewidth relative to that in other brain regions. In fact, the examined linewidths between 15 Hz and 29 Hz are sufficient to cover the entire range occurring in *in vivo* spectra at 16.4 T (14).

A comprehensive analysis was performed to study the effect of progressively deteriorated linewidth and SNR on accuracy and precision of quantifying metabolite concentrations. Current findings were in qualitative agreement with previous results acquired at the human brain at 4 T (1), though a direct comparison is difficult due to the large differences in field strength, measurement parameters, quantification techniques and the range of linewidth and SNR investigated (1,15,17). Although the concentration found for all metabolites varied distinctly when changing both of the parameters, in general, a higher sensitivity to linewidth changes was observed in highly concentrated metabolites and vice versa. This finding shows that increasing SNR improves the accuracy only to a certain limit, after which linewidth is the more influential parameter. In total, the differences in concentration values and standard deviations between the realistic measurements and the reference spectra is relatively small, which confirms a previous study demonstrating a decreasing effect of averaging on the CRLBs (18). Interestingly, opposite patterns were observed in the accuracy study even for metabolites with similar concentrations and chemical characteristics (chemical shifts and J-coupling constants) such as Ala / Lac and GPC / PCh (Fig. 2a). This shows that in addition to the concentrations, the spectral surroundings, such as the degree and number of overlapping metabolites, also have considerable influence. Standard deviations were strongly sensitive to SNR for all metabolites, which was consistent with results from the human brain (1), confirming the importance of SNR on the precision of estimating metabolite concentrations. Similar patterns were observed for the CRLBs (data not shown) as would be expected since their calculation depends on the noise amplitude (19).

In comparison to previous studies at lower field (5), the correlation coefficients were small, indicating independent quantification even for highly overlapping metabolites. This improvement at higher field can be contributed mainly to the increased chemical shift dispersion.

The comparison of different techniques to include macromolecular signals into the analysis showed strong differences between the two approaches: Although using the regularized spline baseline seemed to give a reasonable approximation to the underlying macromolecular peaks, the limited efficiency of this approach was indicated by missing some small structures such as those at 2.15 ppm and 2.38 ppm, close to the M20 component (2), and is especially noticeable in the metabolite-free region between 0.5 ppm and 1.8 ppm (Fig. 4b). This leads to a high number of spectra for which the CRLB exceeds 50% (71, 93, 45, 45 and 17 in Ace, Ala, Gly, Lac and PCh, respectively), which did not occur at all with the parameterization approach. The large differences in metabolite concentrations become apparent in a comparison of fitting results with both techniques (Fig. 4c). The methyl signal of Ala at 1.47 ppm is absorbed into the baseline, causing the incapability to quantify this metabolite. Similarly, the excessive width of the M14 resonance causes an underestimation in the Lac concentration. The mismatch of the M20 peak results in an underestimation of the NAAG concentration as well as overestimations of the Gln and GSH

concentrations. Using the parameterized macromolecular data as additional input in LCModel can help to avoid these problems.

Finally, the high CRLBs found for the quantification of Ser indicate the impossibility to reliably quantify this metabolite even at high SNR. This cannot be expected to change, even when further increasing the field strength. However, based on the relatively high concentration of Ser in the rat brain, spectral editing techniques (20) may make it possible to quantitatively analyze this metabolite.

**REFERENCES**

1. Bartha R. Effect of signal-to-noise ratio and spectral linewidth on metabolite quantification at 4 T. *NMR Biomed* 2007;20:512-521.
2. Hong ST, Balla DZ, Shajan G, Choi C, Ugurbil K, Pohmann R. Enhanced neurochemical profile of the rat brain using *in vivo*  $^1\text{H}$  NMR spectroscopy at 16.4 T. *Magn Reson Med* 2011;65:28-34.
3. Provencher SW. Estimation of metabolite concentrations from localized *in vivo* proton NMR spectra. *Magn Reson Med* 1993;30:672-679.
4. Kaminogo M, Ishimaru H, Morikawa M, Ochi M, Ushijima R, Tani M, Matsuo Y, Kawakubo J, Shibata S. Diagnostic potential of short echo time MR spectroscopy of gliomas with single-voxel and point-resolved spatially localised proton spectroscopy of brain. *Neuroradiology* 2001;43:353-363.
5. Pfeuffer J, Tkac I, Provencher SW, Gruetter R. Toward an *in vivo* neurochemical profile: quantification of 18 metabolites in short-echo-time  $^1\text{H}$  NMR spectra of the rat brain. *J Magn Reson* 1999;141:104-120.
6. Hofmann L, Slotboom J, Boesch C, Kreis R. Characterization of the macromolecule baseline in localized  $^1\text{H}$ -MR spectra of human brain. *Magn Reson Med* 2001;46:855-863.
7. Kunz N, Cudalbu C, Mlynarik V, Huppi PS, Sizonenko SV, Gruetter R. Diffusion-Weighted Spectroscopy: A Novel Approach to Determine Macromolecule Resonances in Short-Echo Time  $^1\text{H}$ -MRS. *Magn Reson Med* 2010;64:939-946.
8. Ratiney H, Coenradie Y, Cavassila S, van Ormondt D, Graveron-Demilly D. Time-domain quantitation of  $^1\text{H}$  short echo-time signals: background accommodation. *Magn Reson Mater Phy* 2004;16:284-296.
9. Agrawal HC, Davis JM, Himwich WA. Postnatal Changes in Free Amino Acid Pool of Rat Brain. *J Neurochem* 1966;13:607-615.
10. Wolosker H, Dumin E, Balan L, Foltyn VN. D-amino acids in the brain: D-serine in neurotransmission and neurodegeneration. *Febs J* 2008;275:3514-3526.
11. Frahm J, Merboldt KD, Hanicke W. Localized Proton Spectroscopy Using Stimulated Echoes. *J Magn Reson* 1987;72:502-508.

12. Tkac I, Starcuk Z, Choi IY, Gruetter R. *In vivo*  $^1\text{H}$  NMR spectroscopy of rat brain at 1 ms echo time. *Magn Reson Med* 1999;41:649-656.
13. Gruetter R. Automatic, localized *in vivo* adjustment of all first- and second-order shim coils. *Magn Reson Med* 1993;29:804-811.
14. Hong ST, Balla DZ, Pohmann R. Determination of regional variations and reproducibility in *in vivo*  $^1\text{H}$  NMR spectroscopy of the rat brain at 16.4 T. *Magn Reson Med* 2011;66:11-17.
15. Kanowski M, Kaufmann J, Braun J, Bernarding J, Tempelmann C. Quantitation of simulated short echo time  $^1\text{H}$  human brain spectra by LCModel and AMARES. *Magn Reson Med* 2004;51:904-912.
16. Kassem MNE, Bartha R. Quantitative proton short-echo-time LASER spectroscopy of normal human white matter and hippocampus at 4 Tesla incorporating macromolecule subtraction. *Magn Reson Med* 2003;49:918-927.
17. Macri MA, Garreffa G, Giove F, Guardati M, Ambrosini A, Colonnese C, Maraviglia B. *In vivo* quantitative  $^1\text{H}$  MRS of cerebellum and evaluation of quantitation reproducibility by simulation of different levels of noise and spectral resolution. *Magn Reson Imaging* 2004;22:1385-1393.
18. Hong ST, Balla DZ, Choi C, Pohmann R. Rat-strain dependent variations in brain metabolites detected by *in vivo*  $^1\text{H}$  NMR spectroscopy at 16.4 T. *NMR Biomed* (in press).
19. Cavassila S, Deval S, Huegen C, van Ormondt D, Graveron-Demilly D. Cramer-Rao bounds: an evaluation tool for quantitation. *NMR Biomed* 2001;14:278-283.
20. Choi CH, Dimitrov I, Douglas D, Zhao CG, Hawesa H, Ghose S, Tamminga CA. *In Vivo* Detection of Serine in the Human Brain by Proton Magnetic Resonance Spectroscopy ( $^1\text{H}$ -MRS) at 7 Tesla. *Magn Reson Med* 2009;62:1042-1046.

## Chapter 6

### CONCLUSIONS and OUTLOOK

The main purpose of this thesis was to investigate the potentials of ultra-high field for the application of *in vivo*  $^1\text{H}$  NMR spectroscopy in preclinical studies of the brain. This involved an implementation and optimization of the sequence as well as a rigorous examination of the characteristics and limitations of single-voxel MRS at 16.4 T.

First, a STEAM sequence with a short echo time was implemented to obtain spectra with maximum information content by avoiding losses due to  $T_2$  and J-coupling. The TE of 1.7 ms was achieved by reducing the duration of slice-selective RF pulses and spoiler gradients. The chemical shift displacement artifact, one of the critical problems with increasing static field strength, was minimized by using asymmetric pulses with large bandwidth and short duration. However, increased contributions of macromolecular components to spectra at ultra-short TE required an efficient approach for taking these components into account in the quantification of the metabolite concentrations. The technique chosen here, using a metabolite-nulled spectrum to parameterize single macromolecular peaks, that are then included in the LCModel analysis, has the advantages of being able to detect changes in macromolecular content in pathologies without the need to acquire additional macromolecular spectra for every subject, and to accurately model the shape of the spectral baseline. Thus, combining the high sensitivity at ultra-high field strength with an improved quantification technique made it possible to reliably detect and quantify an additional metabolite, Ace, for the first time *in vivo*  $^1\text{H}$  NMR spectroscopy.

Further studies carefully examined the properties of *in vivo*  $^1\text{H}$  spectroscopy at ultra-high field. Thus, the variations of the CRLB as a function of the number of averages were comprehensively analyzed to determine changes of the quality of the quantification with measurement time, demonstrating the possibility to measure most metabolites precisely with less than 150 averages. This should facilitate dynamic studies including direct/indirect  $^{13}\text{C}$  spectroscopy and functional MRS. Minor interstrain differences in metabolite concentrations were observed in contrast to substantial regional differences in metabolite concentrations. The highly reproducible quantification results were ascertained by intra- and inter-individual reproducibility measurements. The combination of a Monte-Carlo simulation with the LCModel algorithm provided an insight into the accuracy and precision of estimating metabolite concentrations as a function of linewidth and SNR. Pronounced sensitivity to linewidth was observed in highly concentrated metabolites while metabolites with smaller concentrations were dominated by the variations of SNR. The importance of the accurate determination of macromolecules was ascertained by demonstrating improved reliability of the quantification with the parameterization approach compared to the regularized spline baseline.

Further studies could now use the developed technique in preclinical studies on animal models, where the improved metabolic profile that can be acquired at ultra-high field should help to gain insight into different pathologies. In addition, it should be studied whether the quantification of Ace is sensitive enough to detect pathological variation. While the voxel size used in these studies were still comparable to those of previous studies performed at lower field strength, it may be possible to reliably acquire spectra from much smaller volumes. Furthermore, technical improvements might be useful to extend the anatomical structures that can be examined: While the STEAM sequence used here provided excellent neurochemical profile in all brain regions selected (hippocampus, thalamus, cerebellum and medulla oblongata), acquiring spectra from more difficult regions in the deeper parts of the brain such as the hypothalamus and the substantia nigra might be possible using, e.g., the adiabatic selective refocusing (LASER) sequence. Based on a previous study, reporting an echo time of 15 ms with LASER at 11.7 T, reaching echo time below 10 ms in a semi-LASER experiment might be possible at 16.4 T to minimize J-modulation and  $T_2$  relaxation.

The homogeneity of the static field becomes a more challenging issue at higher field strength since susceptibility differences grow with increasing field strength. Here, alternative shimming approaches such as FASTAMP with adiabatic pulses or the use of a volume coil for transmission, especially for the deep parts of the brain, would be advantageous. This increased susceptibility also causes problems when the VOIs are located close to the skull. For example, spectra acquired from the cortex showed distorted peaks around 1.4 ppm, which is due to contamination from lipids around the skull. These disturbances are caused by imperfect localization and incomplete outer-volume suppression, both of which have to be improved to extend the range of possible applications of single-voxel spectroscopy.

Further efforts could be made to improve the quantification quality: Although all numerically calculated spectra with ideal pulses showed very close agreement with measured spectra, including realistic slice-selective RF pulses into the density matrix simulations will improve the agreement between simulated spectra and *in vitro* spectra, especially for longer TE. In addition, further refinement of chemical shift and J-coupling values is an important ingredient to improve the accuracy of simulated spectra.

Finally, chemical shift imaging (CSI) could be applied to provide highly enhanced metabolite maps by taking advantages of ultra-high field strength, resulting in observations of anatomical distribution of metabolites in a single experiment.

The studies presented in this thesis have demonstrated the high accuracy and reproducibility of *in vivo*  $^1\text{H}$  NMR spectroscopy at ultra-high field. Together with future applications and enhancements, this technique will finally be able to play an important role in medical and neuroscientific research.

## APPENDIX

### Product Operator Formalism

The product operator by raising and lower operators are defined by

$$I^+ = I_x + il_y, \quad I^- = I_x - il_y, \quad I_0 = I_z$$

#### A.1 Chemical shift evolution

$$\begin{aligned} I^+ &\xrightarrow{\omega t I_z} I^+ e^{-i\omega t} \\ I^- &\xrightarrow{\omega t I_z} I^- e^{+i\omega t} \\ I_0 &\xrightarrow{\omega t I_z} I_0 \end{aligned}$$

where  $\omega t$  is an angle rotating about the z axis

#### A.2 Scalar evolution

$$\begin{aligned} I^+ &\xrightarrow{\pi J t 2 I_z S_z} I^+ \cos \pi J t - 2i I^+ S_0 \sin \pi J t \\ I^- &\xrightarrow{\pi J t 2 I_z S_z} I^- \cos \pi J t + 2i I^- S_0 \sin \pi J t \\ I_0 &\xrightarrow{\pi J t 2 I_z S_z} I_0 \\ 2I^+ S_0 &\xrightarrow{\pi J t 2 I_z S_z} 2I^+ S_0 \cos \pi J t - i I^+ \sin \pi J t \\ 2I^- S_0 &\xrightarrow{\pi J t 2 I_z S_z} 2I^- S_0 \cos \pi J t + i I^- \sin \pi J t \end{aligned}$$

#### A.3 RF pulse

$$\begin{aligned} I^+ &\longrightarrow \frac{I^+}{2} (\cos \theta + 1) - \frac{I^-}{2} (\cos \theta - 1) e^{-2i\phi} + i I_0 \sin \theta e^{-i\phi} \\ I^- &\longrightarrow \frac{I^-}{2} (\cos \theta + 1) - \frac{I^+}{2} (\cos \theta - 1) e^{-2i\phi} - i I_0 \sin \theta e^{+i\phi} \\ I_0 &\longrightarrow \frac{i I^+}{2} \sin \theta e^{-i\phi} - \frac{i I^-}{2} \sin \theta e^{+i\phi} + I_0 \cos \theta \end{aligned}$$

where  $\phi$  the phase of a RF pulse and  $\theta$  is a flip angle.